ISSN 2435-7499 (Online)
ISSN 2189-6909 (Print)
November 2021

LASTI
Annual Report

Laboratory of Advanced Science and Technology for Industry
University of Hyogo

Vol.22 (2020)

PREFACE

This annual report reviews the research activities of the Laboratory of Advanced Science and Technology for Industry (LASTI) in the academic year of 2019 which is from April 2019 to March 2020) including research activities using NewSUBARU light source at the SPring-8 site and other research activities of the micro and nanoscale are carried out energetically at the Center for Advanced Science and Technology (CAST) II.

NewSUBARU facility has a 1.0-1.5 GeV electron storage ring, which provides light beams from IR to Soft X-ray regions, and the largest synchrotron light facility operated by the university in Japan.

The researches which are carried out are the light sources for next generation through a machine R and D, and the industrial applications such as EUVL lithography, LIGA process, material analysis.

The annual report describes mainly that topics of the NewSUBARU research activities of this year including 1) the research and development of gamma ray application at BL1 beamline, 2) the next generation lithography by Extreme UltraViolet (EUV) lithography at BL3, BL9B, BL9C, and BL10 beamlines, 3) Lithographie, Galvanoformung, and Abformung (LIGA) process technology at BL2 and BL11 beamlines, 4) the chemical analysis using soft X-ray absorption fine structure at (BL5, BL9A, and BL7 beamlines and soft X-ray emission spectroscopy at BL5 and BL9A beamlines at soft X-ray energy region.

Most of our research activities are being conducted in collaboration research works with industries, research institutes, and other universities, inside and outside Japan.

We will continue to respond to the community's demand by offering new science and novel technology.

The SPring-8 linear accelerator which had been used as an injection of the electron beam both to SPring-8 and NewSUBARU electron beam storage rings in cooperation of the SPring-8 accelerator team. For the innovation work on NewSUBARU, the new injector program started from 2016. The subsidiary building employed as a klystron gallery for the new injector was constructed on March, 2019. And the previous linear accelerator was shut down on July 29, 2020. From April to December, the new linear accelerator for NewSUBARU was installed at the beam transportation tunnel. This length of the new linear accelerator has a length of approximately 50-m-long and it is a half-length of the previous one. The new one employed the microwave frequency of approximately 6 GHz (C-band microwave) and it is double frequency of the previous one (S-band microwave) to shortening the length.

The commissioning of NewSUBARU phase II started from April 20, 2021. After the beamline tuning, user time is operated at electron beam current of 350 mA in electron energy of 1.0 GeV top-up mode. In addition, 1.5 GeV operation will be started at the same time. The construction of the new injector has been completed in cooperation of the SPring-8 accelerator team. We would like to appreciate the SPring-8 accelerator team for their huge contributions.

Takeo Watanabe

Takeo Watanabe

Director of Laboratory of Advanced Science
and Technology for Industry,
University of Hyogo

The Organization of
Laboratory of Advanced Science and Technology for Industry
University of Hyogo

The organization

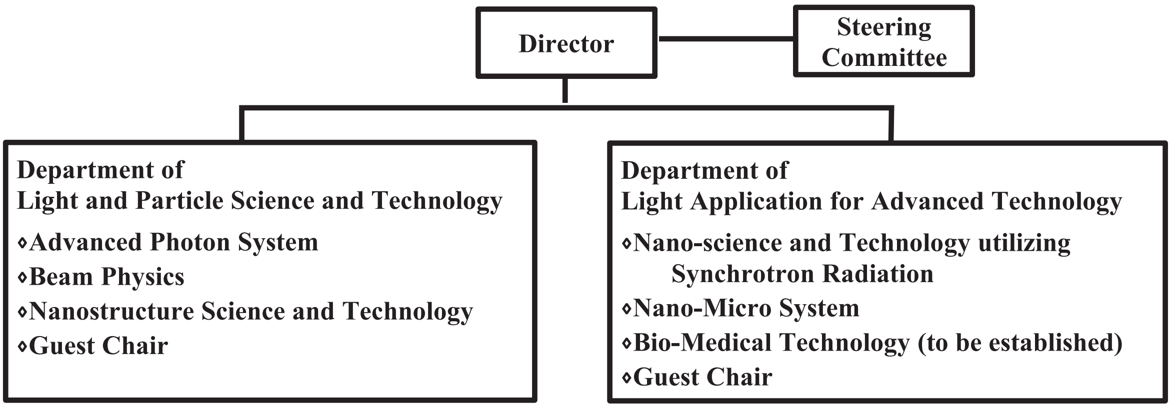
Director

Steering Committee

Department of Light and Particle Science and Technology
- **Advanced Photon System**
- **Beam Physics**
- **Nanostructure Science and Technology**
- **Guest Chair**

Department of Light Application for Advanced Technology
- **Nano-science and Technology utilizing Synchrotron Radiation**
- **Nano-Micro System**
- **Bio-Medical Technology (to be established)**
- **Guest Chair**

Staff (FY 2020)

Research and faculty staff
WATANABE Takeo, Professor, Director
KANDA Kazuhiro, Professor
UTSUMI Yuichi, Professor
SUZUKI Satoru, Professor
NIIBE Masahito, Associate Professor
SHOJI Yoshihiko, Associate Professor
HARUYAMA Yuichi, Associate Professor
YAMAGUCHI Akinobu, Associate Professor
HASHIMOTO Satoshi, Associate Professor
HARADA Tetsuo, Associate Professor
AMANO Sho, Research Associate
FUJII Satoshi, Research Associate
YAMAKAWA Shinji, Research Associate

Specially appointed staff
TERANISHI Nobukazu, Professor
MIYAMOTO Shuji, Professor
NAKANISHI Kouji, Associate Professor

Administrative staff
HAYASHI Masahiko, General Manager
HIROKAGA Yasuhiro, Manager
KAYAHASHI Hidetoshi, Chief
KUWATA Ayami, NewSUBARU
HASEGAWA Miwa, CAST
AKAMATSU Sumiyo, CAST
YOSHIDA Mizuho, CAST
KONO Kimi, CAST
MAEDA Yasuhide, CAST
SENBA Ayako, CAST
KUSUMOTO Kumi, CAST

Coordinator
MIYAMOTO Shuji, NewSUBARU

Guest staff
KUDOU Hiroto, Professor
HORIBE Hideo, Professor
BAN Hiroshi, Professor
HARADA Yoshihisa, Professor

Contact address

Advanced Research Building
3-1-2 Kouto, Kamigori-cho, Ako-gun, Hyogo, 678-1205 JAPAN.
T:+81-791-58-0249 F:+81-791-58-0242
NewSUBARU Synchrotron Radiation Facility
1-1-2 Kouto, Kamigori-cho, Ako-gun, Hyogo, 678-1205 JAPAN.
T:+81-791-58-2503 F:+81-791-58-2504
Web URL http://www.lasti.u-hyogo.ac.jp/, http://www.lasti.u-hyogo.ac.jp/NS/
e-Mail lasti@lasti.u-hyogo.ac.jp
Access http://www.lasti.u-hyogo.ac.jp/NS-en/access/

CONTENTS

Part 1. Current Status of NewSUBARU and Other Light Source

Part 2. Research Activities

List of publications

Part 1. Current Status of NewSUBARU and Other Light Source

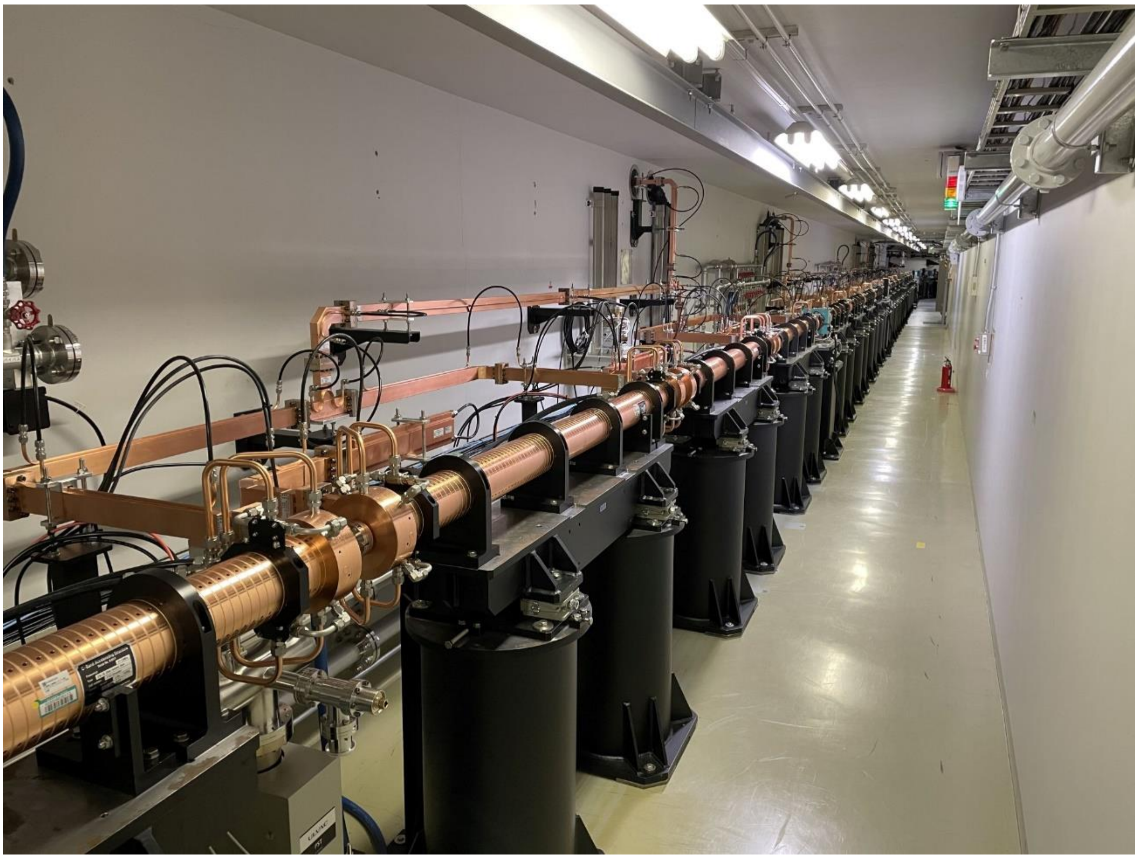

New Injector Linac

Electron storage ring and new injector linac at NewSUBARU

Satoshi Hashimoto
LASTI, University of Hyogo

1. Introduction

NewSUBARU synchrotron light facility has a 1.5 GeV electron storage ring, which is the largest accelerator among universities in Japan. The general layout of the ring is shown in Figure 1. The ring is consisted with 6 DBA cells with an inverse bending magnet. There are 6 straight sections between each cell, and they are used for an injection septum, an accelerating RF cavity, three undulators. The main parameters of the ring are listed in Table I.

The 1.0GeV linear accelerator (linac) of SPring-8 had been supplying electron beams for over 20 years, but shut down in August 2020. Therefore, a new 1.0GeV linac dedicated to the NewSUBARU ring was constructed with the help of SPring-8 accelerator staff. Construction of the new linac was completed at the end of 2020 and succeeded in accelerating the beam in March 2021. The construction and commissioning of the linac will be reported in detail in Section 5.

2. Operation Status of the ring in FY2020

The ring has two operation modes for user-time, 1.0 GeV top-up mode and 1.5 GeV current decay mode. The basic operation time is 9:00 - 21:00 of weekdays. Monday is used for machine R&D, Tuesday is for 1.5 GeV user time, Wednesday and Thursday are for 1.0 GeV top-up user time, Friday is for 1.0 GeV or 1.5 GeV user time. Weekday night and weekend can be used for additional machine study or user time with the special mode, such as a single bunch operation or an operation with arbitrary electron energy. Range of the electron energy is from 0.5 GeV up to 1.48 GeV with 1 MeV step.

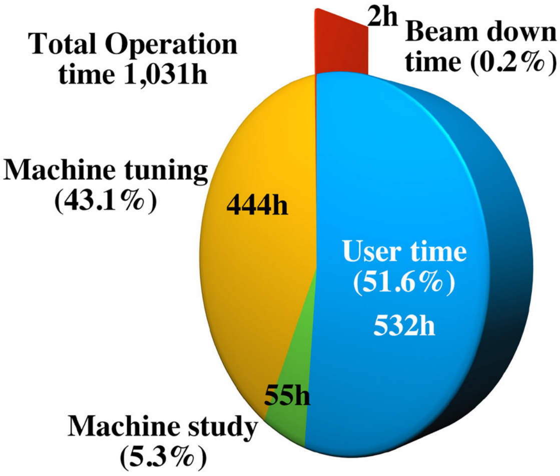

Fig. 2. Operation time of NewSUBARU in FY2020.

Due to the injector construction that started in August, the user-operation of the ring in FY2020 was completed in July. The total machine time in FY2020 was 1,031 hours, 38% of that of FY2019, excluding the beam down time and including machine tuning with the new

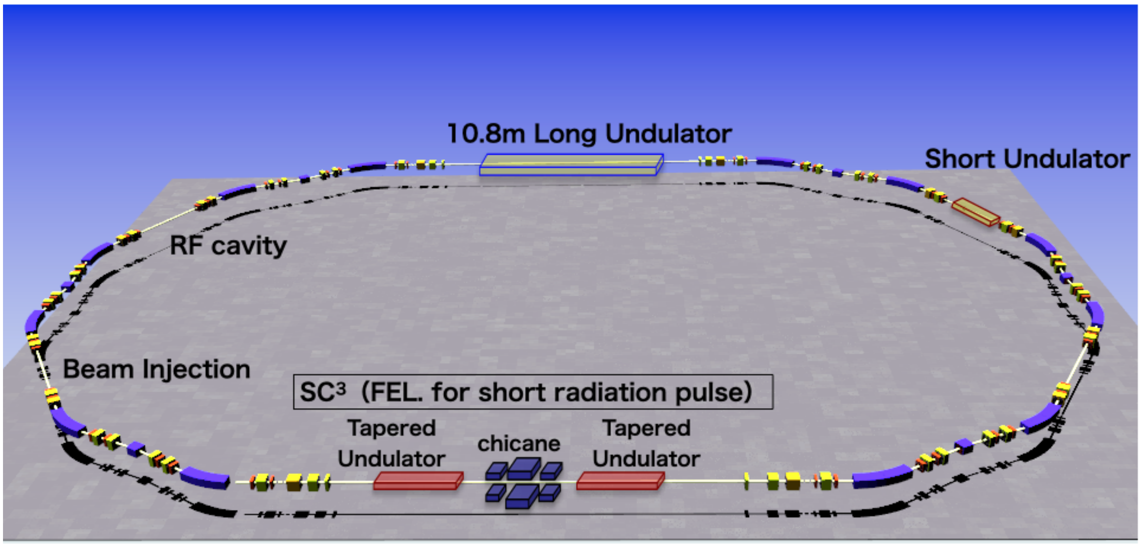

Fig.1. General layout of the NewSUBARU storage ring. Electron beams are injected from the newly-constructed 1.0 GeV linac dedicated to the NewSUBARU ring.

linac in February and March 2021. Figure 2 shows the breakdown of the ring operating time. The beam down time includes not only the down due to machine trouble, but also the off-beam period after the beam is aborted due to beam instability or erroneous operation. The total down time in FY2020 was 2 hours, 0.2 % of the total operation time. The machine's tuning time is long because all February and March operations were linac tuning.

Table I Main parameters of the NewSUBARU storage ting

Circumference	118.73 m
Lattice	DBA + inv. Bends
Number of bends	12
Radius of curvature	3.217 m
RF frequency	499.955 MHz
Harmonic number	198
Betatron tunes	6.29(H), 2.22 (V)
Number of IDs	3
Radiation loss per turn	33.4 keV (@1.0GeV)
Energy acceptance	±0.85%
Injection repetition rate	1 Hz

3. Machine Trouble

Typical troubles for both hardware and software in FY2020 are as follows. The beam down time was only 2 hours.

3-1. Magnet power supply failure.

Power supplies for quadruple magnet families often showed “Heat” alarm at startup. Fluctuations in the current of the sextupole magnets were observed several times a year.

3-2. Failure of pulsed bump power supply.

At the moment of beam injection, several reductions in the accumulated current occurred. This was due to the aging of the thyratron in the bump magnet power supply. Replacing the thyratron solved the problem.

3-3. Failure of cooling fans in the RF klystron power supply.

After a long period of injector construction, it turned out that many air-cooling fans inside the klystron power supply had failed. Until the repair scheduled for the summer of 2021, it will be cooled with an external blower and spot cooler as an emergency measure.

4. Machine Study

In FY2020, the main theme of the ring R&D was SC^3 project. Another topic was getting the latest ring parameters in preparation for beam injection from the new injector into the ring.

4-1. SC^3 project (mono-cycle FEL)

Under the collaboration with RIKEN SPring-8 center, University of Hyogo Graduate School of Material Science and LASTI, we are running the SC^3 (Slippage-Controlled Coherent radiation by Chirped micro-bunching) project, where the generation of the extremely short radiation pulse corresponding to only a few wavelengths will be experimentally proved at NewSUBARU using arbitrary tapered undulators [1], a magnetic chicane and a chirped seed laser. Main parameters of modulator, radiator and chicane are shown in Table II.

Table II Main parameters of SC^3 insertion device.

[Modulator/Radiator]

magnet	permanent
wavelength	15 cm
Number of periods	24
Total length	7.2 m
Max. field	0.7 T
Max. K parameter	10
Gap	280~50 mm

(gap can be longitudinally tapered)

[Chicane]

Magnet	Electromagnet
Number of coils	Main x1, Sub x2
Total length	600 mm
Max. field	0.7 T

Fig. 3. Insertion device for generating mono-cycle FEL light pulse. Modulator and radiator with high K parameter and a magnetic chicane between them.

The installation of undulators, a laser system, and a high-precision timing system were completed in FY2019. The first beam experiment started in April 2020. A single bunch electron beam could be stored at closest ID gap of 50 mm. Figure 4 shows the measured horizontal and vertical tune shifts caused by the strong magnetic field of the undulator. During the experiment, this vertical tune shift is corrected by a real-time tune correction system. Spontaneous radiation was successfully measured at various gaps. Additional tuning for the FEL experiment, including the overlap of electron beams and seed laser pulses in both space and time, began in April 2021.

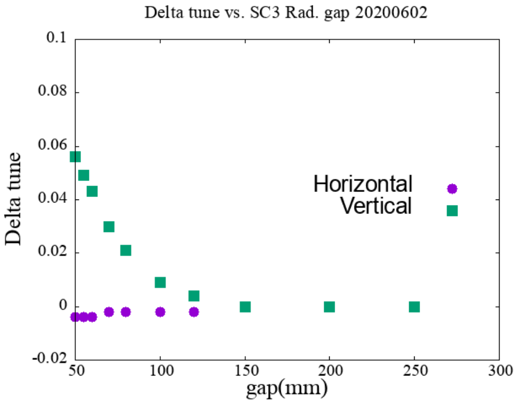

Fig. 4. Horizontal and vertical betatron tune shifts vs. SC3 radiator gap.

4-2. Another studies

Several studies have been done on the ring to smoothly inject the electron beam into the ring with the new linac. For example, measuring lattice functions and circulating beam parameters, optimizing pulsed magnets for injection, and readjusting the beam monitor.

5. Construction and Commissioning of New Injector Linac

Our storage ring has been supplied with electron beams from 1.0 GeV electron linac of SPring-8 as shown in Figure 5. However, RIKEN SPring-8 center/JASRI decided to shutdown this linac and to inject electron beams from 8.0 GeV linac of SACLA to the SPting-8 main ring. Therefore, a new 1.0 GeV injector is needed, and with the cooperation of RIKEN SPring-8 center and JASRI, we constructed a new linac dedicated to NewSUBARU ring.

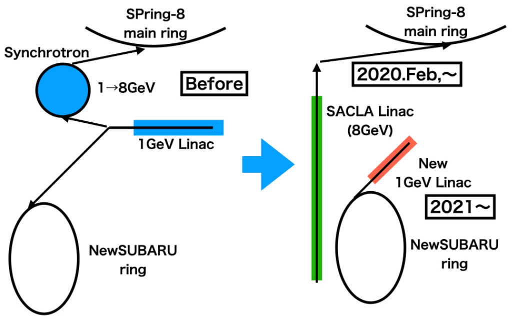

Fig. 5. Conceptual diagram of beam injection of SPring-8 and NewSUBARU. Before the shutdown of 1.0 GeV linac (left) and now (right).

5-1. General description of the injector linac

This section describes the main configurations of the injector linac [2]. This injector features a simple and sophisticated buncher and accelerator configuration. It has a C-band high-gradient accelerating structure and is characterized by being inexpensive and compact. This injector linac design is also used at the 3 GeV synchrotron radiation facility in Sendai [3].

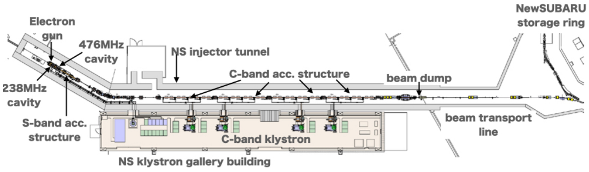

Fig. 5. General layout of the new 1.0 GeV linac.

The general layout of the injector linac is shown in Figure 5. The main characteristics of the injector linac are as follows [3].

50 kV gun using gridded thermionic cathode

A composite RF gun with a gridted thermionic cathode is used for generating stable and low emittance beam [4]. Stable emission of short pulse beams is achieved without any special tuning. Figure 6 and 7 show the electron gun and 238 MHz RF cavity.

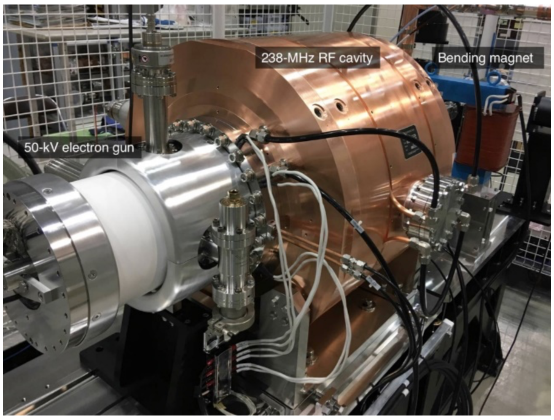

Fig. 6. 50 kV gridded themionic electron gun and 238MHz RF cavity.

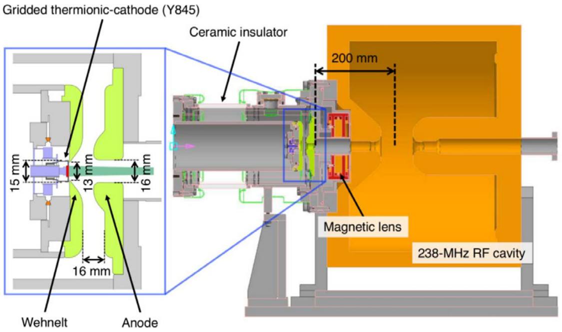

Fig. 7. Gridded themionic electron gun inside 238MHz RF cavity [4].

238 MHz cavity

The electron gun and focusing magnetic lens are mounted in a 238MHz cavity as shown in Figure 7. The 50 keV beam emitted by the electron gun is accelerated by the cavity up to 500 keV to suppress emittance growth due to space charge. The cavity is driven by 42 kW solid state amplifier.

476 MHz cavity

The following 476 MHz cavity provides velocity bunch compression. It decelerates beams from 500 KeV to 270~360 keV providing the energy chirp. Velocity bunch compression reduces the bunch length from 200 ps (FWHM) to several ps at S-band first cavity.

S-band accelerating structure

As shown in Figure 8, one S-band accelerating structure is used to accelerate the electron beam up to 50 MeV.

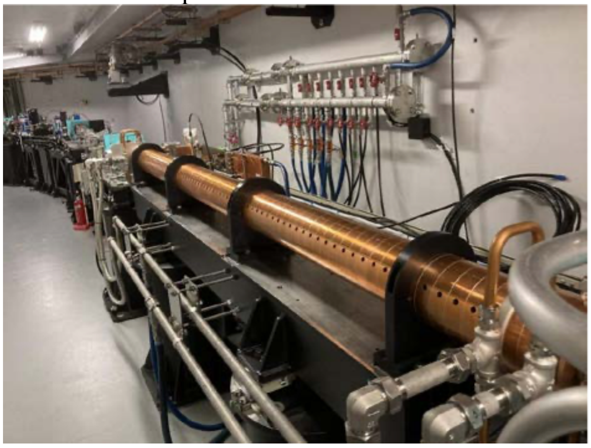

Fig. 8. S-band accelerating structure.

C-band accelerating structure

C-band accelerating structure shown in Figure 9 is the same type as SACLA. It is well proven and has a high acceleration gradient of about 31 MV / m [5]. The length of one acceleration tube is 2m. One unit (8.6m, 250MeV) consists of four acceleration tubes and is driven by a C-band klystron. Four units are used for 1.0 GeV acceleration.

Beam dump

A beam dump and a vertical bending magnet are installed downstream of the C-band accceleration tubes as shown in Figure 10.

Beam transport line

Figure 11 shows the designed envelope functions of the beam transport line from the exit of the linac to the injection point of the ring. The electron beam from the injector is transported to the ring without loss.

Fig. 9. C-band linear accelerating structure of the new 1.0 GeV linac.

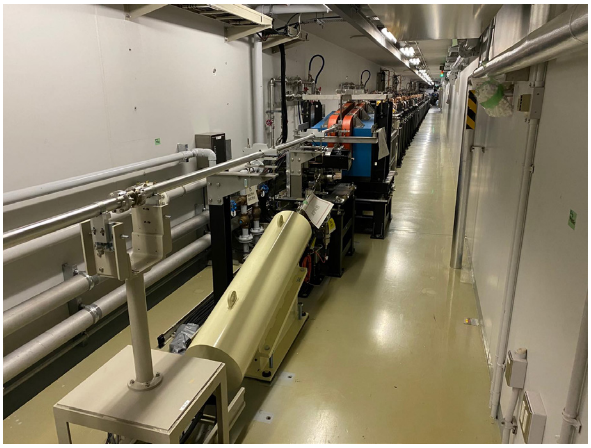

Fig. 10. Beam dump and vertical bending magnet.

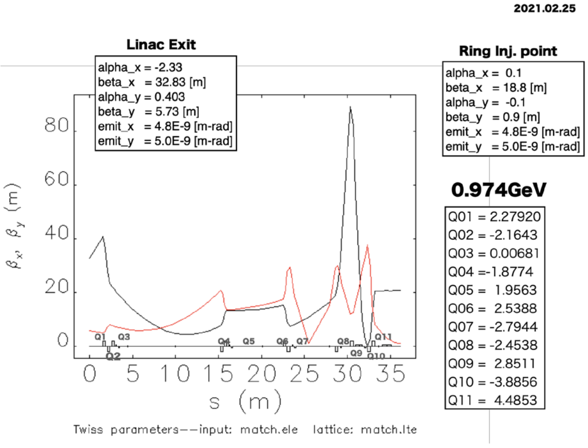

Fig. 11. Beam envelope functions of the beam transport line from the exit of the linac to the injection point of the ring.

5-2 Construction and commissioning history

Normal user operation in 2020 ended in July. Removal of existing equipment in the beam transport tunnel and construction of the new linac began in August. Construction of the new linac was completed by December. Despite the COVID-19 pandemic, there was no delay in the work process. RF conditioning of the klystrons and acceleration tubes was carried out for about a month and a half until mid-February 2021. The beam commissioning began in February and the 1.0 GeV electron beam was successfully transferred to the beam dump on February 17. Beam injection into the ring began on March 8, and the first synchrotron light from electrons supplied by the new linac was observed on March 9. A beam accumulation of 200 mA was achieved on March 11. User operation restarted on April 20 with a top-up current of 350 mA. This is about 3 weeks faster than planned. Table III summarizes the history of injector linac construction and commissioning.

Table III Construction and commissioning history of the new injector linac.

- Feb, 2017	Accelerator design
- Mar. 2019	Annex building constructed
- Jan. 2020	Install klystron & modulator
- July.	Storage ring shut down
	Remove beam transport line
- Oct.	Install linac in tunnel
- Jan. 2021	RF conditioning
- Feb.	Beam commissioning
	1 GeV, 100 pC beam
- Mar. 9	First light at storage ring
	Injection efficiency > 90%
- Apr. 20	User run restarted
	1-1.5 GeV, 350 mA

5-3. Benefits of the new injector linac

Table IV shows the performance required for the injector and its measurement results. We obtained sufficient performance of the beam. Also, linac is working very well without any problems.

Table IV Performance of the new injector linac.

	Require	Measurement
Beam Energy	1.0 GeV	1.0 GeV
Bunch charge	100 pC	100 pC
Normalized emittance	<10 mm-mrad	<10 mm-mrad
Energy spread	<±0.5%	0.1% (FWHM)
Energy stability	-	0.4% (STD)
Bunch length	5ps (FWHM)	<1ps (FWHM)
Injection efficiency	>90%	>90%

Having an injector that can be used exclusively has several advantages. First, we can schedule the operation of the machines according to the needs of the users in the facility. Second, we can inject the beam into the ring at any time and tune the injector linac at any time to increase the beam intensity or injection efficiency. Third, the beam quality is better than the previous Linac. As a result, the top-up current increased from the previous 300 mA to 350 mA. Due to its high long-term stability and reproducibility, the daily accelerator tuning time is short.

Summary

In FY2020 the new 1.0 GeV injector linac for NewSUBARU ring was constructed. We obtained sufficient performance of the beam. The stability and the reproducibility of the beam are also good. We re-started user time in April 2021.

The sophistication of accelerators will enable further contributions to the industrial use of synchrotron radiation.

Acknowledgements

We would like to express our sincere gratitude to the accelerator staff at RIKEN SPring-8 center, JASRI, QST, and SES for their great cooperation in the construction and operation of the new injector. We would also like to thank to Mr. Y. Minagawa, Mr. K. Kajimoto, Mr. H. Hirayama, Mr. S. Nakata of SES, and Mr. Y. Hamada of JASRI for their efforts in operating the accelerators.

References

[1]“Development of an undulator with a variable magnetic field profile”, T. Tanaka, Y. Kida, R. Kinjo, T. Togashi, H. Tomizawa, S. Hashimoto, S. Miyamoto, S. Okabe, Y. Tanaka, Journal of synchrotron radiation 28, p .404-409（2020）

[2]"Construction of a Compact Electron Injector Using A Gridded Rf Thermionic Gun And A C-Band Accelerator", T. Inagaki†, T. Fukui, T. Hara, T. Hiraiwa, H. Maesaka, H. Tanaka, T. Asaka, H. Dewa, N. Hosoda, E. Iwai, C. Kondo, T. Magome, T. Ohshima, T. Sakurai, K. Yanagida, S. Inoue, K. Kajimoto, Y. Minagawa, S. Nakata, T. Seno, H. Sumitomo, R. Takesako, S. Tanaka, R. Yamamoto, M. Yoshioka, S. Hashimoto, IPAC2021, WEPAB039 (2021)

[3]http://www.slitj.tagen.tohoku.ac.jp/oldHP/about.html

[4] T. Asaka, et. al., Phys. Rev. Accel. Beams 23, 063401 (2020)

[5] T. Inagaki, et. al., PRST-AB 17, 080702 (2014)

Beamlines

Koji Nakanishi
LASTI, University of Hyogo

The arrangement of the beamlines in the NewSUBARU synchrotron radiation (SR) facility is shown in Fig.1. Total nine beamlines are operating in the NewSUBARU SR facility.

Four beamlines of BL01, 03, 06 and 11 were constructed until 1999. Three beamlines of BL07, 09 and 10 were started the operation from 2000.

BL02 beamline was constructed for the usage of LIGA in 2003.

BL03B beamline branched from the BL03 beamline propose for the usage of the EUVL (extreme ultraviolet lithography) microscope for the EUVL finished mask inspection.

BL05 was built in 2008 to perform industrial analysis by soft X-ray XAFS and PES. A major upgrade was started in 2020 for more effective use.

BL09B beamline branched from BL09 beamline for the usage of the EUV interference lithography to evaluate. And BL09C beamline branched from BL09B beamline for the usage of the thickness measurement of the carbon contamination originated to the resist outgassing during the EUV exposure.

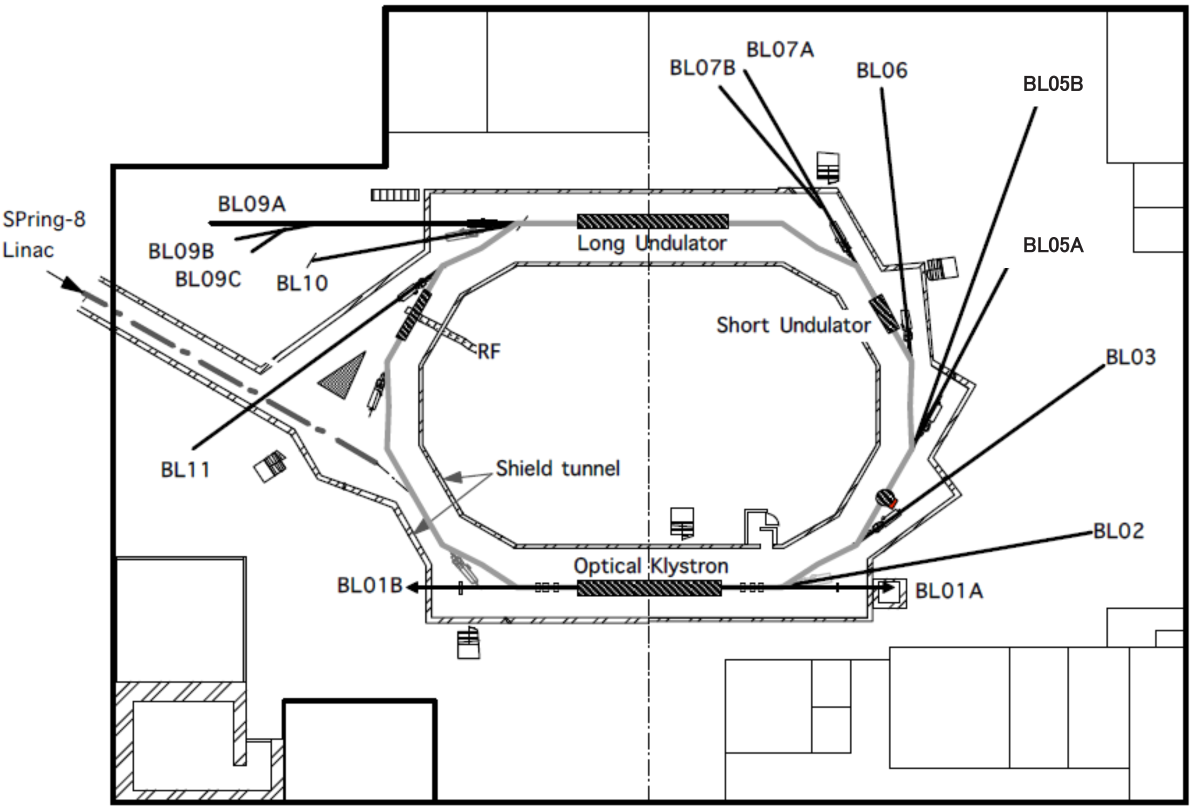

Fig. 1 Beamline arrangement in NewSUBARU.

I. BL01

BL01 is a beamline for research and developing new light sources. This beamline is one of two long straight section on NewSUBARU. Optical klystron was installed at this straight section. Upstream side of this beamline (BL01B) is intended to be used for visible and infrared light generated from free electron laser (FEL) or synchrotron radiation (SR). Downstream side of this beamline (BL01A) is used for laser Compton scattering gamma-rays source. Gamma-ray beamline hutch just outside of the storage ring tunnel was constructed in 2004 for gamma-ray irradiation experiments. Specification of this gamma-ray sources are listed in Table 1. New gamma-ray irradiation hutch "GACKO" was installed at BL01A, collaborating with Konan University. Table 2 shows the specification of "GACKO".

Table 1. Specification of BL01 gamma beam

CO_2 laser 10.52 μm 5W	Gamma energy : 1.7 - 4 MeV Gamma flux*: 9×10^{6} γ/s : 6×10^{5} γ/s (1.5-1.7 MeV) (with 3mmφ collimator)
Nd laser 1.064 μm / 0.532 μm 5 W	Gamma energy : 17 - 40 MeV Gamma flux*: 7.5×10^{6} γ/s : 3×10^{5} γ/s (15-17 MeV) (with 3 mmφ collimator)

*Electron beam energy : 1-1.5 GeV
*Electron beam current : 250 mA
*Gamma-ray beam divergence : 0.5 mrad

Table 2. Specification of "GACKO"

Maximum gamma-ray power	0.33 mW
Maximum gamma-ray energy	1.7 MeV - 73 MeV
CO_2 laser, wavelength/power	10.59 μm / 10W
1-1.7 MeV gamma-ray flux	2×10^{7} γ/sec@10W/300mA
Nd:YVO_4 laser, wavelength/power	1.064 μm/ 30W, 0.532 μm/ 20W
10-17 MeV gamma-ray flux	5×10^{7} γ/sec@30W/300mA

II. BL02

The LIGA (abbreviated name of Lithogaphic, Galvanoformung and Abformung) process which consists from deep X-ray lithography, electroforming, and molding process is one of the promising candidates for such 3D micofabrication. More than hundreds aspect ratio for microstructure can be attained by the usage of the higher energy X-rays (4-15 keV) from synchrotron radiation (SR) with deeper penetration depth to the photosensitive resist. In this system we have succeeded to enlarge the exposure area up to A4 size and the fabrication dimension from submicron to millimeter by varying the energy of the X-ray source in accordance with the size of desired microparts. Microstructure with high aspect ratio over several hundred will be achieved using the X-rays over 10 keV since high energy X-ray has deep penetration depth to the photo-sensitive resist materials. Whereas, in the case of lithography for low energy X-rays from 1 keV to 2 keV, submicron structures with high aspect ratio will be achieved using the X-rays mask with precise line-width and thinner absorber, since low energy X-rays has low penetration depth. Based on this principle, the beamline for x-ray exposure have constructed with continuous selectivity of X-rays from 100 eV to 15 keV by using the X-ray mirrors (plane and cylindrical mirror) and Be film filters. The horizontal angle of the outgoing SR could be obtained up to 12.5 mrad, which corresponds to the horizontal size of 220 mm (A4 horizontal size) at the exposure position. The second characteristic performance of the beamline is the high efficiency differential pumping system. This was necessary for maintain the vacuum difference between the storage ring ($<10^{-9}$ Pa) and the end-station ($<10^{-9}$ Pa) at which gasses for substrate cooling will be introduced in the exposure apparatus.

The flexibility for the shapes and functions of microstructure will be enlarged by achieving 3D microfabrication process using multi step exposure at various configuration between X-ray mask and substrates. The relative positions between X-ray mask and substrates, tilt and rotation angle to the SR incident direction can be moved simultaneously during SR exposure using 5 axis stages. The movement of each axis is controlled by the PC in terms of the scanning speeds, scanning length, and repetition number. In order to decrease the heat load of sample substrate suffered during SR irradiation helium introduction and substrate cooling mechanism were also equipped. Specification of spectrometer is listed in Table 3.

Table 3. Specification of the LIGA exposure system

Optics	Plane and cylindrical mirror, Be filters
Exposure energy	0.1 - 2 keV, and 4 – 15 keV
Exposure method	Proximity and multi-step exposure
Wafer size	A4 or 8 inch
Exposure area	230 mm(H) ×300 mm(V)
Exposure environment	< 1 atm (He-gas)

III. BL03

BL03 is a beamline for the developing the next generation lithographic technology so called extreme ultraviolet (EUV) lithography. The extreme ultraviolet lithography (EUVL) is a promise technology for fabricating a fine pattern less than 7-nm node. There are (1) a EUV resist-sensitivity evaluation tools, (2) a VUV reflectometer, and (3) an EUV microscope with Schwarzschild optics. At (1) tool, EUV resist is exposed with SR light of EUV monochromatized by 7 Mo/Si multilayer mirrors. The exposure spectrum of this tool was same as the ASML exposure tools. The monochromator of (2) reflectometer was UV – VUV reflectometer. At EUV lithography, out-of-band radiation (100 – 300 nm) of EUV source degrades image quality. Thus, optics and resist property of out-of-band region was essential to evaluate, for example EUV mask reflectivity, and EUV resist sensitivity. The monochromator specification was shown in Table 4. The EUV microscope (3) has Schwarzschild optics, which were fabricated with collaboration of Dr. Toyoda (Tohoku Univ.). The spatial resolution was quite high of less than 28 nm, which was equal to 7 nm at wafer printing size.

Table 4. VUV monochromator specification

Mount type	Collimate plane grating monochromator
Grating	Plane Grating (1,000 lines/mm)
Energy range	4 - 120 eV (UV ～ VUV)
Resolving power (E/ΔE)	～1000

IV. BL05

BL05 was constructed in response to a demand in the industrial world, which is enhancement of the analysis ability in the soft x-ray region with the development of nanotechnology. BL05 consists of two branch lines for use in the wide range from 50 eV to 4000 eV. BL05A and BL05B are designed to cover the energy range of 1300-4000 eV and 50-1300 eV, respectively. The incident beam from the bending magnet is provided for two branch lines through different windows of a mask. Therefore, these two branch lines can be employed simultaneously.

However, both beamlines have not been used as much in industrial analysis as expected due to the low accuracy of obtained spectra and the long acquisition time.

1) BL05A

In order to solve these problems, we first started to improve BL05A. In order to improve the basic beamline performance of BL05A, most of the optical elements, measurement system, and control program were replaced. For example, a Golovchenko-type double-crystal monochromator capable of high-speed scanning was newly installed to shorten the XAFS acquisition time. In addition, newly designed and installed masks and slits have made it possible to use high-intensity X-rays. Two toroidal mirrors as a collimated mirror and a focusing mirror have been used in the BL05A so far, but the focusing mirror was temporarily removed. The total electron yield mode with a sample current and the partial fluorescence yield mode with a silicon drift detector and a digital X-ray processor can be used for soft X-ray XAFS measurements. Table 5 shows the specification of monochromator.

Table 5. Monochromator specification

Monochromator	Double crystal monochromator
Monochromator crystals	Beryl(10-10), KTP(011), InSb(111), Ge(111), Si(111)
Energy range	1300 - 4000 eV

2) BL05B

The constant-deviation monochromator consisting of a demagnifying spherical mirror and a varied-line-spacing plane grating (VLSPG), which can provide high resolution, simple wavelength scanning with fixed slits, was mounted on BL05B. The optical system consists of a first mirror (M0), a second mirror (M1), an entrance slit (S1), a pre-mirror (M2), and three kinds of plane grating (G), an exit slit (S2) and a focusing mirror (M3). The including angle of the monochromator is 175°. Two measurement chambers for XAFS and PES are prepared at the end station of BL05B. The XAFS spectra in the total electron yield mode and fluorescence XAFS spectra using SDD (Ourstex) can be measured in a high vacuum chamber. In addition, the photoelectron spectrum can be measured using spherical electron analyzer (VG Sienta, R3000) in an ultrahigh-vacuum chamber. The chambers can be replaced by each other within 1 hour. Table 6 shows the specification of the monochromator.

Table 6. Monochromator specification

Monochromator	Varied-line-spacing plane grating monochromator
Grating	100 lines/mm, 300 lines /mm, 800 lines /mm
Energy range	50 - 1300 eV
Resolution	E/⊿E=3000

V. BL06

BL06 has been mainly developed for irradiation experiments such as photochemical reaction, SR-CVD, photo-etching, surface modification. The white radiation beam from bending magnet is introduced to the sample stage using a pair of mirrors, whose incident angle was 3°. The SR at BL06 sample stage had a continuous spectrum from IR to soft x-ray, which was lower than 1 keV. A differential pumping system can be utilized for experiments in a gas atmosphere, which is difficult in the soft x-ray region. A sample holder can install four pieces of samples at a time. By using heater set in the sample holder, the sample can be heated from room temperature to 220°C. The temperature of sample is monitored using a Cr-Al thermocouple mounted on the sample holder.

The current BL06 for irradiation experiments was closed due to plans to build a new beamline for XAFS in August 2020. Irradiation experiments will be partially possible at the newly constructed beamline.

VI. BL07

This beamline was designed for the development of new materials by SR technology. This beamline consists of two branch lines, which are provided with an incident beam from a 3-m-long undulator by switching the first mirror. One of them is a high photon-flux beamline with a multilayered-mirror monochromator for the study of SR-process (BL07A) and another is a high-resolution beamline with a varied line spacing grating monochromator for the evaluation of nano-structure characteristics by SR-spectroscopy (BL07B). The useful range of emitted photons from 50 to 800 eV is covered at both beamlines. The light source of BL07 is a 3-m length planar undulator, which consists of 29 sets of permanent magnets, a period length of which is 76 mm. The incident beam from the undulator is provided for two branch lines by translational switching of first mirror.

1) BL07A

The multilayered-mirror (MLM) monochromator, which has high reflectivity in the soft X-ray region, was installed at the BL07A. It consists of a switching mirror chamber, a slit chamber, a MLM monochromator, a filter chamber and a reaction chamber. To obtain a large photon flux, we decided to use only first mirror (switching mirror), M0, for focusing. The MLM monochromator is designed to cover an energy range of up to about 800 eV by combination of three kinds of mirror pairs with 4 kinds of filter. The flux deliver by this design is estimated to be between a maximum of 10^{17} photons/s at 95 eV and a minimum 2×10^{14} photons/s at 300 eV for a 500 mA ring current. Table 7 shows the summary of BL07A. In addition, X-ray fluorescence (XRF) apparatus using spherical varied line spacing grating was mounted at the downstream of irradiation chamber. The poly capillary was used to enhance beam-condensing efficiency. Measurement energy range was from 30 eV to 450 eV. This XRF apparatus was expected to utilize the chemical analysis on the light metals, Li and Be, and light elements, B, C and N.

Two novel vacuum chambers were installed in 2019 for the measurement of inverse Compton scattering of soft X-rays. One large chamber with a size of W1120×D820×H610 mm3 was set up 16.7 m downstream of the undulator center. A multi-layer mirror was placed on high precision auto-stages inside this chamber with cooling water circulation. The other chamber was installed 2.6 m upstream of the large mirror chamber, in order to monitor radiated and reflected X-rays.

Table 7. Summary of BL07A.

Energy range (eV)	Multilayer mirror					Filter	
	Material	Spacing	Thickness Ratio	Number of layers	ΔE/E	Material	Thickness
50-60	Mo/Si	20 nm	0.8	20	6.2 %	Al	100 nm
60-95						None	-
90-140	Mo/B_4C	11 nm	0.5	25	3.3 %		
140-194						Ag	100 nm
190-400	Ni/C	5 nm	0.5	60	2.5 %		
400-560						Cr	500 nm
550-800						Ni	500 nm

2) BL07B

The constant-deviation monochromator consisting of a demagnifying spherical mirror and varied line spacing plane grating (VLSPG), which can provide to high resolution, simple wavelength scanning with fixed slits, was mounted on BL07B. The optical system consists of a first mirror (M0), an entrance slit (S1), a pre-mirror (M1), and three kinds of plane grating (G), an exit slit (S2) and two focusing mirrors (M2 and M3). The monochromator is designed to cover the energy range 50-800 eV with three gratings, of which including angle are 168°. The VLSPG has been well known to obtain high resolution in extreme ultraviolet region by diminishing various kinds of aberration. The total resolving power about 3000 can be realized in the whole energy region. Table 8 shows the specification of the monochromator.

Table 8. Monochromator specification

Mount type	Hettrick-Underwood type
Grating G1, G2, G3	Plane VLS (600, 1200, 2400 l/mm)
Energy range	50-150 eV, 150 – 300 eV, 300-800 eV
Resolving power (E/ΔE)	～3000

VII. BL09

A purpose of this beamline is studies on a soft x-ray interferometry or a holographic exposure experiment with making use of highly brilliant and coherent photon beams radiated from 11 m long undulator in NewSUBARU.

BL09 consists of M0 mirror, M1 mirror, G grating and M2 mirror. M0 mirror is used for horizontal deflection and beam convergence, M1 is used for vertical beam convergence at the exit slit, and M2 is used for vertical deflection and beam convergence. A monochromator is constructed by M1 and a plane grating. The maximum acceptance of the undulator beam is 0.64 mrad in horizontal and 0.27 mrad in vertical. The acceptance can be restricted by 4-jaw slits equipped at upstream of the M0 mirror.

1) BL09A

BL09A beamline is used for material analysis: X-ray absorption spectroscopy (XAS) and X-ray photoelectron spectroscopy (XPS). In 2013, X-ray emission spectrometer (XES) was introduced at the end-station of the BL-09A. The energy range and resolving power of the XES system was designed to be about 50-600 eV and 1500, respectively.

2) BL09B

BL09B beamline branched from BL09 beamline for the usage of the EUV interference lithography for the evaluation of the exposure characteristics of EUV resist. Coherence length of 1 mm at the resist exposure position was achieved using BL09B beamline. And BL09C beamline branched from BL09B beamline for the usage of the thickness measurement of the carbon contamination originated to the resist outgassing during the EUV exposure. Table 9 shows the specification of the monochromator.

Table 9. Monochromator specification

Mount type	Monk-Gillieson type
Grating	Plane VLS (300, 900, 1200 l/mm)
Energy range	50 – 750 eV
Resolving power (E/ΔE)	～3000

VIII. BL10

BL10 is for EUV reflectometry and soft X-ray analysis. M0 mirror is used for horizontal deflection and beam convergence, M1 is used for vertical beam convergence at the exit slit, and M2 is used for vertical deflection and beam convergence. A monochromator is constructed by M1 and a plane grating. At the beginning, the multilayer reflectivity measurement was carried out at this beamline. The characteristics of this beamline and the result of the Mo/Si multilayer measurement are carried out for the development of the EUV- mask technology.

BL10 utilizes a monochromator of the varied-line-spacing plane grating (VLS-PGM). The line density of the monochromator in central region of the gratings were 600, 1800 and 2,400 lines/mm. The reflectometer has a two-axis vacuum goniometer. One axis carries the sample, which may be a mirror surface at the center of the reflectometer vacuum chamber (θ-motion). The other (φ-motion) carries the detector on a rotating arm. In addition, there are linear motions to translate the sample in two orthogonal directions (x, y). All motors are controlled by computer. The reflectivity result obtained at BL10 has a good agreement with that at LBNL. Table 10 shows the specification the monochromator.

The micro-CSM tool was adapted at the most downstream of the BL10 beamline for the EUV mask defect inspection with coherent-diffraction-imaging method. This too is very effective for the inspection of the actinic patterned mask with phase imaging.

A large reflectometer was installed in a branch line for large EUV optical component including EUV collector mirrors. The reflectometer has a sample stage with y, z, θ, φ, and Tilt axis, which can hold large optical elements with a maximum weight of 50 kg, a diameter of up to 800 mm, and a thickness of 250 mm. The entire sample surface is able to be measured.

Table 10. Monochromator specification

Mount type	Monk-Gillieson type
Grating	Plane VLS (600, 1800, 2400 l/mm)
Energy range	50 – 1,000 eV
Resolving power (E/ΔE)	～1000

IX. BL11

A beam line BL11 is constructed for exposure Hard X-ray Lithography (DXL) in the LIGA (German acronym for Lithographite Galvanoformung and Abformung) process. LIGA process, that utilizes a useful industrial application of SR, is one of the promising technologies for fabrication of extremely tall three-dimensional (3D) microstructures with a large aspect ratio. This process was invented at the Institut Fur Mikrostrukturtechnik (IMT) of the Karlstuhe Nuclear Center (KfK) in 1980. Microstructures with height of over a few hundred μm have been widely applied to various fields such as micro-mechanics, micro-optics, sensor and actuator technology, chemical, medical and biological engineering, and so on. This beam line was designed by the criteria; photon energy ranges from 2 keV to 8 keV, and a density of total irradiated photons $\geq 10^{11}$ photons/cm^2. The BL11 can provide the most suitable photon energy for microfabrication in X-ray lithography, while the BL2 is equipped for fabricating fine pattern submicron-scale structure and microstructure with high aspect ratio by selectivity of X-rays using movable mirror system. That is, LIGA process in NewSUBARU can provide the best 3D microfabrication because the BL11 and BL2 are complementary. The beamline BL11 is consisting of an absorber chamber, a first-mirror chamber (M1), a 4-way slit chamber, a Be and polyimide window chamber, and an exposure chamber. The horizontal angle of the outgoing SR could be obtained up to 17.8 mrad, providing a beam spot size on the exposure stage $\geq 80 \times 10$ mm^2. The micron-scale structure with high aspect ratio will be achieved using the toroidal typed mirror M1 which can produce a parallel collimated beam of X-rays. In addition, the homogeneity of the beam is excellently controlled by a novel adding system.

Using the precision stage in the exposure chamber, the flexibility for the shaped and functions of microstructure will be enlarged by achieving 3D microfabrication process using multi step exposure at various configuration between x-ray mask and substrates. The exposure area of 200 mm × 200 mm is brought to fruition. In order to decrease the heat load of sample substrate suffered during SR irradiation, helium introduction and substrate cooling system were also equipped. The specification of the LIGA exposure system is listed in Table 11.

Table 11. Specification of the LIGA exposure system

Exposure method	Proximity exposure
Wafer size	8 inch
Exposure area	200 mm(H)×200 mm(V)
Exposure environment	< 1atm (He-gas)

Establishment of Research Center for Advanced Synchrotron Radiation Analysis

In order to respond to diverse analysis needs from industries, it is necessary to advance technological development for analyzing beamlines (BLs) of NewSUBARU SR facility to advance integrated and strategic development of analyzing technology. For this reason, the Research Center for Advanced SR Analysis was launched in August 2016. As an organization crossing in university courses, this center is consulted and administered by all members of the LASTI related to analysis, and in collaboration with the SR Nanotechnology Center of Hyogo Prefecture, a wide range of energy from hard X-rays to soft X-rays. We aim to respond to various analysis needs of the area on a one-stop basis.

Acknowledgement

We would like to thank all the staff who work at NewSUBARU synchrotron radiation research facility for their help to describe the update details of the beamlines.

Part 2. Research Activities

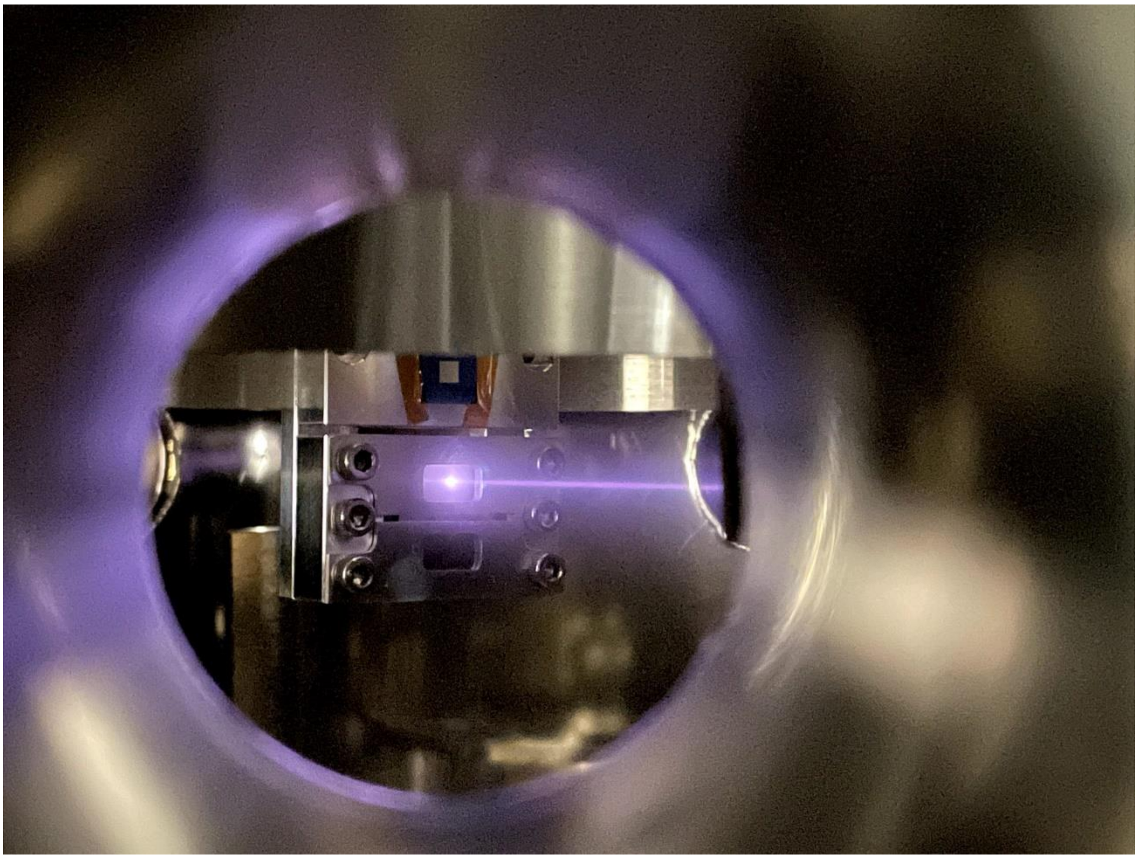

Hydrogen Plasma Emission

(BL-9C high-power EUV irradiation tool)

Application of Machine Learning Techniques to Betatron Tune Correction

H. Fujii[1], K. Watanabe[2], and S. Hashimoto[1]
[1]LASTI, [2]University of Hyogo

Abstract

In NewSUBARU synchrotron light facility, a real-time spectrum analysis is performed for betatron tune correction. However, the existing system is a handmade system and its range of application and accuracy are limited. In this study we developed a new system using logistic regression model, which is one of the simplest machine learning techniques. As a result, it was found that it is possible to construct a model with accuracy exceeding the existing system even with a relatively small amount of teacher datasets.

Introduction

The orbit of the electron beam orbiting the storage ring is given by the following orbit equation.

$$\frac{d^2x(s)}{ds^2} + K(s)x(s) = F(s). \qquad (1)$$

Where s is the position on the design orbit and $x(s)$ is the horizontal deviation from it. Since the vertical deviation is given in the same form, only the horizontal direction is considered below. $K(s)$ is a function representing the magnetic field of each electromagnet and satisfies $K(s+L) = K(s)$. L is the circumference of the ring. $F(s)$ mean the strength of the residual magnetic field on the design orbit. The periodic solution of Eq. (1) can be written as follows.

$$x(s) = \sum_{n=-\infty}^{\infty} \frac{\sqrt{\beta(s)}\nu^2 f_n}{\nu^2 - n^2} e^{\frac{in\psi(s)}{\nu}}. \qquad (2)$$

The aperiodic solutions decay, so it is not considered here. $\beta(s)$ is betafunction and satisfies $\beta(s+L) = \beta(s)$. $\psi(s)$ is a function that satisfies $\psi(s+L) = 2\pi\nu + 2\pi l + \psi(s)$, where l is an integer. ν is called *betatron tune*, or simply *tune*, which means the number of oscillations of the electron beam per round of the storage ring. n is an integer and f_n is the Fourier coefficient. Figure 1 shows the betatron oscillation.

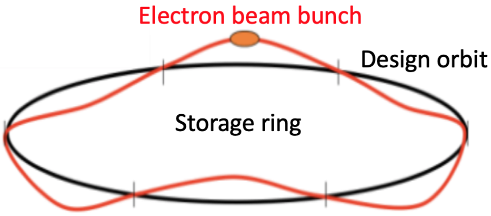

Figure 1. Schematic drawing of betatron oscillation of electron beam bunch. Residual magnetic field is not considered in this figure.

As is clear from the denominator of this solution, when tune value approaches an integer, $x(s)$ becomes large due to resonance with the residual magnetic field and the electron beam becomes unstable. In reality, there are various other resonance conditions. Then, in order to extend the lifetime of the electron beam, it is necessary to constantly monitor and correct the tune value to keep it away from the resonance conditions. Figure 2 shows the results of the tune measurement obtained in NewSUBARU storage ring.

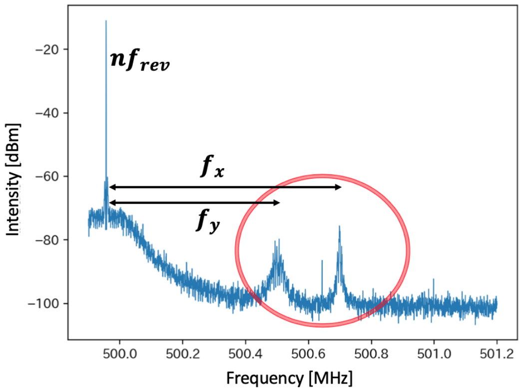

Figure 2. Frequency spectrum of voltage signal from beam positioning monitor on storage ring. nf_{rev} is n-th harmonics of the revolution frequency of the electron beam bunch. f_x and f_y are the frequency of horizontal and vertical betatron oscillation, respectively.

The peak around 499 MHz in Fig. 2 is from the higher harmonics of the revolution frequency of the orbiting electron beam bunch. The frequency of betatron oscillation is observed as its sideband. The peaks around 500.5 and 500.7 MHz are from the betatron oscillation in the vertical and horizontal directions, respectively. The tune value is obtained by dividing these frequencies by the revolution frequency. (To be precise, only the decimal part of the tune is obtained here.) In the current system, the spectrum in Fig. 2 is smoothed and then peak fitting is performed to obtain the tune. If the tune value is inappropriate, a correction is performed by changing the current value of the auxiliary winding of the quadrupole electromagnets. The problem here is that the peak fitting does not always work. Depending on operating conditions, for example, the peak may be too small or too large as shown in (a) and (b) of Fig. 3.

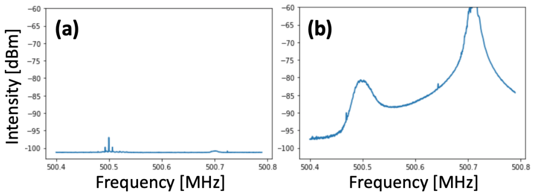

Figure 3. Bad frequency spectrum examples.

In such cases, correct tune value cannot be obtained and a wrong correction may be performed. To prevent this, the current system judges whether correction should be performed or not using various criteria such as peak height, full width at half maximum, and amount of change from the previous tune value. However, this method cannot be used to judge complicated waveforms. In addition, it is necessary to adjust the parameters of the criteria every time the operating status changes. Therefore, we construct a new judging system by using the machine learning techniques. In this study, we used logistic regression [1] which is one of the simplest methods for solving classification problems. In logistic regression, classification is performed using the following classification model,

$$p(z_l) = e^{z_l} \Big/ \sum_{k=0}^{K-1} e^{z_k}\,, \tag{3}$$

$$z_l = \sum_{j=0}^{M} w_j^{(l)} x_j\,. \tag{4}$$

This is called Softmax function. K is the number of classes $(0,1,2,\dots,K-1)$. In our case, $K=2$. (A correction should be performed: 0, or not: 1. In this case, the Softmax function is equivalent to the sigmoid function.) M is the number of features (or descriptors, explanatory variables). x_j is the value of the j-th feature. In our case, feature is spectral intensity at the observation points in the frequency spectrum. Here, $x_0 \equiv 1$ is a bias term (or a constant term). $w_j^{(l)}$ is the weight to be learned. Equation (3) reads the spectral data $x_0, x_1 x_2, \dots, x_M$ and returns a value with range from 0 to 1. Obviously, $\sum_{k=0}^{K-1} p(z_k) = 1$ and $p(z_l)$ represents a probability that the read data belongs to class l. Logistic regression is a method classified as supervised learning, and it is necessary to give a correct label in advance. Compare the estimated value from Eq. (3) with the correct label and then update the weight $w_j^{(l)}$. The update procedure is as follows: first, the loss function is defined by

$$J = -\sum_{k=0}^{K-1} t_k \ln[p(z_k)]\,. \tag{5}$$

This function means the estimation accuracy of the classification model. Here, t_k is a vector $\vec{t} = [t_0, t_1, t_2, \dots, t_{K-1}]$ which means the correct label expressed by one-hot encoding, i.e., it is a vector in which only the element of the correct label is one and the other elements are zero. The derivative of J by $w_j^{(l)}$ is

$$\frac{\partial J}{\partial w_j^{(l)}} = -[t_l - p(z_l)]x_j. \tag{6}$$

From this derivative, the following gradient descent method is use to update the weights.

$$w_j^{(l)} = w_j^{(l)} - \eta \frac{\partial J}{\partial w_j^{(l)}}. \tag{7}$$

In this way, the derivative can eventually reach 0 as the learning progresses. η is called the learning rate (or step size) that determines the magnitude of weight update. Repeat the above update procedure a specified number of times.

Experiments and Results

Figure 4 shows the percentage of correct answers to the number of teacher datasets used in the training of the logistic regression model.

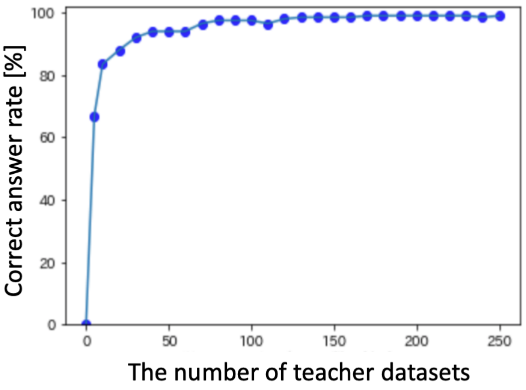

Figure 4. Correct answer rate of logistic regression model as a function of training datasets.

It can be seen from this figure that a model with a correct answer rate of 99.5% or more can be constructed even with a relatively small number of teacher datasets of about 140. The judgment processing time of this logistic regression model is about 0.03 s, which can be sufficiently used for real-time system. The performance of the conventional system is 99% correct answer rate and 0.01 s judgment time. Therefore, the logistic model is a little slower in speed, but higher in accuracy. Here, in this new system, the spectral data is integrated, and the data whose integrated value is too small or too large, such as (a) and (b) in Fig. 2, is excluded in advance to make learning a little easier. Even with such a simple machine learning model, it was possible to construct a model with high accuracy. In the future, we will construct a tune correction system using a more efficient machine learning model and use it for actual operation.

Reference

[1] C. M. Bishop, "Pattern Recognition and Machine Learning", Springer (2006).

Performance of BL07A at NewSUBARU with installation of a new multi-layered-mirror monochromator

Shotaro Tanaka, Shuto Suzuki, Tomohiro Mishima and Kazuhiro Kanda
LASTI, University of Hyogo, 3-1-2 Koto, Kamigori, Hyogo, Japan

Abstract

Soft X-rays excite the inner shells of materials more efficiently than any other form of light. The investigation of the synchrotron radiation (SR) processes by using inner-shell excitation requires the beamline to supply a single color and a high-photon-flux light in the soft X-ray region. A new integrated computing multi-layered mirror (MLM) monochromator was installed at the beamline 07A (BL07A) of NewSUBARU, which has a 3-m undulator as a light source for the irradiation experiments with high-photon-flux monochromatic light. The MLM monochromator has a high reflectivity index in the soft X-ray region; it eliminates unnecessary harmonic light from the undulator and lowers the temperature of the irradiated sample surfaces. The monochromator can be operated in a high vacuum, and three different mirror pairs are available for different experimental energy range; they can be exchanged without exposing the monochromator to the atmosphere. Measurements of the photon current of a photodiode (PD) on the sample stage indicated that the photon flux of the monochromatic beam was more than 10^{14} photons/s・cm^2 in the energy range of 80—400 eV and 10^{13} photons/s・cm^2 in the energy range of 400—800 eV. Thus, BL07A is capable of performing SR stimulated process experiments.

1. Introduction

Reaction processes originating from the excitation of inner-shell electrons of atoms are different from those originating from excitation of valence electrons, because the inner-shell electrons are localized within molecules. Specific atoms can be excited using inner-shell excitation because the binding energies are particular to each atom and the chemical bond environment. This ionic dissociation originating from the inner shell excitation shows contains information on the initial resonance excitation, namely, the transition from the inner-shell electron of a particular atom to an anti-bonding orbital and suggests the possibility of using inner-shell resonance excitation for site-selected chemical-bond cutting. This reaction process is especially interesting from the perspective of cutting specific chemical bonds through the control of light, i.e. as a "molecular scalpel". In addition, the soft X-ray region has the largest reaction cross section in the light spectrum for such cutting reaction. For these reasons, inner-shell excitation has attracted attention as a surface modification process at relative lower temperatures because it can cause a reaction without emitting extra energy. To excite inner shells of various elements, the energy of the light source must be tunable in the soft X-ray region, and synchrotron radiation (SR) is realistically the only available light source to serve this purpose. As well, a beam line with a high brightness beam is necessary to study inner-shell excitation reactions of a single color by using soft X-rays. Moreover, the beam line should be able to irradiate a sample’s surface with high-photon-flux monochromatic light.

In the work reported here, we installed a new multi-layered mirror (MLM) monochromator at beamline 07A (BL07A) in NewSUBARU Synchrotron Radiation Facility for experiments on inner-shell excitation in which irradiation with high-photon-flux monochromatic light produced by a combination of an undulator source and a multilayer film mirror monochromator.

The BL07A beamline was designed for investigating functional surfaces by using high-flux soft X-rays. It has a 3-m undulator to supply soft X-rays in the range of 80—800 eV [1]. In the previous studies, we performed various studies on surface modification processes by directly irradiating samples with the undulator light [2]. Many research results were obtained, such as one showing the crystallization temperature of polysilicon is 200 °C lower than what was previously believed [3]. However, there are two problems with irradiating a sample directly with undulator light, which includes multiple higher-order harmonics due to the undulator: (1) harmonics not at the desired energy become a heat source that needlessly raises the sample’s surface temperature; (2) the photon flux cannot be estimated because the sample is irradiated with multiple higher-order harmonics with different energies, and their intensity ratio cannot be evaluated. Therefore, we could not determine the reaction cross sections of inner-shell excitations at this beamline. To solve these problems, we installed a new MLM monochromator that can be operated under a high-vacuum, by setting two differential pumping chambers upstream and downstream of the monochromator (Fig. 1). Here, we report the experimentally estimated photon flux when using the new MLM monochromator under each irradiation condition at BL07A.

2. Beamline Overview

Beamline 7 (BL07) at NewSUBARU was constructed for researching the creation of new functional materials. For new-materials development using SR, two kinds of beamline are required in the soft X-ray region. One is a high-photon-flux and energy-tunable beamline for studying SR-stimulated processes, such as inner-shell excitation leading to selective photochemical reactions. The other is a high-resolution beamline for the analysis of the produced materials, such as by photoelectron spectroscopy and X-ray absorption spectroscopy. BL07 thus consists of two-branch lines. BL07A is a SR-stimulated reaction beamline using high photon-flux light; it has an MLM monochromator. BL07B is a material-analysis beamline; it has a constant-deviation monochromator, consisting of a demagnifying spherical mirror and varied line spacing plane grating (VLSPG). This type of monochromator can provide high resolution through simple wavelength scanning with fixed slits.

The light source of BL07 is a 3-m planar undulator, which consists of 29 sets of permanent magnets, the period length of which is 76 mm. The K parameter of the undulator ranges from 0.3 to 5.3, and the radiation wavelength from this undulator ranges from 66 to 4.4 nm when utilizing the fundamental and third through seventh higher harmonics. The brilliance of this undulator, which was calculated as 100 mA of the ring current (Miyamoto, 2001), is depicted in Fig. 2 (a) for 1.0-GeV operation mode and (b) for 1.5-GeV operation mode. Brilliance steeply decreases at photon energies more than 400 eV in 1.0-GeV operation mode. On the other hand, brilliance in 1.5-GeV operation mode remains high enough out to 800 eV. The incident beam from the undulator is provided for the two branch lines, BL07A and BL07B, by translational switching of the first mirror.

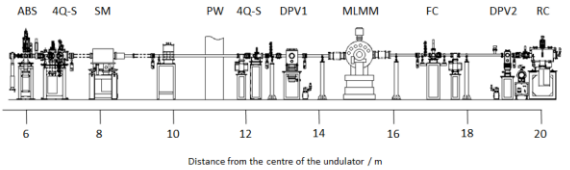

Figure 1 Layout of BL07A showing the position of beamline components. ABS: absorber; 4Q-S: four-quadrant slit; SM: switching mirror; PW: protective wall; DPV1: differential pumping vessel 1; MLMM: multi-layered-mirror monochromator; FC: filter chamber; DPV2: differential pumping vessel 2; RC: reaction chamber.

Figure 1 shows the overall setup of BL07A from the front end of the storage ring to the reaction chamber. The optical layout of BL07A does not change from the design was described in reference [1]. The front end consists of a mask, absorber and four-quadrant slit. The acceptance angles are 2.2 mrad horizontally and 2.4 mrad vertically. The first mirror, the switching mirror, is spherical with a radius of curvature of 312,400 mm. The center of the first mirror is located 8,174 mm downstream from the center of the undulator, and its incident angle is 3°. The first mirror is made of Si and its surface is coated with Pt. The induced undulator light is reflected by this mirror and propagates outside the protective wall as quasi-parallel light.

Undulator light reflected by the first mirror reaches the MLM monochromator, located 7,100 mm downstream from the center of the first mirror, through a four-quadrant slit and differential pumping vessel 1. As described in the introduction, we installed a new MLM monochromator that can operate in a high vacuum. This monochromator, MKZ-7NS (Kohzu Precision Co. Ltd.), is controlled with integrated computing, in which mechanically independent axes are programmatically controlled for keeping a fixed exit position. The Bragg angle can be varied from 9 to 65°. The beam offset of the monochromator is precisely 15 mm. This design reduces the convolution of mechanical errors, and the control mechanism is very compact. Three different pairs of mirrors can be selected and they can be exchanged without exposing the monochromator to the atmosphere. The details of the monochromator were reported by. Okui et al. [4].

A filter chamber and differential pumping vessel 2 are downstream of the MLM monochromator. The undulator light through a filter is introduced into the reaction chamber. A four-quadrant beam-forming slit is placed in front of the reaction chamber. The irradiation point of the sample in the reaction chamber is located at 11,927 mm downstream from the center of the first mirror. The reaction chamber has a load-lock system, and samples can be placed at the irradiation position without exposing the chamber to the atmosphere. The plane size of the sample holder is 70 mm long × 25 mm wide, and both sides of the sample holder can be used. The beam spot at the irradiation point is about 25 mm square. The intensity of light is made almost homogeneous in a 20 mm square around the center by checking with a 3-mm-square photoelectric board.

3. Experimental Setup and Results

The photon flux at the irradiation point was measured with a photodiode (PD), AUXV100 (International Radiation Detectors Inc.), whose light-receiving area was 10 mm square. The PD was placed about 205 mm downstream from the irradiation point in the reaction chamber. To confirm the linearity of the photocurrent from the PD against the photon flux, we measured the output current of the PD while varying the current of the storage ring. The output current of the PD showed good linearity in the range under 1.7 mA. The data sheet of the AUXV-100 indicates that its quantum efficiency has a temperature dependence of 0.045 %/°C. The temperature of the PD can be considered to depend on the quantity and energy of the irradiated X-rays. Unfortunately, we could not measure the surface temperature of the PD directly, because the reaction chamber does not have a window port for observing the PD's surface. Instead, we measured the surface temperature of a-Si thin film placed at the irradiation point through a ZnSe window by using an infrared radiation thermometer (CPA-T400A, Chino Co.). Under six energies of X-ray irradiation at the storage ring current of 300 mA, the surface temperature of the a-Si thin film varied from 20.5 °C to 107.5 °C. As a result, the error range of the photon flux due to temperature was estimated to be within 2 %.

The photon energy of the monochromatic light of BL07A cannot be determined precisely, because the installed M LM monochromator has low resolving power. Instead, we assessed the relationship of the energies of the undulator harmonics with the gaps of the 3-m undulator at BL07B, which has a grating monochromator with a high resolving power, and we set the energy of the MLM monochromator to the peak positions of the harmonics estimated from this relationship.

3.1. Multi-layered Mirrors and Energy Resolution

Undulator light includes the fundamental and multiple higher harmonics. To eliminate undesired undulator harmonics, undulator light is monochromatized by a combination of an MLM monochromator and three different metal foils prepared as filters. Three different MLMs are used to cover an energy range from 80 to 800 eV. The MLMs are composed of multi-layered mirrors made from Mo and Si, Mo and B_4C, and Ni and C. The filters are made from Ag, Cr, and Ni; the film.

Energy resolution was estimated by measuring the PD current against the photon energy of the MLM monochromator. The electron energy and current of the storage ring were 1.0 GeV and 300 mA, respectively. The third harmonics of the undulator light were used with the undulator gap of 56.2 mm. The Mo/B_4C MLM and Ag filter were used. The resolution, ΔE/E, estimated from this figure is 7.9 %, which is about twice the ideal energy resolution calculated from the specifications of the MLM. The resolution is sufficient for picking out a specific harmonic from other harmonics of the undulator with a certain gap.

3.2. Photon flux

Photon fluxes in 1.0-GeV and 1.5-GeV operation mode were estimated as follows. The photon flux in 1.0-GeV operation mode was calculated from the PD current measured when the ring current was 300 mA. The photon flux in 1.5-GeV operation mode was obtained after the PD current was normalized by the ring current of 300 mA. After normalization, the photon fluxes were obtained for each irradiation condition, with the quantum yield corresponding to the photon energy listed in the data sheet for the AUXV-100.

Figures 2 and 3 show the photon fluxes of monochromatic SR at the reaction chamber of

BL07A measured in 1.0-GeV operation mode and 1.5-GeV operation mode. The colors of the dots indicate the type of MLM used; red dots, green dots, and blue dots respectively indicate measurements made with Mo/Si, Mo/B4C and Ni/C MLMs. Moreover, the shapes of the dots correspond to the harmonics of the undulator; circular, square, triangular, and diamond-shaped dots correspond to the fundamental, third, fifth, and seventh harmonics of the undulator light. An adequate filter corresponding to the energy as listed in Table 1 was used for each measurement. The intensity unit of photon flux was defined as photons/s·cm^2. The error range for the photon flux in these figures was estimated to be 20-30 %.

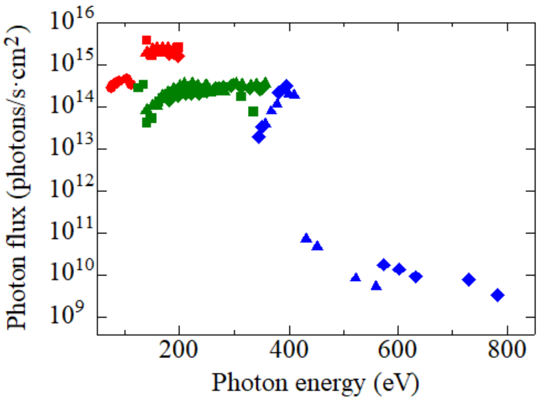

Figure 2 Photon flux at irradiation point of sample stage of BL07A in 1.0-GeV operation mode. Ring current was 300 mA. Red dots, green dots, and blue dots were measured with Mo/Si, Mo/B4C, and Ni/C MLM pairs, respectively. Circular, square, triangular, and diamond-shaped dots represent fundamental, third, fifth and seventh harmonic of undulator light, respectively.

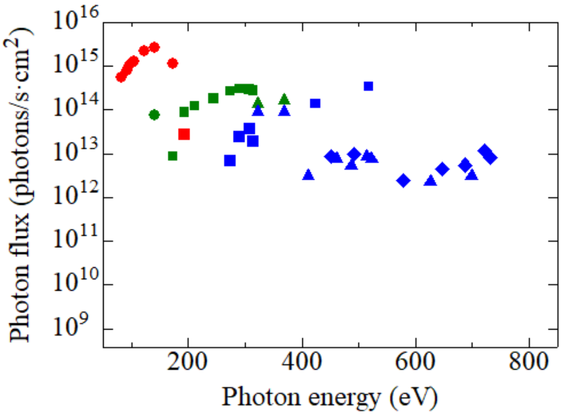

Figure 3 Photon flux at irradiation point of sample stage of BL07A in 1.5-GeV operation mode. Flux was normalized by ring current of 300 mA. Red dots, green dots, and blue dots were measured with Mo/Si, Mo/B4C, and Ni/C MLM pairs, respectively. Circular, square, triangular, and diamond–shaped dots represent fundamental, third, fifth and seventh harmonic of undulator light, respectively.

In the range of 80-200 eV, the photon flux ranged up to more than 2×10^{14} photons/s·cm^2. The highest photon flux in the range of 125—200 eV was about 4×10^{15} photons/s·cm^2. The photon fluxes monochromatized by the Mo/Si MLM were higher than those monochromatized by the Mo/B$_4$C MLM in the range of 125—200 eV. The photon fluxes in the range of 200—400 eV were about 2×10^{14} photons/s·cm^2. The photon fluxes monochromatized by the Mo/B$_4$C MLM were higher than those monochromatized by the Ni/C MLM in the range of 280—360 eV, while they were almost the same value in the range of 360—400 eV. In the range above 400 eV, photon fluxes measured in 1.5-GeV operation mode were about 10^{13} photons/s·cm^2. However, those measured in 1.0-GeV operation mode were lower than 10^{11} photons/s·cm^2. Therefore, the photon-flux-to-sample in 1.5-GeV operation mode was clearly much higher than that in 1.0-GeV operation mode in the energy range higher than 400 eV. The above results indicate that BL07A can be used to investigate the SR process for monochromatic soft X-rays with photon fluxes higher than 10^{13} photons/s·cm^2. In particular, irradiation experiments using high-photon fluxes exceeding 10^{14} photons/s·cm^2 can be performed in the energy range of 80—400 eV.

References

[1] Kanda, K., Haruyama, Y., Fujisawa, M. & Matsui, S. (2001) Nucl. Inst. Meth. A, 467-468, 500-503.

[2] For example, Heya, A., Matsuo, N. & Kanda, K. (2018) Jpn J. Appl. Phys. 57, 116502 1-6.

[3] Heya, A., Kanda, K., Toko, K., Sadoh, T., Amano, S., Matsuo, N., Miyamoto, S., Miyao, M. & Mochizuki, T. (2013) *Thin Solid Films*, **534,** 334-340.

[4] Okui, M., Yato, N., Watanabe, A., Lim, B., Murayama, N., Fukushima & S., Kanda, K. (2016) AIP Conference Proceedings, 1741, 030033.

Photon flux density dependence of graphene synthesis from pentacene-based molecules on Ni film by soft X-ray irradiation

Akira Heya[1], Yoshiki Yamada[1], Kazuhiro Kanda[2], Ryo Yamasaki[3], and Koji Sumitomo[1]

[1] University of Hyogo, [2] LASTI, University of Hyogo, [3] Tocalo Co., Ltd.,

Abstract

Graphene synthesis from pentacene-based molecules on a Ni film/quartz substrate was investigated. A mixture film consisting of pentacene, 6,13-dihydropentacene, and pentacene oligomers, prepared by hot mesh deposition, were irradiated with soft X-rays generated in NewSUBARU. The dependence of photon flux density on graphene synthesis was evaluated to control the size of nanographene and to clarify the polymerization mechanism. It was found that the high photon flux density is required to synthesis the graphene. In addition, the polymerization reaction is considered to be promoted by the photoelectron transfer reaction by soft X-ray excitation and supply of the excited electrons from the Ni underlayer film. In addition, it was suggested that the supply of excited electrons also affects the orientation of graphene.

Introduction

Nanographenes are attractive two-dimensional materials consisting of carbon atoms arranged in a hexagonal lattice. The graphene nanoribbons (GNRs) have band gaps that depend on the ribbon width. Therefore, GNRs are expected to be used in next-generation semiconductor devices as part of logical elements, transistors, spin transistors, and gas sensors.

We have investigated the fabrication method of GNRs using pentacene (Pn), H_2 gas, and W mesh. This method is named as hot mesh deposition (HMD) [1]. By using a nanocarbon film including PO prepared on a Ni film/quartz substrate using a $W_{Ni(3\%)}$ mesh prepared by HMD, graphene was produced by soft X-ray irradiation [2]. It was found that the hydrogen desorption and the catalytic effect of the Ni film excited by soft X-ray irradiation assists in pentacene polymerization. However, to obtain GNRs, the issue of optimization the conditions for PO formation and soft X-ray irradiation remained.

In this study, we tried to optimize the nanocarbon precursor film and soft X-ray irradiation condition.

Experimental

A W mesh (10×55 mm^2) with a wire diameter of 0.1 mm and 30 holes/inch was used. Ni particles were supported on the W mesh surface with an atmospheric plasma spray. A mixture of Ar and H_2 was used as the plasma generation gas. The plasma power was 38.5 kW. The Ni was supported on both faces. The W mesh with supported Ni area ratios of 3% ($W_{Ni(3\%)}$) was prepared.

The HMD apparatus and typical condition are already shown in elsewhere [1]. In this study, to adjust the film property of HMD nanocarbon film, the deposition of nanocarbon film was performed the $W_{Ni(3\%)}$ mesh temperatures (T_{mesh}) were 1410, 1450, and 1480 °C. In this case, the ratio of Pn, DHP, and PO was slightly different [3].

The irradiation of soft X-rays was carried out at BL07A of NewSUBARU. Schematic diagram of soft X-ray irradiation apparatus is shown in Fig. 1. The light source of BL07A was a 2.28 m undulator. The storage-ring energy was 1 GeV during this experiment. The undulator gap was 56.4 mm. The photon energy was 300 eV. The storage-ring current and dose were 300 mA and 100 mA h, respectively. To control the photon flux density, size of slit in storage ring was varied from 0.8 × 0.8 to 8.8 × 8.8 mm^2. The saturated sample temperature during irradiation was 80, 530, and 780 ° C for each slit size. Although the photon flux density was not measured, the ratios of photon flux density were expected from the saturated sample temperature to be 1, 8.5, and 12.7, respectively. To clarify the effect of soft X-ray irradiation, annealed samples were prepared at 3 Pa and 780 ° C for 20 min.

The changes in molecular structure by soft X-ray irradiation was evaluated by Raman spectroscopy and X-ray diffraction (XRD) measurements.

Results and discussion

The Raman spectra of the nanocarbon film prepared by HMD before and after soft X-ray irradiation are shown in Fig. 2. The broad peaks of D and G bands were observed in nanocarbon films prepared at small and medium slit sizes after soft

X-ray irradiation. On the other hand, the sharp peak of D and G bands were observed under condition of large slit size and thermal treatment. It is considered that nanographene was obtained under high photon density and high temperature heat treatment irradiation conditions and amorphous (or contains fine graphite pieces) carbon film was formed under low photon density (small, medium) conditions.

The XRD patterns of the nanocarbon films consisting of Pn, DHP, and PO before and after soft X-ray irradiation are shown in Fig. 3. In the cases of low photon flux densities (small and medium), the diffraction peak was not observed. The X-ray diffraction peak due to graphite (002) was observed in all soft X-ray irradiated sample at 26.5°. However, in thermal treated sample, the X-ray diffraction peak due to graphite (002) was only obtained in the nanocarbon film prepared at a T_{mesh} of 1450 °C. The effect of soft X-ray irradiation on graphene orientation was indicated.

Our aim is GNR synthesis. However, from the Raman spectra and XRD patterns, we obtained not GNR but graphene using soft X-ray irradiation with high photon flux density. To control polymerization, the effects of soft X-ray irradiation on polymerization are discussed. For soft X-ray irradiation, the film property dependence of nanocarbon precursor film was not observed in the range of 1410 and 1480 °C. On the other hand, in thermal treatment, the crystal orientation was depended on nanocarbon precursor film. It implies that the effects of soft X-ray irradiation such as electron excitation and enhancement of molecular movement and photoelectron transfer reaction [4] are useful to obtain high quality GNR.

Conclusions

1) Amorphous (or containing fine graphite pieces) carbon film was produced under low photon density conditions (Small, Medium), and nanographene was produced under high photon density conditions (Large) and high temperature thermal treatment.

2) The structure of the carbon film prepared by soft X-ray irradiation did not depend on the HMD precursor film. On the other hand, the orientation of the nanographene film produced by thermal treatment depended on the HMD precursor film.

3)The polymerization reaction is considered to be promoted by the photoelectron transfer reaction by soft X-ray excitation and the supply of excited electrons from the Ni film, and it was suggested that the supply of excited electrons also affects the orientation of graphene.

References

[1] A. Heya, N. Matsuo, Jpn. J. Appl. Phys. **57** (2018) 04FL03.

[2] A. Heya, T. Oonuki, R. Utimi, K. Kanda, R. Yamasaki, K. Sumitomo, Thin Solid Films **713** (2020) 138365.

[3] A. Heya, R. Yamasaki, N. Matsuo, Thin Solid Films **685** (2019) 186.

[4] A. Shiotari, T. Kumagai, M. Wolf, J. Phys. Chem. C **118** (2014) 11806.

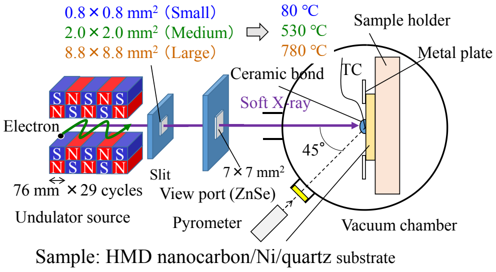

Fig. 1. Schematic diagram of soft X-ray irradiation apparatus.

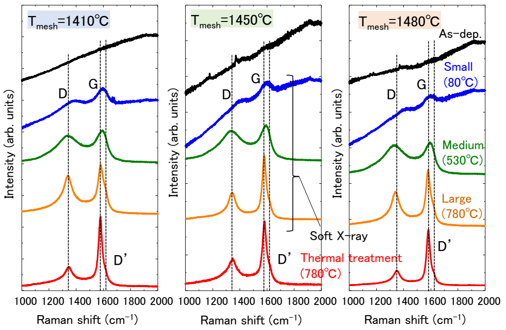

Fig. 2. Raman spectra of nanocarbon films consisting of Pn, DHP, and PO before and after soft X-ray irradiation.

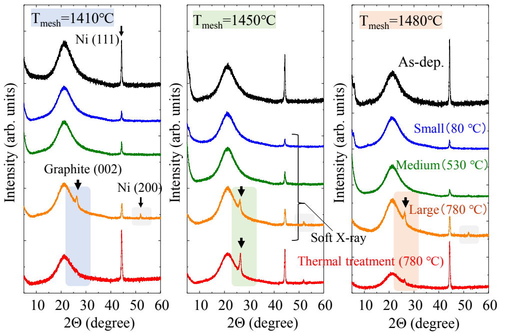

Fig. 3. XRD patterns of nanocarbon films consisting of Pn, DHP, and PO before and after soft X-ray irradiation.

Effect of soft X-ray irradiation on film properties of a hydrogenated Si containing DLC film

Kazuhiro Kanda [1], Ryo Imai [1], Shotaro Tanaka [1], Shuto Suzuki [1], Masahito Niibe [1], Takayuki Hasegawa [1],
Tsuneo Suzuki [2], and Hiroki Akasaka [3]
1 LASTI, University of Hyogo, 3-1-2 Koto, Kamigori, Hyogo, Japan
2 Energy-Density Research Institute, Nagaoka University of Technology, 1603-1 Kamitomioka-machi, Nagaoka, Niigata, Japan
3 School of Engineering, Tokyo Institute of Technology, 2-12-1 Ookayama, Meguro-ku, Tokyo, Japan

Abstract

The effect of soft X-ray irradiation on hydrogenated silicon-containing diamond-like carbon (Si-DLC) films intended for outer-space applications was investigated by using synchrotron radiation (SR). We found that the decrease in film thickness was about 60 nm after 1600-mA·h SR exposure, whereas there was little change in their elemental composition. The decrease in volume was attributable to photoetching caused by SR, unlike desorption of hydrogen in the case of exposure of hydrogenated DLC (H-DLC) film to soft X-rays. The $sp^2/(sp^2+sp^3)$ ratio of the C atoms in the hydrogenated Si-DLC films increased rapidly from ≈0.2 to ≈0.5 for SR doses less than 20 mA·h. SR exposure significantly changed the local structure of carbon atoms near the surface of the hydrogenated Si-DLC film. The rate of volume reduction in the irradiated hydrogenated Si-DLC film was 80 times less than that of the H-DLC film. Doping DLC film with Si thus suppresses the volume reduction caused by exposure to soft X-rays.

1. Introduction

To investigate the effects of the soft X-ray irradiation inside and on the surface of the hydrogenated Si-DLC films and the influence of Si atoms on these effects, we exposed hydrogenated Si-DLC films to SR in the soft X-ray region in a dose region from 0 to 3000 mA·h and discussed on the local structure of carbon and silicon atoms on the basis of the C *K*-edge, Si *K*-edge, and Si *L*-edge near-edge X-ray absorption fine structure (NEXAFS) spectra. In addition, we measured various film properties depending on the SR dose as follows. 1) Film thickness, from which the decrease in film volume can be estimated, was measured with a stylus profiler, SEM and XRR. 2) Film density was estimated by making X-ray reflection-measurements (XRR). 3) Elemental composition of the hydrogenated Si-DLC film was evaluated by a combination of elastic recoil detection analysis (ERDA) and Rutherford backscattering spectrometry (RBS). 4) Surface composition of the hydrogenated Si-DLC film was observed by X-ray photoelectron spectroscopy (XPS).

2. Materials and Methods

Hydrogenated Si-DLC film was deposited on a Si wafer by using an amplitude-modulated radio-frequency plasma-enhanced chemical vapor deposition method (Nippon ITF Co.). The observed thickness of the as-deposited hydrogenated Si-DLC film was 522 nm using a scanning electron microscope (SEM).

The irradiation of the hydrogenated Si-DLC films by soft X-rays was carried out at BL06. The SR at the irradiation point had a continuous spectrum from the infrared to soft X-ray region (less than 1 keV). During the exposure of the hydrogenated Si-DLC films to the soft X-rays, the sample holder was confirmed to be room temperature. In addition, the temperature of the sample holder could be raised to 150 degrees Celsius by using a heater.

To discuss the variations in the local structure of the hydrogenated Si-DLC film due to exposure to SR, the C-*K* edge, Si-*K* edge, and Si-*L* edge NEXAFS spectra were measured. The C *K* edge and Si *L* edge measurements were performed at BL09A, which has grating monochromator. The NEXAFS measurement of the Si *K* absorption was performed at BL05A, which has a double crystal monochromator. In the measurement at both beamlines, the irradiation angle at the sample was the “magic angle” of 54.7° with respect to the surface. The electrons coming from the sample were detected in total electron yield (TEY) mode.

3. Results

The C-*K* edge NEXAFS spectra of the hydrogenated Si-DLC film before and after SR irradiation are depicted in Figure 1 together with that of β-SiC powder and typical commercial DLC film.

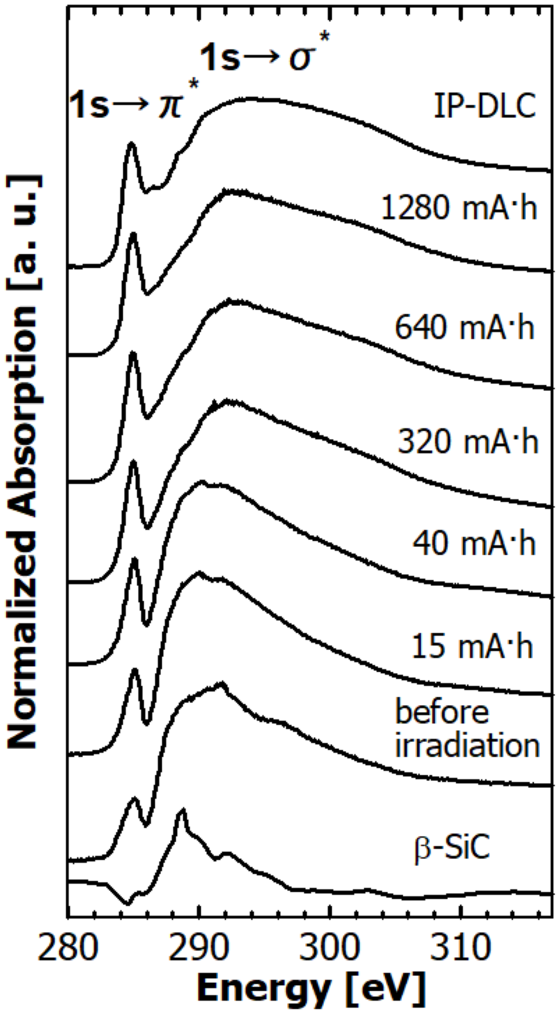

Figure 1. Dependence of C *K*-edge NEXAFS spectra of hydrogenated Si-DLC films on SR dose, together with those of β-SiC powder, and IP-DLC film.

The sharp π* peak observed at 285.4 eV is ascribed to the C $1s \rightarrow \pi^*$ resonance transition originating from the carbon-carbon double bond. The broad σ* peak observed at about 285-310 eV is ascribed to the $C1s \rightarrow \sigma^*$ resonance transition. The C *K*-edge NEXAFS spectra of the Si-DLC films were classified into four types according to silicon content [1]. The C *K*-edge NEXAFS spectra of the hydrogenated Si-DLC films before SR irradiation were classified as type 3. That is, the σ* peak was narrower than that of typical DLC film and shifted to the lower energy of ≈5 eV, due to the influence of the peak at 289 eV derived from the $1s \rightarrow \sigma^*$(C-Si) transition. In addition, the peak intensity of the $1s \rightarrow \pi^*$ transition at 285.4 eV was weak.

The features of the C *K*-edge NEXAFS spectra of hydrogenated Si-DLC film greatly varied between before and after irradiation by soft X-rays. The peak intensity of the $1s \rightarrow \pi^*$ transition at 285.4 eV increased with an SR dose of 15 mA·h and it increased gently with an SR dose more than 15 mA·h. The σ* peak became broader and the intensity peak shifted to a higher energy. In other words, the C *K*-edge NEXAFS spectra of the hydrogenated Si-DLC films changed from type 3 to type 1 or 2. As a result, the spectral features of the hydrogenated Si-DLC film after SR exposure of more than 320 mA·h resembled that of typical DLC film consisting only of carbon and hydrogen without silicon.

The C atoms in the DLC films consist of sp^2 hybridization carbon and sp^3 hybridization carbon. The sp^2/sp^3 ratio have is considered to be a structural parameter that characterizes DLC film properties. The absolute $sp^2/(sp^2+sp^3)$ ratio of carbon atoms in the DLC film can be accurately determined from the C *K*-edge NEXAFS spectra, as described in Ref. 2. The SR-dose dependence of the $sp^2/(sp^2+sp^3)$ ratio in the hydrogenated Si-DLC film is plotted in Figure 2. The amount of sp^2 bonded carbon atoms can be determined by normalizing the area of the resonance corresponding to the $1s \rightarrow \pi^*$ transitions at 285.4 eV with a large section of the spectrum. The absolute $sp^2/(sp^2+sp^3)$ ratio was determined by comparing the normalized $1s \rightarrow \pi^*$ area from the sample with that from the NEXAFS spectrum of highly ordered pyrolytic graphite (HOPG) as a standard sample. The $sp^2/(sp^2+sp^3)$ ratio of the hydrogenated Si-DLC film before irradiation (open circle) was ≈0.23, which indicated that sp^3 hybridized carbon was a major component of the hydrogenated Si-DLC film. The $sp^2/(sp^2+sp^3)$ ratio increased rapidly to ≈0.5 for SR doses less than 20 mA·h. At doses more than 20 mA·h, the $sp^2/(sp^2+sp^3)$ ratio remained approximately constant at ≈0.5.

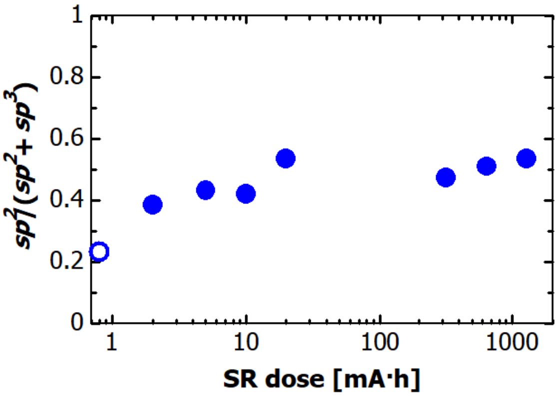

Figure 2. Dependence of sp^2 / (sp^2 + sp^3) ratio in hydrogenated Si-DLC film on SR dose. The open circle indicates sp^2 / (sp^2 + sp^3) ratio of hydrogenated Si-DLC film before SR irradiation.

The Si *K*-edge NEXAFS spectra of the hydrogenated Si-DLC film before after irradiation are depicted in Figure 3 together those of reference materials, SiO_2 powder, Si wafer, β-SiC powder and amorphous hydrogenated silicon (a-Si:H) film. In the spectra of the Si wafer and a-Si:H film, peaks from SiO_2 due to native oxidation were observed at 1846.8 eV. Si atoms in the hydrogenated Si-DLC film can be expected to have Si, C, H, and/or O as neighboring atoms. The chemical environment around the absorbing atom can be evaluated from the positions of the absorption edge and the white line in the NEXAFS spectrum. The Si *K*-edge shifts towards the higher energy side with increasing positive charge on the Si atom. The edge from the hydrogenated Si-DLC film before irradiation was at ≈1840 eV, i.e., near those of the Si wafer and a-Si:H film. The white line was observed about 3 eV above the absorption edge, which resembled those of the Si wafer and a-Si:H film. These results indicate that the chemical environment of Si atoms in the hydrogenated Si-DLC film is similar to that in the Si wafer and a-Si:H film. After SR irradiation, a peak at 1846.8 eV, which was derived from SiO_2, appeared in the NEXAFS spectra of the Si-DLC films. The intensity reached a maximum at 800 mA·h and decreased beyond 1000 mA·h. On the other hand, the intensity increased in the energy range about 1843-1846 eV. The peak in this energy range was reported to be due to deoxidization of SiO_2. These results mean that an oxidized Si layer was generated at the surface of the hydrogenated Si-DLC film by oxidation of surface Si atoms with residual oxygen in the vacuum chamber due to SR irradiation. The oxidized Si layer was deoxidized by additional exposure to soft X-rays. On the other hand, the SR exposure did not change the positions of the absorption edge and the white line. Therefore, the chemical environment around the Si atoms in the hydrogenated Si-DLC film was not changed by the SR irradiation.

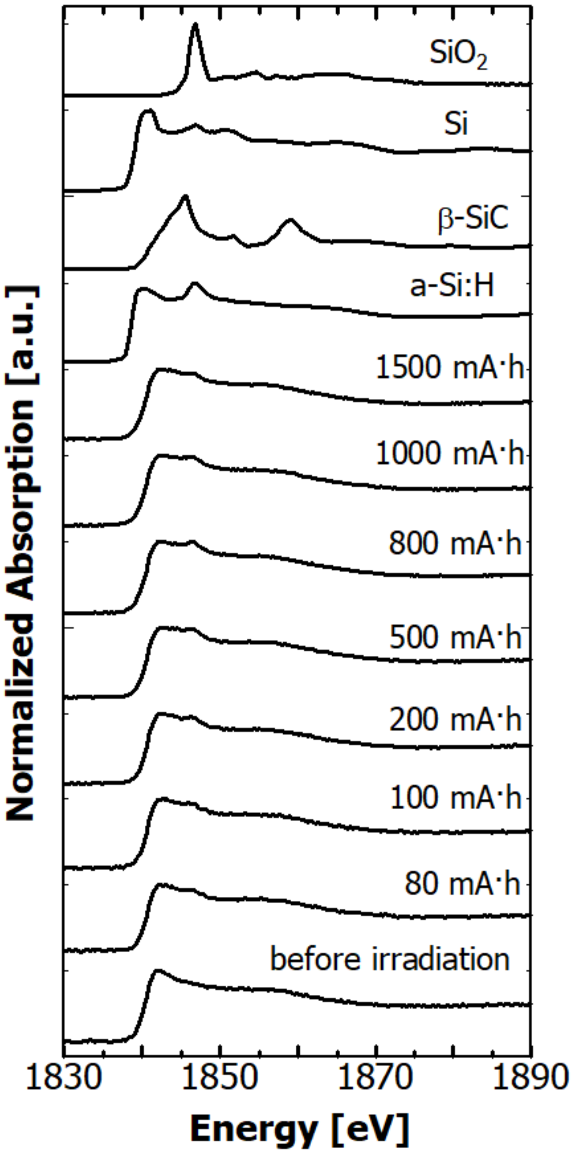

Figure 3. Dependence of Si *K*-edge NEXAFS spectra of hydrogenated Si-DLC films on SR dose, together with those of SiO_2 powder, Si wafer, β-SiC powder and a-Si:H film.

Development of a new γ-beam source by X-ray Compton scattering

Norihito Muramatsu[1], Shinsuke Suzuki[2], Haruo Ohkuma[3], Schin Daté[3], Kazuhiro Kanda[4], Shuji Miyamoto[4],
Tetsuo Harada[4], Takeo Watanabe[4], Hajime Shimizu[1], Manabu Miyabe[1], Atsushi Tokiyasu[1], Masahiro Okabe[1]
[1] ELPH, Tohoku University, [2] JASRI/SPring-8, [3] RCNP, Osaka University, [4] LASTI, University of Hyogo

Abstract

We are developing new techniques to produce a high energy γ-beam via Compton scattering of soft X-rays from 1 or 1.5 GeV electrons at NewSUBARU. The X-rays of 92 eV are obtained from the short undulator at BL07A and reflected backwardly into the storage ring by using a Mo/Si multi-layer mirror. We performed basic tests of the X-ray mirror in terms of surface condition, heat load, and reflection.

Introduction

We aim to develop and demonstrate a new method to produce a high energy γ-beam via Compton scattering of X-rays at an electron storage ring. In our project [1], soft X-rays of 92 eV are obtained from a short undulator (total length: 2.28 m, period length: 7.6 cm) installed to BL07 at NewSUBARU, and backwardly reflected into the storage ring by using a Mo/Si multi-layer mirror. This method increases the maximum energy of a produced γ-beam up to 0.58 and 1.02 GeV for the electron beam energy of 1 and 1.5 GeV, respectively. These maximum energies are much higher than that of laser Compton scattering, which is usually adopted all over the world.

We have set up a large mirror chamber at BL07A [2] to place the Mo/Si multi-layer mirror with automatic stepping-motor stages in a vacuum of 10^{-6} Pa. An initial version of the mirror is put on an oxygen-free copper holder with water cooling. In addition, we have installed an X-ray wire scanner and gamma detectors [3]. The wire scanner measures profiles and intensities of both radiated and reflected X-ray beams, while the gamma detectors are used to get a rate, profile, and energy spectrum of the γ-beam. This report describes results of basic tests for the installed multi-layer mirror in terms of surface condition, heat load, and X-ray reflection.

Examination of surface condition

A substrate of the Mo/Si multi-layer mirror is made of a low thermal expansion glass ceramic (Zerodur) with an area of 50 ×50 mm^2 and a thickness of 5 mm. Its reflective surface is cylindrically polished to make a focus on the electron beam at the 16.7-m upstream straight section of the storage ring. This cylindrical surface was made by bending the substrate with application of stress at two edges, then polishing a surface flatly, and finally releasing the stress [4]. A curvature radius of the cylindrical surface, corresponding to the focal length of 16.7 m, was confirmed by measuring a depth of the mirror center and alternatively counting the number of Newton fringes. The reflective surface was coated by Mo/Si multi-layers with 50 periodic repetitions.

We examined the surface condition of a mirror substrate after polishing. The measurement was done at National Metrology Institute of Japan, which is a research center of AIST. Figure 1(a) shows a result of surface roughness obtained for a region of 2×2 μm^2 by using an atomic force microscope (AFM). The RMS value of surface roughness was measured to be 0.99±0.46 nm without anisotropy. It was confirmed that the surface roughness of our multi-layer mirror is moderately good for the reflection of 92-eV X-rays (λ=13.5 nm). Simultaneously, we measured surface accuracy in the central region of 40 ×40 mm^2 by using an ultrahigh accurate 3D profilometer. As shown in Fig.1(b), a cylindrical surface is clearly formed even by using the unique method mentioned

4. Discussion

The effect of soft X-rays irradiating hydrogenated Si-DLC films was investigated for dose ranges up to 3000 mA·h. The thickness (film volume) of hydrogenated Si-DLC film decreased after the exposure to continuous soft X-rays up to 1000 eV. However, the rate of decrease in film thickness of the hydrogenated Si-DLC film was much smaller than that of the H-DLC film. The density of the hydrogenated Si-DLC film rose a little as a result of the exposure to soft X-rays. The elemental composition (H, C, and Si) of the hydrogenated Si-DLC film, which was estimated from the ERDA/RBS study, did not significantly change as a result of the exposure. In addition, no significant change occurred in the surface elemental composition (C, Si, and O) in the XPS measurement. On the other hand, C *K*-edge NEXAFS measurements showed that soft X-ray exposure significantly changed the local structure of the C atoms, while the Si *K*-edge and Si *L*-edge NEXAFS measurements showed no significant.

From these experimental results, the reason why the rate of decrease in film thickness of hydrogenated Si-DLC film is much smaller than that of H-DLC film is ascribable to the process of the decrease in film thickness. The dominant process in the exposure of H-DLC film to the soft X-rays is shrinkage of the film by desorption of hydrogen from inside the film. These changes in the C-*K* edge NEXAFS spectra are believed to correspond to hydrogen desorption from the film. As described in ref. **3**, hydrogen content in H-DLC films decreases from ≈50 to ≈30% due to 200-mA·h SR exposure. On the other hand, in the exposure of the hydrogenated Si-DLC film to soft X-rays, hydrogen does not desorb from the interior of the film. In this case, the dominant process of the decrease in thickness is photoetching, which is much slower than the shrinkage due to desorption of hydrogen. This photoetching process is not one in which the activation energy determines the reaction rate, because the rate of decrease in film thickness does not change when the substrate temperature rises. In other words, this photoetching does not proceed through a temperature rise in a local area due to exposure to SR, but rather through direct inner shell excitation of the C and Si atoms in the hydrogenated Si-DLC film by the soft X-rays.

Soft X-rays caused reactions several nm from the surface of the hydrogenated Si-DLC film. In the C *K*-edge NEXAFS spectra, the intensity of the $1s \rightarrow \pi^*$ transitions at 285.4 eV increased and the peak of the $1s \rightarrow \sigma^*$ transition shifted with increasing SR dose to the high energy side in the dose range less than 20 mA·h. The shift of the peak of $1s \rightarrow \sigma^*$ transition was ascribable to the decrease in C atoms coupling with Si and H atoms. The $sp^2/(sp^2+sp^3)$ ratio of the C atoms increased from 0.23 to 0.5 the dose range up to 20 mA·h. An increase in the $sp^2/(sp^2+sp^3)$ ratio due to irradiation by soft X-rays was also observed in the irradiated H-DLC film, and this increase was concluded to occur through formation of C-C double bonds induced by the coupling between C atoms through desorption of hydrogen [4].

As described above, it was found that the volume change of the hydrogenated DLC film due to soft X-ray irradiation was suppressed by silicon doping into film. This is attributed to the suppression of hydrogen desorption from the film. We think that the mechanism of the suppression of hydrogen desorption by silicon doping may be as follows: (1) Si atoms on the surface of the hydrogenated Si-DLC film are spontaneously oxidized to silicon oxide, which suppresses hydrogen desorption from inside the film. (2) Soft X-ray irradiation desorbs hydrogen from the film near the surface, increasing the concentration of Si atoms in the surface vicinity, which oxidizes in the same way as (1), and the silicon oxide layer suppresses hydrogen desorption. (3) Soft X-ray irradiation desorbs hydrogen from the film near the surface, forming the C-Si network in the surface vicinity, which suppresses hydrogen desorption.

Reference

1) K. Kanda *et al.*, Jpn. J. Appl. Phys. 2013, 52, 095504.
2) K. Kanda *et al.*, Jpn. J. Appl. Phys. 2002, 41, 4295–4298.
3) K. Kanda *et al.*, Jpn. J. Appl. Phys. 2011, 50, 055801.
4) K. Kanda *et al.*, Sensor Mater. 2017, 29, 817-826.

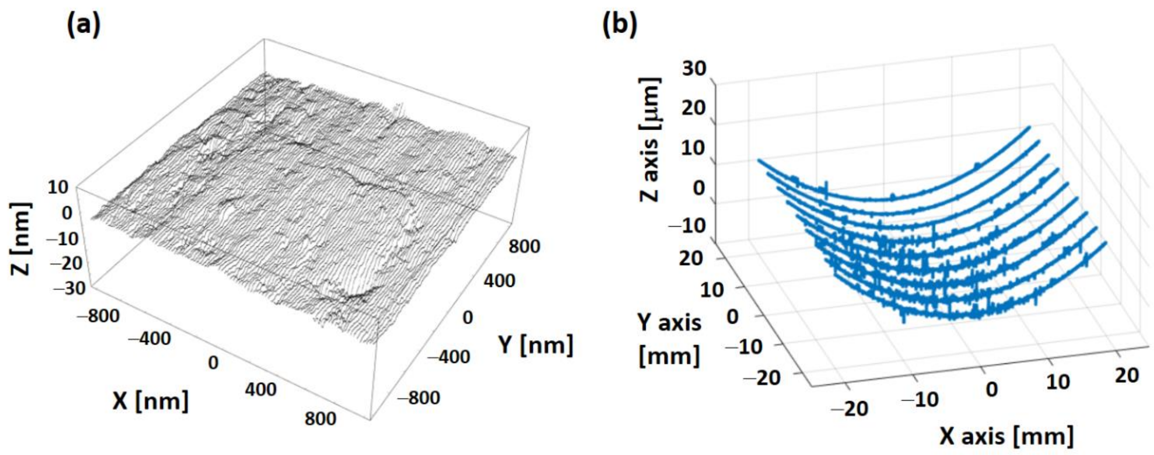

Figure 1 (a) Mirror surface roughness measured by an atomic force microscope in an area of 2×2 μm². (b) Mirror surface accuracy measured by an ultrahigh accurate 3D profilometer in an area of 40 ×40 mm².

above. A mean curvature radius was measured to be 14.38±0.06 m, which was shorter than the design value.

Heat load test with X-ray irradiation

The heat resistant temperature of a Mo/Si multi-layer mirror is known to be 300°C. In addition, high heat load may result in the distortion of a mirror surface, although we adopted a low thermal expansion glass ceramic as a mirror substrate. Therefore, we seriously tested heat load by X-ray irradiation on the multi-layer mirror that was installed at BL07A.

Figure 2 shows a result of temperature change when X-rays are incident on the mirror in a region of 10 ×10 mm² with the undulator setting where a component of 92 eV is peaked as the third harmonics of radiation. The mirror temperature was obtained by using a radiation thermometer thorough a ZnSe window, which was newly attached to the mirror chamber for infrared transmission. In Fig.2, X-rays were irradiated for the first 70 minutes. A temperature of the whole mirror increased by about 100°C in two minutes and reached 190°C at maximum. After stopping the irradiation of X-rays, the mirror temperature gradually dropped over 100 minutes by thermal radiation. We have also confirmed that water cooling of the mirror holder was not effective because of bad heat conductance.

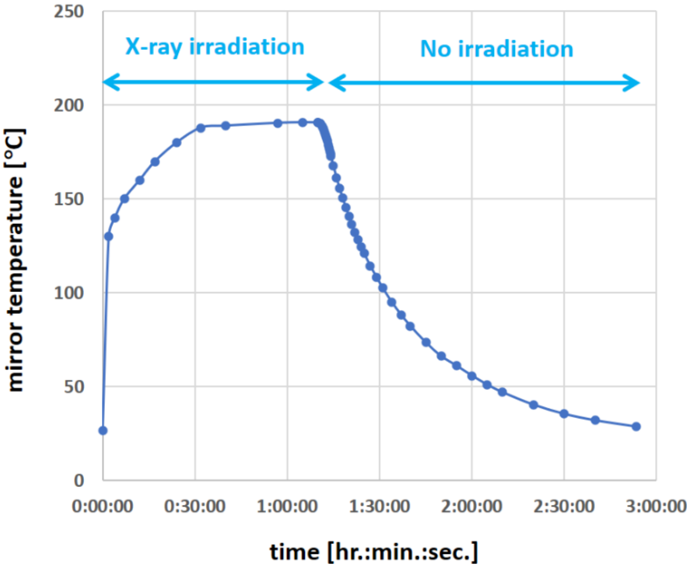

Figure 2 Temperature change of the Mo/Si multi-layer mirror with the irradiation of X-rays in an area of 10 ×10 mm². The irradiation was stopped after 70 minutes.

Expected heat load was estimated to be a few Watt by taking into account higher harmonic radiation that was not reflected. Nevertheless, bad heat contact of the multi-layer mirror in a vacuum causes a rapid increase of its temperature. We confirmed that the maximum temperature was lower than the heat resistant temperature of Mo/Si multi-layer coating.

X-ray reflection test at BL07A

We further tested the performance of the installed Mo/Si multi-layer mirror. As described above, profiles and intensities of radiated and reflected X-rays can be monitored by using the wire scanner where micro current due to a photoelectric effect is detected with wire position shift. Figure 3 shows a result of vertical scanning with a horizontal wire. The profile of reflected X-rays is clearly seen beside a large peak of undulator-radiated X-rays, which contains high harmonic radiation other than a 92 eV component. In this measurement, an elevation angle of the Mo/Si multi-layer mirror was upwardly shifted so that the reflected X-ray profile should not overlap with the incident X-rays. A position of the reflected profile moves depending on the mirror angles, and adjustment of the reflected X-ray axis can be done based on the relation between the profile position and the angle setting.

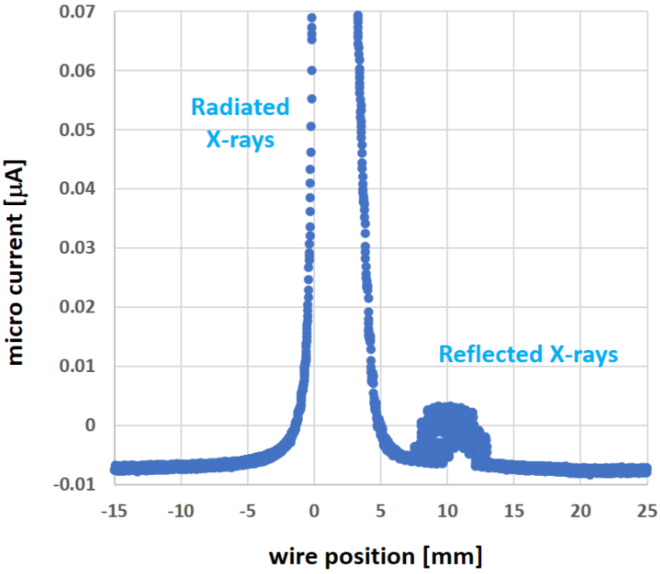

Figure 3 Vertical profiles of radiated and reflected X-rays, obtained by the wire scanner that measures a micro current with the shift of wire position.

Prospect of our project

We are going to demonstrate the production of a high energy γ-beam via Compton scattering of soft X-rays from electrons in the storage ring, for the first time. At an initial stage of production tests, we will use the installed cylindrical mirror whose substrate is made of a low thermal expansion glass ceramic. In addition, we will continue the development of a multi-layer mirror by introducing a silicon substrate and a thermal contact sheet for better heat conductance to the water-cooled mirror holder. We also expect an improvement of surface distortion, caused by heat load. We are simultaneously considering fluid polishing to achieve better surface roughness and accuracy. We aim for the surface roughness of 0.5 nm in RMS. Our development of a new γ-beam source will be helpful for next-generation researches of hadron photoproduction experiments.

Acknowledgments

This research was supported in part by Grant-in-Aid for Challenging Research (Pioneering) No. 18H05325/20K20344.

References

[1]. http://www.rcnp.osaka-u.ac.jp/~mura/kaitaku/

[2]. “Performance of BL07A at NewSUBARU with installation of a new multi-layered-mirror monochromator”, Shotaro Tanaka, Shuto Suzuki, Tomohiro Mishima and Kazuhiro Kanda, J. Synchrotron Rad. 28, 618, 2021.

[3]. “Experimental studies to produce a high energy photon beam by inverse Compton scattering of soft X-rays”, Norihito Muramatsu et al., LASTI Annual Report Vol.21 (2019), 39, 2020.

[4]. “Development of a High Energy Gamma-ray Beam via Inverse Compton Scattering of Soft X-rays”, Norihito Muramatsu et al., J. Particle Accelerator Society of Japan Vol.16 No.3, 154, 2019.

In-situ Evaluation of Surface Cleaning Method with Atomic Hydrogen

Masahito Niibe[1,2], Akira Heya[2] and Seigo Ito[2]
[1]Laboratory of Advanced Science and Technology for Industry, University of Hyogo
[2]Department of Materials and Synchrotron Radiation Engineering, University of Hyogo

Abstract

An atomic hydrogen (AH) irradiation device was introduced at the beamline BL-09A of the NewSUBARU synchrotron radiation facility for the purpose of cleaning the surface of monoatomic layer films and reducing surface oxidation of samples. In order to evaluate its performance, the monatomic layer carbon film and the native metal oxide films were irradiated with AH, and the change in surface state was evaluated with *in-situ* soft X-ray absorption spectroscopy. Hydrocarbon-based contaminants and oxides could be removed to some extent by irradiation with AH. However, even with long-term AH irradiation, the contaminants could not be completely removed. In the future, it will be necessary to study under conditions where the sample temperature is raised and the reaction rate is increased.

Introduction

Since the existence of Dirac fermions in graphene was pointed out by A. Geim and K. Novoselov [1], many studies have been conducted on various Van der Waals two-dimensional (2D) layered materials in terms of both basic physical properties and applications [2]. In the long undulator beamline, BL-09A, of NewSUBARU synchrotron radiation (SR) facility, we have been evaluating those substances of 2D layered materials mainly composed of light elements, such as monoatomic layer h-BN thin film [3], monoatomic layer graphene [4], monoatomic layer boron hydride [5], several-atom layer molybdenum disulfide, and graphene film synthesized from pentacene [6], etc., with X-ray absorption spectroscopy (XAS) and X-ray emission spectroscopy (XES) in the soft X-ray region.

These 2D layered materials may sometimes be synthesized in an ultra-high vacuum and evaluated for their physical properties as they are, without exposing it to the atmosphere. In another case, they may be synthesized and evaluated in different devices. In the latter case, there is a common phenomenon that the surface is oxidized or contaminants are deposited due to atmospheric exposure of the sample or long-term storage in the air. However, since the 2D layered material is a monoatomic layer or a few atomic layers, its physical properties are greatly affected by the contaminations. An Ar ion beam etching or the like has often been used as a method for cleaning contaminants on the surface. But this method causes great damage (crystal structural deformation) to 2D substances, so it is not appropriate to use the ion etching method as in the case of bulk materials.

On the other hand, we have been using atomic hydrogen (AH) generated when hydrogen gas is brought into contact with a high temperature metal (W, etc.) heated to about 1700 °C or higher to remove contaminants deposited on mirrors for SR beamline [7,8]. Since AH is a radical itself, it is chemically active, and the momentum of the particles is small. Therefore, it is expected that the problem of crystal structural deformation can be greatly reduced. In this study, in order to investigate the surface cleaning effect of AH from a more microscopic point of view, the AH generator was directly attached to the SR analysis chamber, and the surface changes before and after AH irradiation were observed *in-situ* using XAS technique.

Experimental Apparatus and Methods

The AH generator is a commercially available device called "H-flux" (tectra, Germany), which heats a W-made capillary with an electron bombardment and passes H_2 gas through the capillary to obtain AH [9]. The overview photograph is shown in **Fig.1**. Since the high temperature AH source is surrounded by a water-cooled Cu plate, heat is less dissipated to the surroundings. The connection to the processing chamber is made with an ICF-70 flange. This device was attached to the BL-09A analysis chamber of the NewSUBARU SR facility at the University of Hyogo to enable AH irradiation of samples and evaluating with *in-situ* soft X-ray absorption spectroscopy. Evaluation samples include HOPG, single-layer and multi-layer graphene stored in the air for a long time, diamond powder, contaminated Au plates, various metal oxide films, and the like.

Fig. 1 Photograph of the atomic hydrogen generation equipment (H-flux).

The generation of AH was confirmed by irradiating the tungsten oxide powder, WO_3, for several minutes. An electron bombardment with 1000 V, 40 mA was applied to the heating mechanism of the H-flex device to heat the tungsten capillary. Although the capillary temperature was not calibrated, but it was estimated to be around 1800 °C under standard operating conditions. Hydrogen gas was flowed inside the capillary at the gas pressure of 0.013 Pa, and the generated atomic hydrogen was irradiated on the WO_3 powder. The results are shown in **Fig. 2**. As can be seen in the figure, the color of the WO_3 powder not irradiated with AH was yellowish green, whereas the powder after AH irradiation changed to black. This is because the metal W is produced by the reduction reaction. In this AH irradiation experiment, the sample temperature is not particularly controlled, and it is considered that the temperature rise due to the radiant heat from the H-flux device is small.

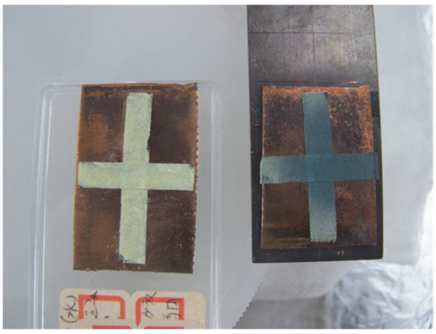

Fig. 2 Confirmation of atomic hydrogen generation by AH irradiation on WO_3 powder. Left: before AH irradiation and right: after AH irradiation.

AH irradiation to samples and results of evaluation with AXS measurement

Figure 3 shows the soft X-ray absorption spectra at the C-K edge before and after AH treatment of single-layer graphene stored in the atmosphere. The spectra show two peaks overlapping at the photon energy of 287.7 eV and 288.5 eV, in addition to the π* peak at 285.4 eV and the broad σ* peak above 292 eV as seen in graphite samples. These are identified as chemical species with a double bond with oxygen, the former being considered to be an oxide with a carbonyl group C=O and the latter being an oxide with a carboxyl group COOH [10]. When the sample is irradiated with AH, the oxide peak decreases and the π* peak increases slightly after 2 min of irradiation. However, even if the irradiation time was further extended to 5 min, the spectral shape did not change much. This is common to other carbon films, and it is thought that physically adsorbed contaminants can be easily removed by AH irradiation, but strongly chemically adsorbed oxides may be difficult to remove. Further optimization of processing conditions is required in the future.

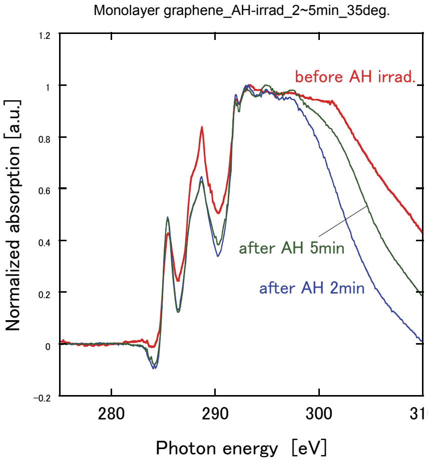

Fig. 3 Soft X-ray absorption spectra of mono-layer graphene at C K-edge before and after AH irradiation.

Figure 4 shows the CK absorption edge spectra before and after AH irradiation of the hydrocarbon contaminants deposited on an Au plate. In this case as well, the peak of 288.8 eV decreased by AH irradiation, but the π* peak of 285.2 eV increased. Moreover, the contaminants containing C could not be completely removed by AH irradiation for 10 min.

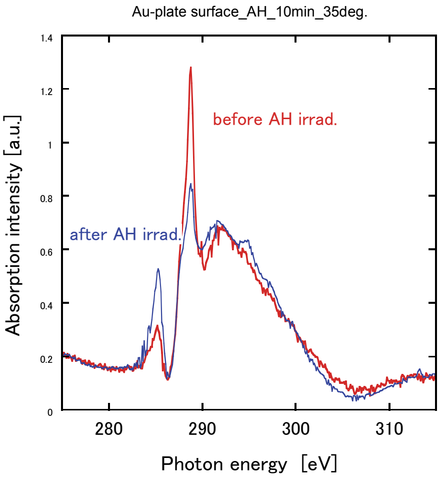

Fig. 4 Soft X-ray absorption spectra of contamination on Au-plate at C K-edge before and after AH irradiation.

Figure 5 shows the absorption spectra of the native oxide films of Al and Ni metals before and after AH irradiation (displayed without normalized). After AH irradiation, the intensity of OK absorption decreased, and it is presumed that oxide reduction occurred. Aluminum is considered to have a strong bond with oxygen, and it was found that the metal oxide can be reduced to some extent even in such a case. It has been reported that the sample temperature is also related to the AH treatment [11]. In the future, we will compare and examine the changes with AH irradiation when the sample temperature is further raised and the reaction rate is increased.

References

[1] K. S. Novoselov et al., Nature, **438**, 197 (2005).

[2] Monatomic Two-Dimensional Layers: Modern Experimental Approaches for Structure, Properties, and Industrial Use, edited by I. Matsuda (Elsevier, 2018).

[3] S. Suzuki, Y. Haruyama, M. Niibe et al., Mater. Res. Express, **6**, 016304 (2019).

[4] M. Niibe, S. Suzuki, S. Honda, The 66th JSAP Spring Meeting 2019, 9p-W521-1.

[5] I. Tateishi, M. Niibe, I. Matsuda et al., Phys. Rev. Materials, **3**, 024004 (2019).

[6] A. Heya, M. Niibe, K. Kanda et al., Jpn. J. Appl. Phys., **60**, 045506 (2021).

[7] M. Niibe et al., AIP Conf. Proc., **2054**, 060010 (2019).

[8] A. Heya et al. J. Photopolymer Sci. Technol. **33**, 419 (2020).

[9] C. Eibl, et al., J. Vac. Sci. Technol. A **16**, 2979 (1998).

[10] R. P. Gandhiraman et al., J. Phys. Chem. C **118**, 18706 (2014).

[11] M. Yamamoto et al., Jpn. J. Appl. Phys. **48**, 026503 (2009).

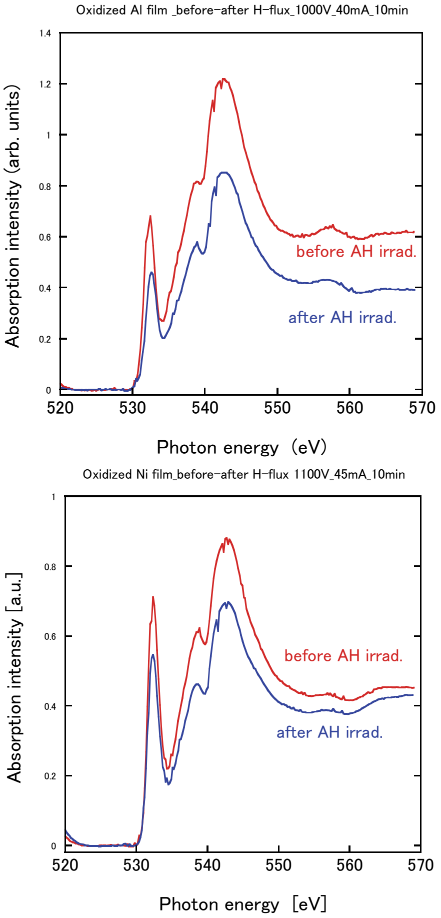

Fig. 5 Soft X-ray absorption spectra of Al (upper) and Ni (lower) native oxide film at O K-edge before and after AH irradiation.

Valence Band Analysis of RuO_x using Soft X-Ray Photoemission Spectroscopy for Oxygen Evolution Reaction at Water Electrolysis

Taku Yoshimura,[1] Ryuki Tsuji,[1] Yuichi Haruyama,[1,2] and Seigo Ito[1*]

[1] Department of Materials and Synchrotron Radiation Engineering, Graduate School of Engineering, University of Hyogo, 2167 Shosha, Himeji, Hyogo 671-2280, Japan.
[2] Laboratory of Advanced Science and Technology for Industry, University of Hyogo, 3-1-2 Kouto, Ako, Hyogo 678-1205, Japan.

Abstract

For research and development of water electrolysis, a famous catalyst (RuO_2) for oxygen evolution reaction in water electrolyzing has been studied using X-ray photoemission spectroscopy (XPES), which revealed the energy diagrams of catalyst surface. It was confirmed that RuO_2 has higher energy potential than the substrate (SUS304).

Introduction

Construction of hydrogen-energy society is quite important for mankind in the future due to global energy and environmental issues. The technology of producing high purity hydrogen by water electrolysis using electric power obtained from natural energy is the most attractive method of converting natural energy into chemical energy, because it does not emit any CO_2. In order to reach a practical energy conversion efficiency, it is necessary to lower the overpotential of the oxygen evolution reaction (OER) at the anodic side using effective catalysts.

In this work, we have prepared RuOx catalysts deposited on stainless steel rod (SUS304) by a coating of the precursor solution and applying flame-annealing, which is a very easy method to fabricate electrocatalysts in a short time. Specially, the performance of water-electrolysis RuOx catalyst deposited on SUS304 by flame-annealing were analyzed and evaluated by electrochemical cyclic voltammetry (CV) and X-ray photoemission spectroscopy (XPES).

Experiments

In this study, a stainless-steel rod (SUS304), which is low cost and useful as a base material for the catalyst deposited electrode, was used as a base material for catalysts for water electrolysis. The stainless-steel electrodes with RuOx catalysts were named RuOx/SUS304. For a catalyst precursor solution of RuOx, ruthenium（Ⅲ）nitrosyl nitrate solution (Ru 1.5 %, Solvent content: water 95.0 %) ($Ru(NO)(NO_3)_3$, Strem Chemicals, Inc.) was used as purchased. The precursor solution was transferred into an elongated test tube to a depth of 4 cm or more, which is to deposit the catalyst on the SUS304 rod over the range of 4 cm. The SUS304 rod were immersed in the catalyst precursor solution and annealed in gas flame. The immersion and annealing were repeated 10 times to be RuOx/SUS304. Figure 1 shows the schematic illustration of the fabrication procedure of RuOx catalysts deposited on a stainless-steel rod by flame-annealing.

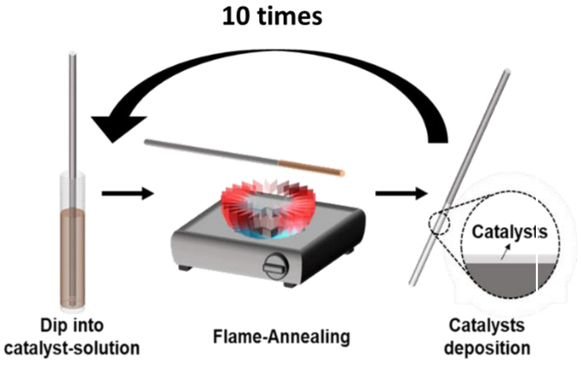

Figure 1. Procedure of flame annealing deposition of RuOx on stainless steel rods.

The electrochemical performance of the RuOx/SUS304 were characterized by electrochemical cyclic voltammetry (CV) in 0.5 M H_2SO_4, 0.5 M K_2SO_4, and 1 M KOH using a reference electrode (reversible hydrogen electrode: RHE).

The energy profile of valence band of RuOx/SUS304 was obtained by a soft X-ray photoemission spectroscopy (XPES) system installed at a beamline 07B end station of NewSUBARU synchrotron radiation facility.

Results and Discussions

Figure 2 shows the current-voltage curves by electrochemical cyclic voltammetry using a SUS304 rod (without RuOx) and RuOx/SUS304. It was confirmed that, by depositing ruthenium oxide (RuOx) on stainless steel (SUS304), the current-onset potential for oxygen evolution decreases in the acidic (0.5 M H_2SO_4) and the neutral (0.5 M K_2SO_4) electrolyte. However, the improvement was obscure using alkaline (1 M KOH) electrolyte. It can be judged that, when the current-onset potential for oxygen evolution is close to the theoretical value (1.23 V) for water electrolysis, the material has effectively active as the oxygen evolution catalyst. From this result, it is considered that ruthenium oxide has good water electrolysis activity on the oxygen evolution side, as is generally known.

(a)

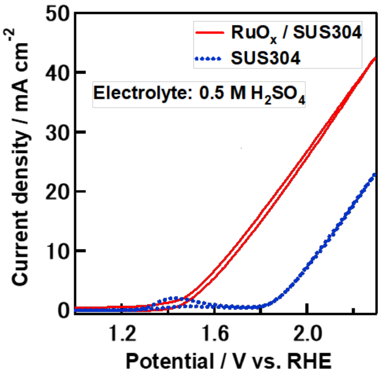

(b)

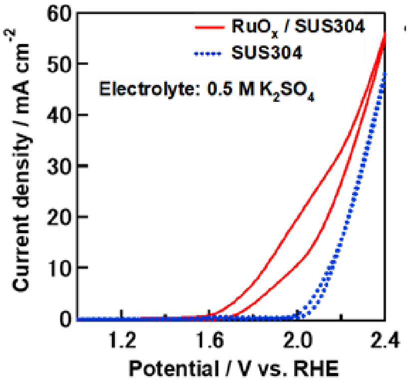

(c)

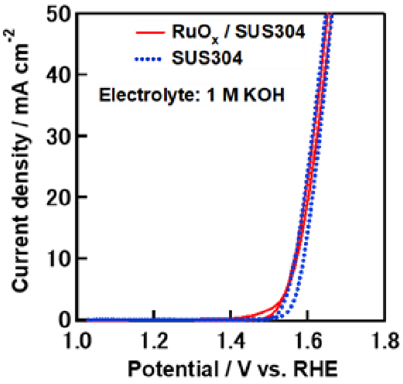

Figure 2. Electrochemical cyclic voltammetry (CV) in 0.5 M H_2SO_4 (a), 0.5 M K_2SO_4 (b), and 1 M KOH (c) using a reference electrode (reversible hydrogen electrode: RHE).

Figure 3 shows XPES results using rods of SUS304 and RuOx/SUS304. In this case, it was confirmed that the onset energy of RuOx has close to zero binding energy against Fermi energy level in material and that the energy level of RuOx was higher than the substrate (SUS304).

In this work, it was confirmed that RuOx/SUS304 has high activity on oxygen evolution reaction for water electrolysis and that the conduction band of RuOx/SUS304 has higher energy than that of SUS304. The relationship between the OER activity and energy level is under discussion for the improvement of catalytic materials.

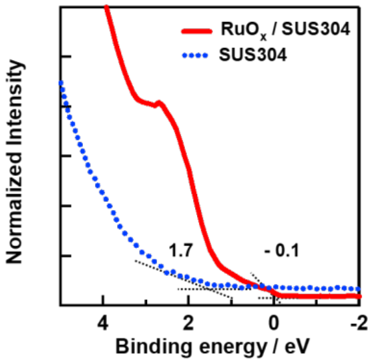

Figure 3. X-ray photoemission spectroscopy (XPES) of SUS304 and RuOx/SUS304.

Sample heating system installed in XAS chamber at BL10

Kae Hiramatsu, Kyoka Maee, Toshiyuki Tanaka, Runa Maruyama, Takuya Motokawa, and Yasuji Muramatsu
Graduate School of Engineering, University of Hyogo

Abstract

To achieve X-ray absorption spectroscopy (XAS) measurements under sample heating conditions, a newly-developed sample heating system was installed in the XAS chamber at BL10. The system can heat a sample plate up to 250 °C. Prior to XAS measurements, off-line heating experiments using sugar samples were performed to clarify the relationship between the heating temperature and vacuum in the XAS chamber. During heating of the sugar samples up to 210 °C, vacuum pressure of the XAS chamber increased to 2×10^{-5} Pa due to degas from melted sugar. Critical vacuum for XAS measurements in BL10 is set to 2×10^{-4} Pa on the interlock system. It is therefore confirmed that *in-situ* or *operand* XAS measurements of heated sugar samples would be safely performed in the XAS chamber at BL10.

1. Introduction

Soft X-ray spectroscopic measurements should be performed under high vacuum pressure, because soft X-rays are intensively absorbed by oxygen and nitrogen in atmosphere. Hence, volatile or outgassing materials are generally prohibited to be directly put in a vacuum chamber for the measurements. However, soft X-ray spectroscopic measurements of them have recently been required for industrial chemical analysis. To perform such the analysis, we have developed the X-ray absorption spectroscopy (XAS) chamber which has a powerful vacuum pumping system, and installed it at BL10 [1, 2].

XAS measurements during sample heating have recently been required. For example, sugar is an interesting material for the XAS measurements. Commercially available sugar consisting of sucrose crystals is generally highly purified material. However, the melting point (mp) of them often differs in 140 - 190 °C range, depending on the sugar manufacturing process. X-ray diffraction (XRD) studies on sugar have not explain the mp-fluctuation. This suggests that the mp-fluctuation does not arise from crystal structure difference. On the other hand, we have recently found the spectral profile differences in X-ray absorption near-edge structure (XANES) spectra of sugar samples [3], which depends on the sugar mp. From the theoretical analysis of C K- and O K-XANES of sugar samples, it is suggested that the spectral profile differences is dependent on hydrogen bonds among sucrose molecules. To confirm the effect of hydrogen bonds for the mp-fluctuation, we have planned to perform *in-situ* XANES measurements of sugar melted by heating in vacuum.

Hydrogen bonds in liquid samples such as water and alcohol have been measured by soft X-ray emission spectroscopy or fluorescence-yield (FY) XAS measurements [4,5]. In these measurements, liquid samples are separated from vacuum by thin SiN windows. On the other hand, our XAS measurements of sugar samples were achieved in solid states by using a total-electron-yield (TEY) method [3]. This suggests that hydrogen bonds in solid would be directly observed by the TEY-XANES. Furthermore, *in-situ* TEY-XAS measurements of solid samples heated to be melt would explore a new XAS technique. We have therefore developed a sample heating system and installed it in the XAS chamber [6] at BL10.

Prior to *in-situ* TEY-XAS measurements under sample heating, we have conducted off-line experiments. The present paper describes the sample heating system and the off-line experiments performed to measure the vacuum pressure evolution during sample heating.

2. Sample heating system

Figure 1 shows the sample heating system. A heating base is a cupper (Cu) block having the electrically heating wires and thermocouple. The heating block is attached behind the sample holder in the XAS chamber. Volume of the XAS chamber is approximately 15 L, and it is pumped by a 350-L/s turbo molecular pump (Leybold, TURBO-VAC 361). The large pumping speed for the chamber volume achieves the high vacuum pressure of 10^{-7} Pa. Heating and monitoring temperature are controlled by a heating controller put outside the chamber. Sample heating up to 250 °C can be performed by the system.

For the sample heating, sample holding should be carefully performed. Conductive carbon tapes and indium (In) substrates, which are used for sample holding in usual TEY-XAS measurements under room temperature, cannot be used in the sample heating measurements. Hence, sample holder should be assembled in all-metal. Figure 2 shows the schematic drawing and photo of the sample plate.

The sample plate is made from Cu. Gold (Au) plate and Au mesh are put on the Cu plate by using screws. Sugar samples are hold between the Au plate and mesh, and then incident X-ray beams irradiate the samples through the Au mesh. Sample current can flow through the Au mesh/plate and Cu plate, and be detected by a galvanometer put outside the XAS chamber. In the present off-line experiments, granulated sugar and *zarame* sugar (mp: 158 - 180 °C) are put on the holder.

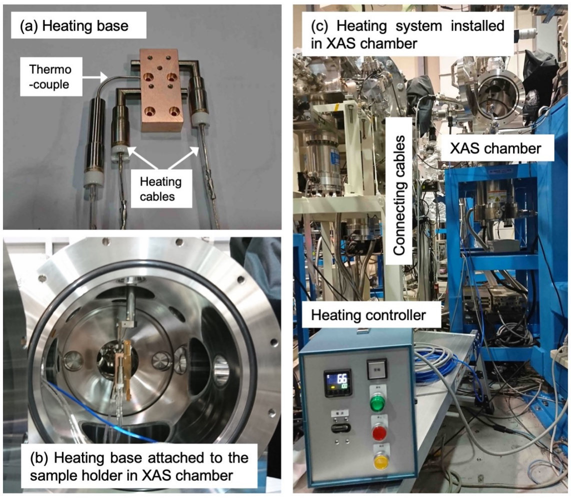

Fig. 1 Photos of a heating base (a), heating base attached to the sample holder in the XAS chamber (b), and a heating system installed in BL10 (c).

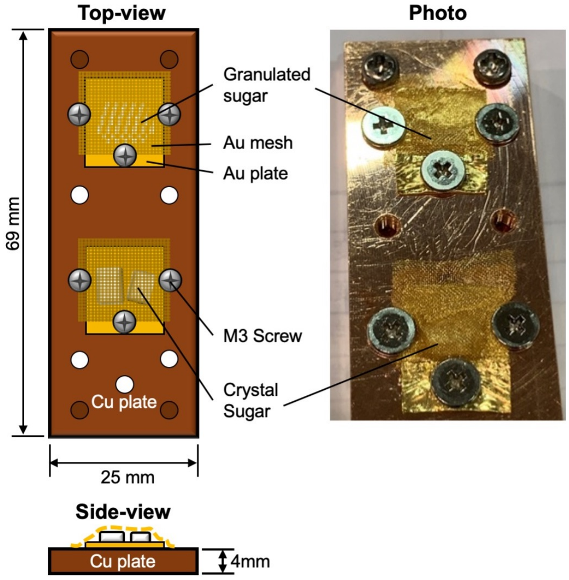

Fig. 2 Schematic drawings of Cu sample plate (left panel) and photo of the plate on which sugar samples are held between the Au plate and mesh (right).

3. Off-line heating experiments

Off-line experiments were proceeded in two steps; 1st step is heating of sample holder without sugar samples for degassing from the Cu sample plate, and 2nd is heating of sample holder with sugar samples held on the degassed Cu plate.

1st step: Back pressure of the XAS chamber was 1.26×10^{-6} Pa. Preset temperature was varied from 40 °C to 200 °C. Vacuum pressures were monitored at individual preset temperature for 500 s. Figure 3(a) shows the evolution of vacuum pressure during heating of the Cu plate in the 40 - 200 °C range. Heating at 40 - 100 °C, vacuum pressure gradually increased up to 2×10^{-5} Pa. Heating at 120 - 200 °C, pressure rapidly increased and peaks can be observed near 100 s heating at individual preset temperature. The vacuum pressure reached to the maximum of 5×10^{-5} Pa at 200 °C heating. Such the behavior means degases of water and/or volatile organic compounds incorporated in Cu plate. After heating at 200 °C for 500 s, vacuum pressure reached to 3×10^{-5} Pa, which is lower than the limit vacuum for XAS measurements. It is therefore confirmed that heating of the Cu plate at 200 °C for 500 s is a sufficient degassing condition.

2nd step: Granulated sugar powders (mp: 158 - 180 °C) and *zarame* sugar particles (mp: 158 - 178 °C) were held on the baked Cu plate, and then heated up to 220 °C. Figure 3(b) shows the evolution of vacuum pressure during the heating.

At the beginning of heating, the temperature was

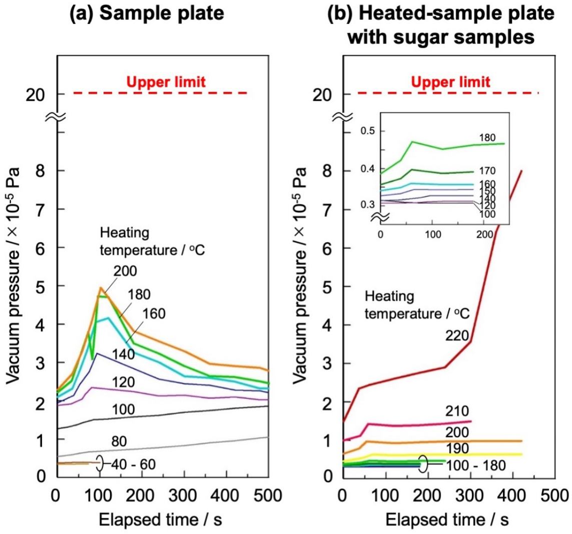

Fig. 3 Left panel (a) shows the vacuum pressure of XAS chamber during heating the sample plate in the 40 - 200 °C range. Right (b) shows the vacuum pressure during heating the heated-sample plate with sugar samples in the 100 - 220 °C range. Inset shows the enlarged graph in the 100 - 180 °C range.

100 ^{o}C and the vacuum pressure was 3.0×10^{-6} Pa. There was little change in pressure during heating from 100 ^{o}C to 150 ^{o}C. This suggests little degassing from Cu plate and sugar samples under 150 ^{o}C heating. Vacuum pressure gradually increased to 5×10^{-6} Pa heating at 160 - 180 ^{o}C, in which sugars may be melting. When the temperature reached to 190 - 210 ^{o}C, the vacuum pressure rapidly increased to 1.5×10^{-5} Pa, because of the sugar melting. Actually, melting of sugar samples can be visually observed at the temperature. Further heating to 220 ^{o}C exhibited a drastic increase of vacuum pressure reaching to 8×10^{-5} Pa. Boiling of melted sugar samples can be visually observed at 220 ^{o}C. Such the melting state and vacuum pressure should be the limit of heating condition in the XAS vacuum chamber. Hence, off-line heating experiments were terminated at 220 ^{o}C.

4. Conclusion

To perform *in-situ* TEY-XAS measurements during sample heating, we have developed a new sample heating system and installed it in the XAS chamber at BL-10. Prior to the XAS measurements, we have performed off-line experiments to clarify the vacuum pressure evolution during sample heating. Followings can be clarified;

(1) Before sample heating, all-metal sample plates should be baked up to 200 ^{o}C for 500 s.

(2) For sugar samples (mp: 140 - 190 ^{o}C), they can be surely melted around 200 ^{o}C with the vacuum pressure of 1.5×10^{-5} Pa. Such heating condition is sufficiently lower than the interlock vacuum limit of 2.0×10^{-4} Pa. Hence, *in-situ* TEY-XAS measurements of sugar sample would be performed under this heating condition.

(3) High temperature heating up to 220 ^{o}C of sugar samples should be prohibited, because sugars are boiled.

Acknowledgements

We would like to express thanks to Professor Kaoru Sakamoto of University of Hyogo for financial support (Grants-in-Aid from the Ministry of Education, Culture, Sports, Science, and Technology of Japan under contract No.17K00823) and preparation of the sugar samples.

References

[1] T. Uemura, Y. Muramatsu, K. Nambu, D. Fukuyama, M. Kuki, T. Harada, T. Watanabe, and H. Kinoshita, Adv. X-Ray Chem. Anal. Japan, 46, 317-325 (2015).

[2] Y. Muramatsu, A. Tsueda, T. Uemura, K. Nambu, T. Ouchi, T. Harada, T. Watanabe, and H. Kinoshita, LASTI Annual Report, 17, 27-28 (2015).

[3] K. Maee and Y. Muramatsu, LASTI Annual Report, 21, 57-59 (2019).

[4] J. Guo and Y. Luo, J. Electron Spectrosc. Relat. Phenom., 177, 181-191 (2010).

[5] T. Tokushima, Y. Harada, Y. Horikawa, O. Takahashi, Y. Senba, H. Ohashi, L.G.M. Pettersson, A. Nilsson, S. Shin, J. Electron Spectrosc. Relat. Phenom., 177, 192-205 (2010).

[6] T. Uemura, Y. Muramatsu, K. Nambu, D. Fukuyama, M. Kuki, T. Harada, T. Watanabe, and H. Kinoshita, Adv. X-Ray Chem. Anal. Japan, 46, 317-325 (2015).

C K-XANES simulations of *n*-alkanes and *cis*-4-alkenes

Runa Maruyama, Toshiyuki Tanaka, and Yasuji Muramatsu
Graduate School of Engineering, University of Hyogo

Abstract

To clarify the fine structures around σ* peak in C K-XANES of carbon materials, C K-XANES spectra of various *n*-alkanes and *cis*-4-alkenes were simulated by the first-principles calculations. For *n*-alkanes, double peak structure can be obtained as σ* peak. The peaks exhibit the lower-energy shifts as the alkyl chain length becomes longer. The peak intensity ratio of the double peaks is also dependent on the alkyl chain length. C K-XANES spectra of *cis*-4-alkenes also show the similar double peak structure which dependent on the alkyl chain length. It is therefore confirmed that C K-XANES spectra of carbon materials containing alkane structures will exhibit broad σ* peak profile composed of double peaks which will exhibit energy-shifts.

1. Introduction

X-ray absorption near-edge structure (XANES) using synchrotron radiation (SR) has been utilized for electronic/chemical-state analysis of carbon materials. Advantages of XANES measurements to characterize carbon materials are briefly summarized as follows. (1) Element/orbital-selective information of the electronic structure can be obtained. (2) High energy-resolution spectroscopy can be performed due to the highly resolved monochromatized SR beams. (3) The orientation of the carbon structure can be evaluated using the polarized SR beams. Additionally, theoretical XANES analysis has recently been performed using first-principles calculations. Hence, a combination of XANES measurements and theoretical analysis provides an advanced characterization method for carbon materials.

Graphitic carbons composed mainly of sp^2-carbon (C) atoms generally exhibit characteristic π* and σ* peaks in C K-XANES. On the other hand, sp^3-C atoms exhibit only σ* peak. From the viewpoint of peak profiles, σ* peaks are generally broader than π* peaks, and σ* peaks overlap continuous conduction band structures. For sp^3-C compounds, although diamond takes rigid crystal structure, alkane molecules take flexible structures because of the numerous conformation caused by rotations around single C-C bonds. This suggests that alkane structure exhibits characteristic σ* peak profile dependent on their conformation and/or alkyl chain length. Hence, the present study aims to clarify the σ* peak structure of alkanes in C K-XANES. Prior to C K-XANES measurements, we have simulated C K-XANES of various *n*-alkanes and *cis*-4-alkenes using the first-principles calculations.

2. XANES Calculation

C K-XANES spectra were theoretically calculated by the DFT calculation code of CASTEP on the Material Studio platform. Calculation models were *n*-alkanes and *cis*-4-alkenes. Details of the models will be explained later. Each model was placed in a sufficiently larger super cell to suppress the intermolecular effects. In the super cell, distance between cell walls and calculation model edge was set longer than 0.5 nm which is sufficiently longer than usual chemical bonds. Hence, such the super cell condition can perform the calculations for isolated models without intermolecular effects. After structure optimization by the Material Studio, DFT calculations in the ground state (initial state) were achieved in CASTEP. Then calculations in an excited state (final state) with a $C1s^{-1}$ core hole were performed for each carbon atom to determine the transition probability, because XANES can mainly reflect the electronic structure in the final state. The transition energy of the calculated XANES was corrected by considering the energy differences at the valence and core levels in the ground (initial) and excited (final) states. The calculated XANES spectra were finally obtained from the transition probability as a function of the transition energy.

Density of state (DOS) was partially calculated using the discrete variational (DV) -Xα method.

3. Results and Discussion

3.1 *n*-Alkanes

Table 1 shows the target *n*-alkanes (C_nH_{2n+2}). Considering C K-XANES measurements under vacuum, models of n = 9 ~ 50 are chosen. Figure 1 shows an example of the calculated C K-XANES and C1s-DOS of *n*-Nonane (C_9H_{20}). In the molecular structure, C atoms are labelled as 1C - 9C, where 1C and 9C are methyl carbons and others are methylene carbons. In the calculated XANES, methyl 1C and 9C exhibit a single peak profile (marked with + in the figure), while methylene 2C - 8C exhibit a double peak profile (marked with *). The peaks also show energy shifts. From the edge (1C, 9C) to center (5C), they exhibit the higher-energy shift as shown by dotted line in the figure. Such energy shift can be explained by the C1s core energy shifts. Figure 1(b) shows the C1s-DOS of 1C - 9C. All C atoms exhibit the single peak profile, showing the lower-energy shift from edge to center carbons. Such the lower-energy shifts on C1s-orbital reflect the higher-energy shifts on the C1s - σ* transitions. Reflecting the energy shifts on XANES of individual 1C - 9C, total XANES which is obtained by summing up the individual XANES of 1C - 9C exhibits a broad double peak profile.

Table 1 Calculated compounds of *n*-alkanes.

Compound	Chemical formula
n-Nonane	C_9H_{20}
n-Decane	$C_{10}H_{22}$
n-Nonadecane	$C_{19}H_{40}$
n-Eicosane	$C_{20}H_{42}$
n-Nonacosane	$C_{29}H_{60}$
n-Triacontane	$C_{30}H_{62}$
n-Pentatriacontane	$C_{35}H_{72}$
n-Tetracontane	$C_{40}H_{82}$
n-Pentacontane	$C_{50}H_{102}$

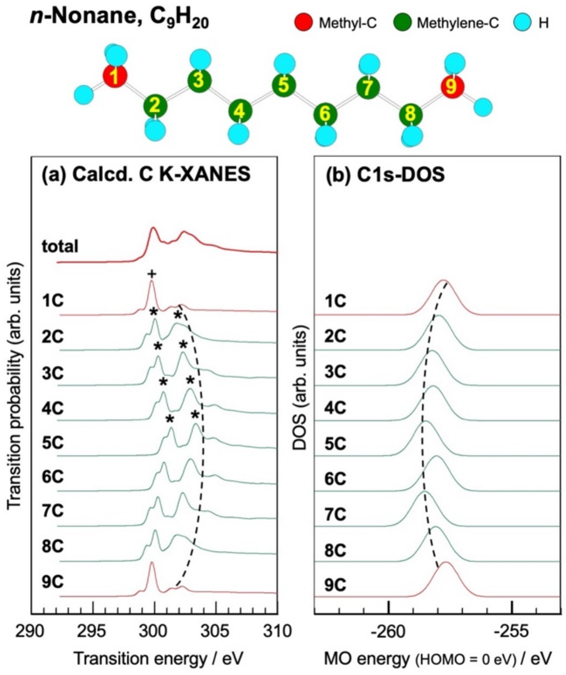

Fig. 1 Calculated C K-XANE (a) and C1s-DOS (b) of *n*-Nonane.

Figure 2 shows the calculated C K-XANES of the *n*-alkanes. All compounds exhibit a double peak profile (denoted by *a* and *b* in the figure). The peaks exhibit the lower-energy shift of 4 eV from C_9H_{20} to $C_{35}H_{72}$, keeping the energy gap of 2.5 eV between peaks *a* and *b*. Peak height of *a* and *b* is also dependent on the alkyl chain length. Relative peak height of *b*/*a* increases as the alkyl chain length becomes longer. Hence, such the alkyl-chain-length-dependence on the peak energy shifts and relative peak height will exhibit a broader σ* profile on C K-XANES of sp^3-C containing carbon materials.

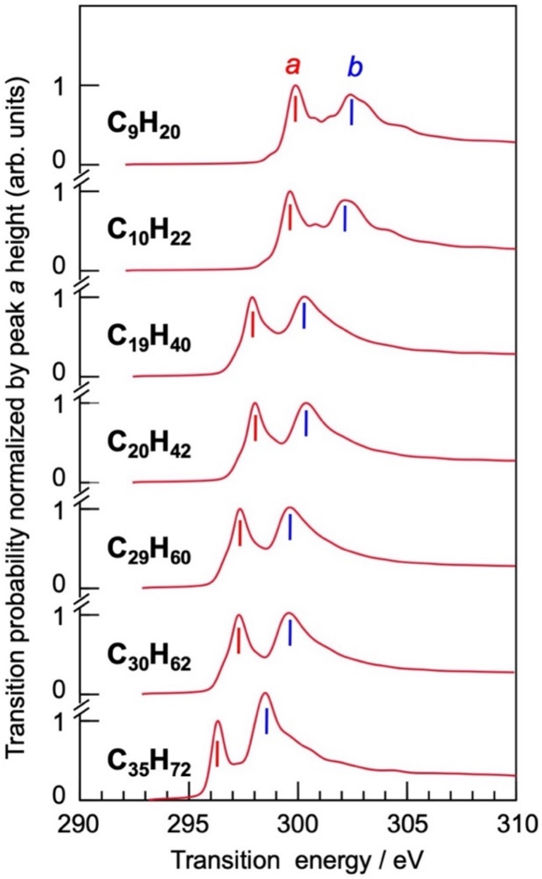

Fig. 2 Calculated C K-XANES of *n*-alkanes.

3.2 *cis*-4-Alkenes

Table 2 shows the target *cis*-4-alkenes (R_1-CH=CH-R_2), in which R_1 is propyl -C_3H_7 and R_2 are alkyl substituents of -C_nH_{2n+1} (n = 3 - 10). Hence, calculated C K-XANES of them will show the R_2 dependence.

Figure 3-1 and 3-2 show the calculated C K-XANES of the *cis*-4-alkenes with their model structures. In the models, C atoms of R_1 are labelled as C1 - C3, and sp^2-C atoms are as C4 and C5. Hence, C1 is a methyl carbon, and C2 and C3 are methylene carbons. For R_2, C atoms are labelled from C6 to C8 (*cis*-4-Octene), to C9 (*cis*-4-Nonene), to C12 (*cis*-4-Dodecene), and to C15 (*cis*-4-Pentadecene).

Table 2 Calculated compounds of *cis*-4-alkenes.

Compound	R_1	R_2
cis-4-Heptene	C_3H_7	C_3H_7
cis-4-Octene	C_3H_7	C_4H_9
cis-4-Decene	C_3H_7	C_7H_{15}
cis-4-Pentadecene	C_3H_7	$C_{10}H_{21}$

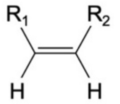

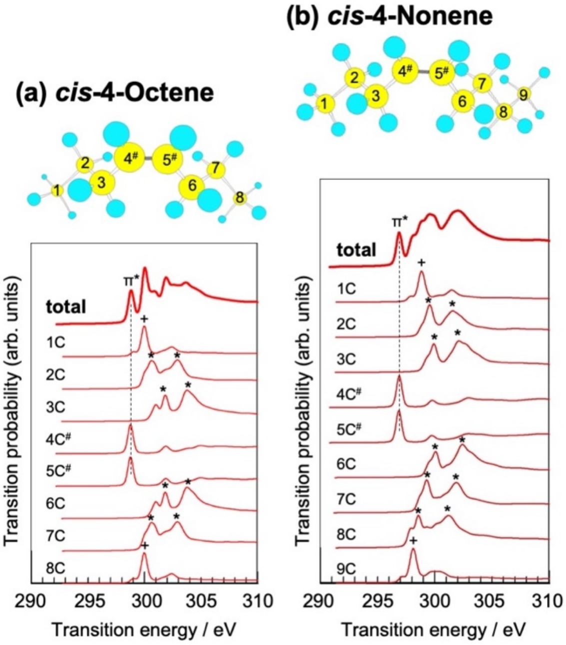

Fig. 3-1 Calculated C K-XANES of *cis*-4-Octene (a) and *cis*-4-Nonene (b).

In the calculated C K-XANES, XANES of individual C atoms and the total XANES summed up them are described. In all models, sp^2-C atoms (C4 and C5) exhibit π* peak at the lowest energy position. The methyl 1C (marked with + in the figure) exhibits a single peak, and methylene 2C and 3C atoms (marked with *) exhibit double peaks. These peaks show the higher-energy shifts from 1C to 3C. Such the peak profiles and energy shifts are as same as the above-mentioned *n*-alkanes. Methylene carbons and terminated methyl carbons in R_2 also show the double peak and single peak profiles, respectively. Energy position of 6C is as same as that of 3C in all compounds, and other C atoms in R_2 show gradual lower-energy shifts from 6C to the terminated methyl carbon. Hence, calculated C K-XANES summed up the total C atoms exhibit broader and complicated structures between the π* - σ* region. It is also found that C K XANES of R_1 and R_2 are isolated by the double bond formed by sp^2-C atoms.

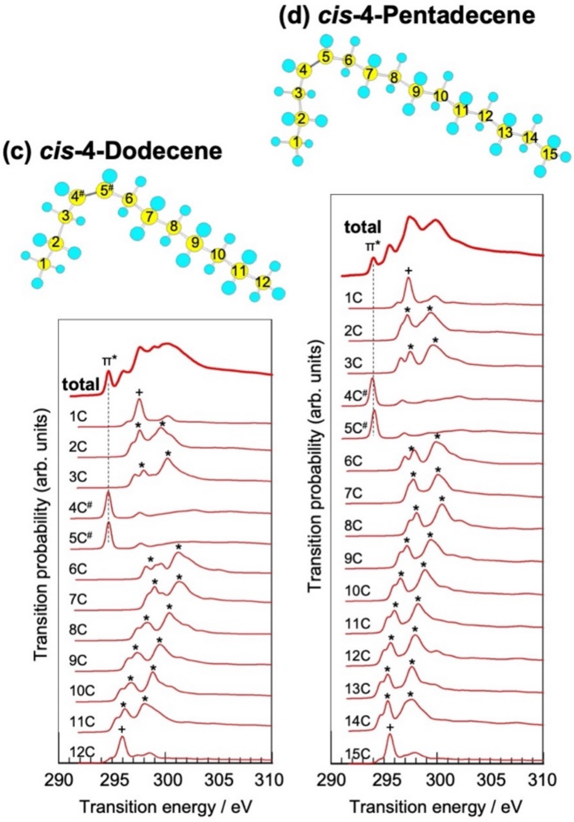

Fig. 3-2 Calculated C K-XANES of *cis*-4-Dodecene (c) and cis-4-Pentadecene (d).

4. Conclusion

To clarify the σ* peak profiles in C K-XANES of alkanes, calculated C K-XANES of various *n*-alkanes and *cis*-4-alkenes were calculated by using the first-principles calculations. The following findings were obtained;

(1) Terminated methyl C atoms exhibit a single peak, while methylene C atoms exhibit a double-peak profile.

(2) Comparing to the terminated methyl C atoms, peaks of methylene C atoms exhibit the gradual higher-energy shifts as the longer alkyl chain length.

(3) Alkyl substituents isolated by double bonds behave independently as alkanes on C K-XANES.

(4) Such the energy shifts dependent on the alkyl chain length will make the broader σ* peak profiles.

Coating Uniformity Effect of EUV Resist for Resonant Soft X-ray Scattering

Tetsuo Harada, Shinji Yamakawa, Takeo Watanabe
LASTI, University of Hyogo

Abstract

Resonant soft X-ray scattering (RSoXS) method is applied to evaluate the chemical contents spatial distribution. Around the carbon absorption edge, the resonant absorption peaks are specific to the chemical contents of carbon. In RSoXS method, the soft X-ray scattering intensity from the resist is recorded by a CCD camera, which the incident photon energy irradiate to the resist sample is varied around the carbon absorption *K*-edge of 284 eV. If these chemical contents have large dispersion, the stochastic becomes worth. In this report, we reported the scattering from samples that were coated with uniform and not-uniform distribution.

Introduction

Resist material has large absorption in the soft X-ray energy region, especially around the carbon K absorption edge. There are resonant absorption peaks which corresponds to chemical structures. For examples, resonant absorption peaks of 286 eV, 289 eV and 296 eV correspond to the π^* bond structure of benzene group, acrylate group, and σ bond structure of carbon, respectively. Therefore, the scattering measurement in soft X-ray region could evaluate the chemical structure distribution. In the resonant soft X-ray scattering (RSoXS) method [1,2], the incident soft X-ray irradiates to the sample, and the scattering light from the sample is recorded by a CCD camera which is installed in a vacuum chamber. The incident photon energy was varied around the carbon absorption edge of 284 eV. The spatial resolution in this method is approximately 12 nm, and this spatial frequency is enough high to analyze the resist uniformity of the chemical structure distribution, which might be affected with the LWR and stochastic.

However, the sample should be coated with good uniformity to analyze the chemical structure distribution. The coating non-uniformity would cause large scattering from the sample, which would hide the scattering from the chemical distribution.

Experiments and Results

Figure 1 shows a schematic drawing the RSoXS system at BL-10 beamline of NewSUBARU. This beamline provides monochromatized energy of the soft X-ray region from 80 to 1000 eV. This beamline has been used for the EUV reflectometry to measure the reflectance of EUV optics and the X-ray absorption spectroscopy (XAS) for the chemical reaction analysis of EUV resist materials. The photon energy range exposing on a sample is from 60 to 1100 eV. The number of photons estimated by the photodiode current at the focal point was 4×10^9 photons/s at the photon energy of 280 eV.

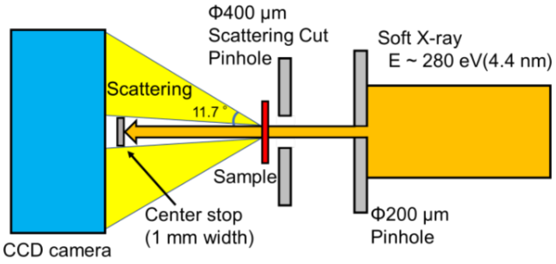

Fig.1 Schematic drawing of RSoXS measurement of the sample resist.

As shown in Fig.1, the incident soft X-ray was irradiated from the right side to the left side, which formulated almost in parallel beam. The focusing point of the incident beam was located at 2.1 m upstream from the sample. A pinhole with 200 μm in diameter employed as an incident aperture to limit the incident beam size to 200 μm. A pinhole with 400 μm in diameter employed as a scattering cut was located just before the sample to cut the direct-back-scattering light from the incident aperture. And then the sample was exposed by the soft X-ray beam and scattered light was led to the in-vacuum CCD camera (MTE-2048B, Roper Scientific) to measure the scattered image from the resist sample.

The center-stop plate with 1 mm in width was located just before the CCD camera, which cut the strong direct beam from the sample

Around the carbon absorption edge, the resonant absorption peaks are specific to the chemical contents. Then, the scattering at the absorption peaks related to the chemical contents in the resist film. Therefore, the resist samples were measure by XAS with the total electron yield (TEY) method around carbon *K* edge. After that, the probe photon energies could be determined as the incident photon energy for the small angle scattering. In the XAS measurement, the resist on a Si wafer was measured.

Figure 2 shows the XAS result of the polymer sample. The vertical axis shows the absorption amount of the polymer. The horizontal axis shows photon energy of the incident soft x-ray beam. The strong absorption peak at 286 eV was observed, which corresponded to the π* bond structure of benzene group. Absorption peak at 289 eV was corresponded to the bonding structure of acrylate group. The broad absorption peaks around 296 eV correspond to σ bond structure of carbon.

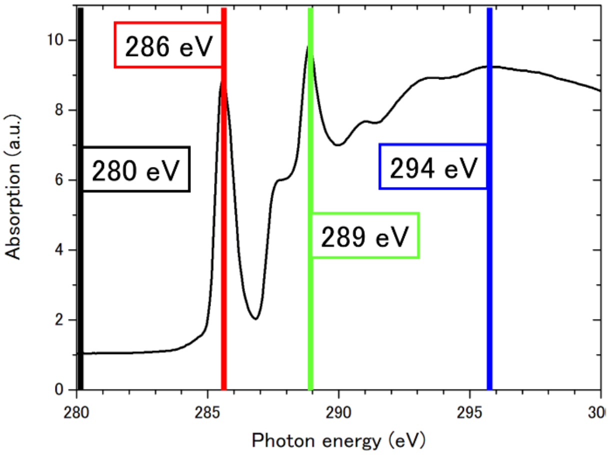

Fig.2 XAS result around CK region of resist which was coated on a Si wafer.

The RSoXS was performed at the photon energies of 280, 286, 289, and 296 eV. The photon energy of 280 eV had just lower than that of the carbon absorption edge. The scattering profile at 280 eV was the base line of the small polymer absorption. Thus, if the spectrum of scattering vector has a similar profile in comparison of that from the base line, the chemical dispersion might be small. Otherwise, if the spectrum of scattering vector has a different profile in comparison of that from the base line, the chemical dispersion might be large.

In sample fabrication process, Si_3N_4 membrane was attached on a Si wafer by polyimide tape. The liquid was dripped on the membrane using a dropper. The polymer was spin coated and prebaked. The spin-coating speed were 500 rpm or 1500 rpm in 30 s. The prebake condition was at the temperature of 130 °C in 60 s. Thickness of the polymer would be approximately 280 nm and 170 nm when the spin-coating speed of 500 rpm and 1500 rpm, respectively.

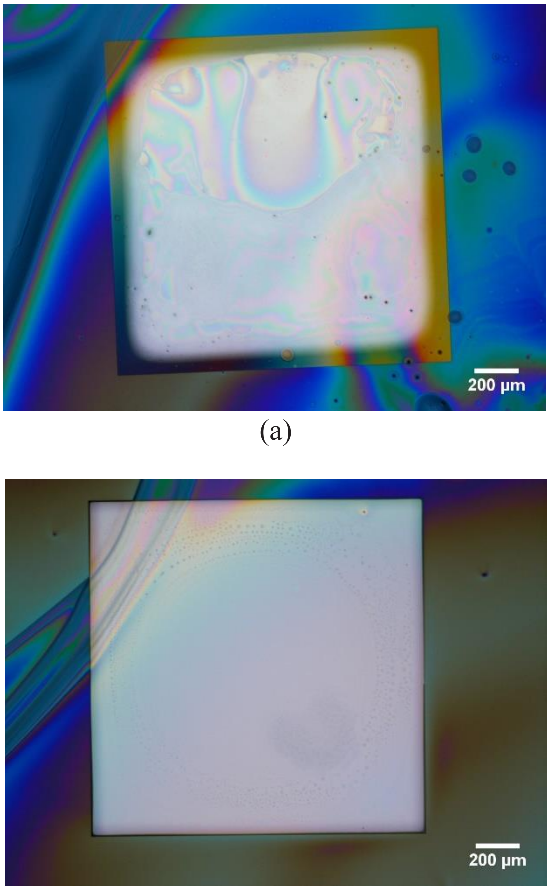

(a)

(b)

Fig. 3. The optical microscope images of the resist coated on the Si_3N_4 membrane at the spin coating speed of (a) 500 rpm and (b) 1500 rpm.

Figures 3(a) and (b) show the optical microscope image of the coated membrane with the spin coating speed of 500 rpm and 1500 rpm, respectively. In Fig. 3(a), the resist film thickness was not uniform. In Fig. 3(b), the resist film thickness was coated with good uniformity.

Figure 4 shows the RSoXS result of the sample with the spin coating speed of (a) 500 rpm and (b) 1500 rpm. Scattering images at 4 photon energies were measured. The horizontal axis shows the scattering vector q. The vertical axis shows scattering signal from the sample, which was normalized at the lowest scattering vector around 0.17 nm^{-1}. For the non-uniform sample, the scattering of each photon energy was quite different with each other in $q > 0.022$ nm^{-1} region which corresponds to the spatial size of 300 nm.

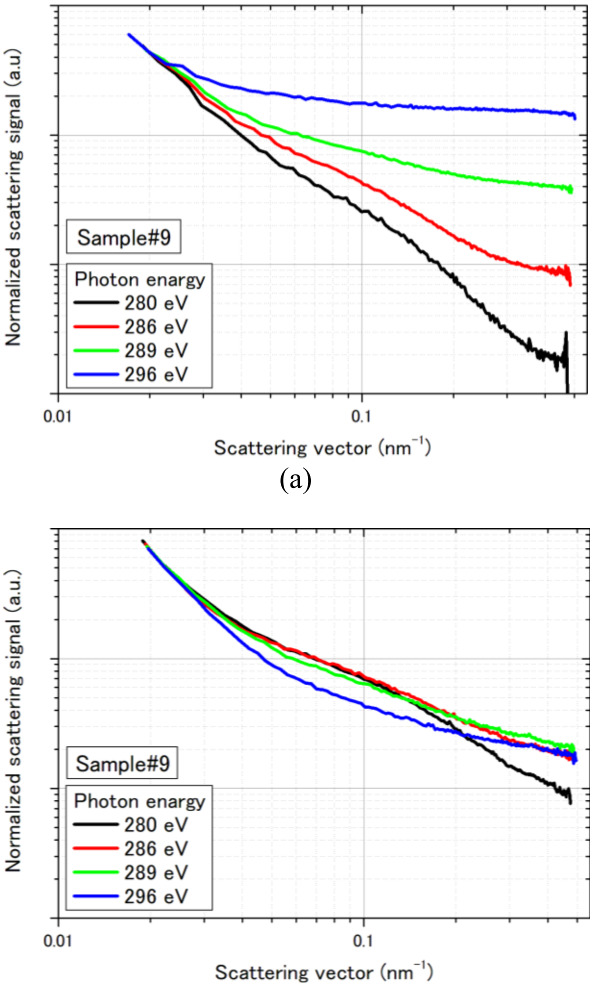

(a)

(b)

Fig. 4. RSoXS result of the sample on the membrane with the spin coating speed of (a) 500 rpm and (b) 1500 rpm.

The polymer would have large cluster of 300 nm. At 280 eV, the polymer had lower absorption because that is just below the carbon absorption peak of 284 eV. The scattering signal of 280 eV was lower than the scatterings of other photon energies at high frequency region. If the cluster has uniform chemical structure, the four scatterings would have same profile. Thus, the cluster would have the chemical structure aggregation, which could be caused by hydrophilicity of functional group in the polymer. The dispersion of these scattering signal shows the cluster size and aggregation of the functional group. For the coating condition at 500 rpm, there was large amount of clusters in in the resist films, which was also observed the optical microscope image as shown in Fig. 4(a).

The coating condition affected the cluster size of the polymer, which was detected to the RSoXS result. The coating on the small membrane was hard to obtain uniform coating. To evaluate chemical structure uniformity of the resist, resist should be coated on the Si wafer, and measured by the RSoXS in the reflection mode. Therefore, we are now developing this reflection-mode RSoXS.

References

1. Y. Nakatani, T. Harada, A. Takano, M. Yamada, and T. Watanabe, J. Photopolym. Sci. Technol., **30** (2017) 77.
2. J. Tanaka, T. Ishiguro, T. Harada, and T. Watanabe, J. Photopolym. Sci. Technol., **32** (2019) 327.

Elimination of Charging Effect in Photoemission Spectroscopy by Gas Introduction

Kento Takenaka[1], Kenta Adachi[1], Koji Takahara[2], Hirosuke Sumida[3], Satoru Suzuki[2]
[1]Graduate School of Science, University of Hyogo, [2]LASTI, University of Hyogo, [3]Mazda Motor Corp.

Abstract

One major problem in photoelectron spectroscopy is the charging effect in measuring bulk insulator samples. We succeeded in eliminating the charging effect of a glass slide and a $LiNbO_3$ by introducing nitrogen gas in the near-ambient-pressure hard X-ray photoemission spectroscopy apparatus. The charging effect was eliminated at 2500 Pa when the distance d between the sample surface and the front-cone of the electron analyzer was 0.3 mm. The elimination of the charging effect is considered to be because secondary electrons created by electron scattering in the gas neutralize the charge on the sample surface. Moreover, the pressure required to eliminate the charging effect was found to strongly depends on d. The charging effect was eliminated at only 250 Pa at d=2.1 mm. Two possible reasons are considered for the strong d dependence. One is pressure decrease near the sample surface induced by the differential pumping through the cone. The other one is the interference of the electron scattering caused by the presence of the corn near the sample surface.

Introduction

Photoelectron Spectroscopy (PES) is a powerful tool for studying the elemental composition, chemical bonding, and electronic structure of materials. However, one of the problems of PES is charging effect in measuring bulk insulator samples. To eliminate charging effect, various methods have been tried [1][2]. The commonly used methods are the simultaneous irradiation of low-energy electrons and ions [3], and the coating of the sample surface with a highly conductive material [4][5]. In the former, it is difficult to control the irradiation conditions. And there is a possibility of sample degradation due to ion irradiation. In the latter case, the coating decreases the photoelectron intensity by scattering. Also, in the measurement with the gas introduced, the coating covers the surface of the sample, making it impossible to observe the reaction between the gas and the sample. Thus, both methods have disadvantages, and it is major challenge to accurately measure bulk insulator samples in photoelectron spectroscopy.

Recently, light sources become more luminous for sensitivity improvement, making it more difficult to control charging effect. It has been reported that measurement under a gas atmosphere reduce the charging effect [6][7][8]. In the previous report, it was shown that the charge relaxation progressed as the gas pressure was increased, but the charge was not completely eliminated even at the maximum pressure in the experiment (~500 Pa). In this study, we attempted to almost completely eliminate the charging effect of an insulator sample by introducing higher pressure gas using the Near-Ambient-Pressure Hard X-ray Photoelectron Spectroscopy (NAP-HAXPES) apparatus.

Experiments

A glass slide (thickness: 1 mm) and a $LiNbO_3$ wafer (0.5 mm) were used as typical insulating samples. The measurements were carried out at near-ambient-pressure hard X-ray photoemission spectroscopy (NAP-HAXPES) station at BL24XU of SPring-8. The excitation light was set at 8 keV using a channel-cut monochromator. The energy analyzer is HiPP-2 from Scienta Omicron. In this system, H_2, N_2 and O_2 gases can be introduced at present. In this experiment, we used N_2 gas, which is relatively stable and has low reactivity, to perform the measurement without chemical change of the sample.

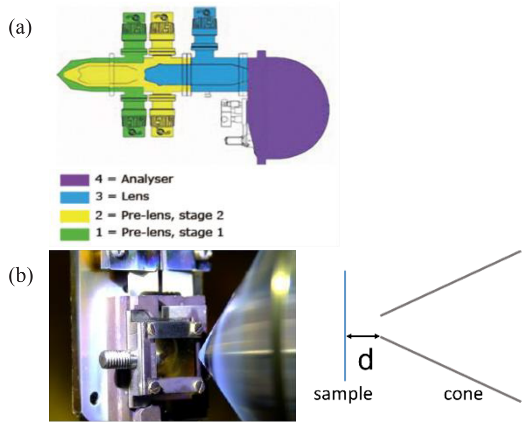

Fig. 1 (a) Schematic diagram of HiPP-2 [9]. (b) Picture of the sample and front cone of the prelens part.

Fig. 1a shows the schematic diagram of HiPP-2. The photoelectrons emitted from the sample enter the hemispherical electron energy analyzer through the prelens, and draw a semicircle to reach the detector. Fig. 1b shows the sample and front cone of the prelens part. There is a small orifice at the tip of the cone through which the photoelectrons enter. If sample-to-cone distance *d* is too short, the gases flow into the electron spectrometer causes pressure decrease on the sample surface [10]. Simulation results report that when *d* is larger than or equal to the hole diameter Φ, the pressure at the sample surface is almost equal to the environmental one [11]. Since $\Phi = 0.3$ mm for this apparatus, we set $d = 0.3$ mm as the normal position and introduced gas to see if the charging would be eliminated. After that, we performed similar measurements with increasing *d*.

Results and discussion

Fig. 2a shows the Nb 3*d* spectra of the $LiNbO_3$ sample obtained under various nitrogen gas pressures, and Fig. 2b shows the pressure dependence of the binding energy and FWHM of the Nb $3d_{5/2}$ peak obtained from Fig. 2a. At nitrogen gas pressures above 2500 Pa, the Nb $3d_{5/2}$ binding energy and FWHM values become mostly constant. The Nb $3d_{5/2}$ binding energy at 2500 Pa is 207.28 eV, which is close to the literature value of 208 eV [12]. From these results, it is considered that the charging effect of the $LiNbO_3$ was eliminated at a nitrogen gas pressure of 2500 Pa.

Fig. 2c shows the Si 1*s* spectra of the glass slide sample obtained under various nitrogen gas pressures, and Fig. 2d shows the pressure dependence of the binding energy and FWHM of the Si 1*s* peak obtained from Fig. 2c. At nitrogen gas pressures above 2500 Pa, the Si 1*s* binding energy and FWHM values become mostly constant. The Si1*s* binding energy at 2500 Pa is 1843.3 eV, which is close to the literature value of 18844.2 eV [13]. From these results, it is considered that the charging effect of the glass slide was eliminated at a nitrogen gas pressure of 2500 Pa.

Fig. 3a shows the change in Nb $3d_{5/2}$ binding energy as the pressure is changed at different distance *d*. At any distance *d*, as the pressure is

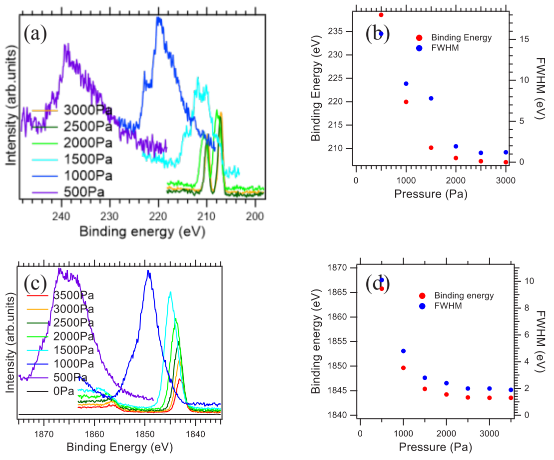

Fig. 2 (a) Nb 3*d* HAXPES of a $LiNbO_3$ plate under various nitrogen pressures. (b) Pressure dependence of the Nb $3d_{5/2}$ binding energies and the FWHM. (c) Si 1*s* HAXPES of a glass plate under various nitrogen pressures. (d) Pressure dependence of the Si 1*s* binding energies and the FWHM.

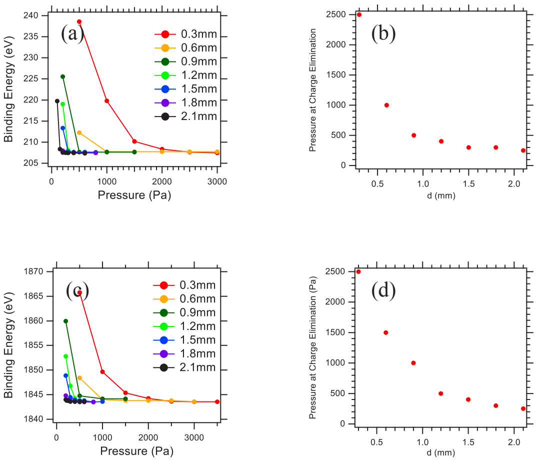

Fig. 3 (a) Pressure dependence of Nb $3d_{5/2}$ binding energy by sample-to-cone distance *d*. (b) Pressure to eliminate Nb 3*d* charge at each distance *d*. (c) Pressure dependence of Si 1*s* binding energy by sample-to-cone distance *d*. (d) Pressure to eliminate Si 1*s* charge at each distance *d*.

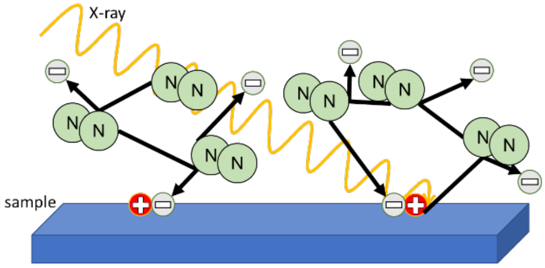

Fig. 4 Schematic diagram of the mechanism of charge elimination.

increased, the binding energy becomes almost the same value, indicating that the charging effect is eliminated. Fig. 3b shows the variation of pressure required for charge elimination of the $LiNbO_3$ sample with distance *d*, based on Fig. 3a. The smaller the distance *d*, the higher the pressure required to eliminate the charging effect.

Fig. 3c shows the change in Si 1*s* binding energy as the pressure is changed at different distance *d*. Fig. 3d shows the variation of pressure required for charge elimination of the glass slide sample with distance *d*, based on Fig. 3c. The results here are similar to those of $LiNbO_3$, but the pressure required to eliminate the charging effect tends to be larger than that of $LiNbO_3$. This indicates that the degree of charging effect varies from sample to sample.

Fig. 4 shows a possible mechanism of charge elimination by gas introduction. First, the photoelectrons emitted from the sample or gas molecules by X-ray irradiation are scattered by the surrounding gas molecules. Then, secondary electrons and Auger electrons are emitted by the scattering, and these electrons are repeatedly scattered. Finally, the electrons that lose energy through scattering reach the positively charged area of the sample by Coulomb attraction, and the charging effect is eliminated. Based on this mechanism, the charge elimination would depend on how much of the electrons are scattered by the gas molecules. The higher the gas pressure, the higher the probability of electrons colliding with gas molecules, and thus the greater the chance of scattering, and the more the process of charge elimination goes on.

There are two possible reasons why the smaller the distance *d*, the higher the pressure required to eliminate the charging effect. The first one is that differential pumping causes a pressure drop on the sample surface. In this case, the smaller the distance *d* is, the larger the pressure drop is, and the larger the deviation from the pressure indicated by the pressure gauge is, the larger "the indicated gas pressure" required to eliminate the charging effect. The other one is that the presence of the corn interferes with the electron scattering. Fig. 5 shows the scattering of 100 electrons with kinetic energy of 8 keV emitted vertically from the sample in nitrogen gas at 2500 Pa by Monte Carlo simulation. According to the simulation, at close distances from the sample, many electrons travel straight ahead with little loss of energy and are expected to enter the cone without being scattered in the actual measurement. The smaller the distance *d* is, the higher the probability that photoelectrons will enter the front cone without being scattered, thus suppressing the emission of secondary and Auger electrons necessary for charge elimination, and thus the gas pressure required to eliminate the charging effect becomes higher.

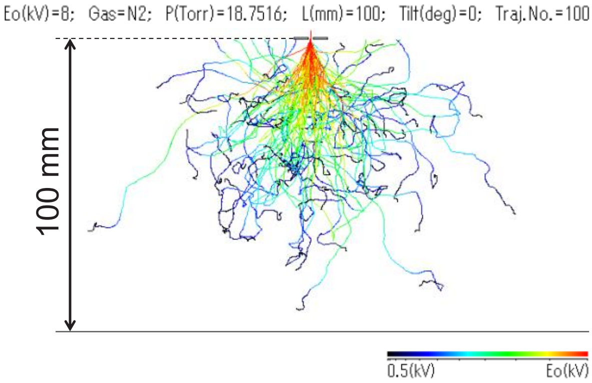

Fig. 5 Monte Carlo simulation of the scattering of 100 electrons of energy 8 keV vertically emitted from a sample in nitrogen gas at 2500 Pa.

Acknowledgments

HAXPES measurements were performed at the beamline BL24XU at SPring-8 (proposal no. 2020A3231 and 2020B3231).

References

[1] H. Iwai, J. Surf. Anal. **7**(1), 37-48 (2000).
[2] T. Oyama *et al.*, Surf. Sci. **20**(8), 530-534 (1999).
[3] L. Edwards, P. Mack, and D. J. Morgan, Surf. Interface Anal. **51**(9), 925–933 (2019).
[4] Y. Mori, J. Surf. Anal. **12**(2), 113–117 (2005).
[5] S. Suzuki *et al.*, J. Appl. Phys. **128**, 015304 (2020).
[6] Enviro^{TM}, https://www.specs-group.com/nc/enviro/products/detail/enviroesca/
[7] X.R. Yu and H. Hantsche, J. Electron Spectrosc. Relat. Phenom. 50,19 (1990).
[8] S. Matsumoto, T. Nanba, Y. Miura, Surf. Sci. **18**(7), 466-472 (1997).
[9] Scienta Omicron,

https://premium.ipros.jp/omicron/catalog/detail/557590/
[10] Y. Takagi, T. Uruga, M. Tada, Y. Iwasawa and T. Yokoyama, Acc. Chem. Res. **51**, 719-727 (2018).
[11] J. Kahk *et al.*, J. Electron Spectrosc. Relat. Phenom. **205**, 57 (2015).
[12] Y. Yun *et al.*, Surf. Sci. **601**, 4636 (2007).
[13] M. Yoshiki, K. Fujii. SPring-8/SACLA Research Report. **8**, 2 (2020).

In-situ Formation of Micro- and Nanobubbles in a Scanning Electron Microscope

Koji Takahara, Satoru Suzuki
LASTI, University of Hyogo

Abstract

The formation of nanobubbles by water radiolysis has been observed by transmission electron microscopy using a very high electron dose ratio. Here, we used a conventional scanning electron microscope to generate nanobubbles in situ at a relatively low magnification of ~1000x. Among the observed bubbles, the one with the lowest dose ratio was 1.3×10^{11} electrons/cm^{2}s, which is 5-7 orders of magnitude smaller than previously reported TEM studies. Furthermore, these bubbles survived for more than three days, contrary to the high Laplace pressure contained within them.

Introduction

Today, micro- and nano-bubbles are being used not only in industrial fields but also in daily necessities such as showers. However, fundamental issues such as the detailed mechanism of stabilization remain unexplored. As an example, nanobubbles do not diffuse and remain in the liquid even though they are covered by a large Laplace pressure.

Several studies have reported that nanobubbles are formed by the radiolysis of water by electron beam irradiation. In these studies, transmission electron microscopy was used to form and observe the nanobubbles. Scanning electron microscopy (SEM) is a similar method of observation using electron irradiation, but there have been no reports of nanobubble formation using SEM, and the first observation using a flow cell has only recently been reported.

In this study, we used SEM to irradiate pure water with electrons and succeeded in generating microbubbles and nanobubbles in-situ [1]. In addition, we used much lower radiation doses than those reported in TEM studies [2].

Experiments

Liquid cells using Si chips with SiN or Si membranes (EMJapan Co., Ltd., Tokyo) as electron-transparent windows were constructed. The thickness and dimensions of the membrane were typically 15 nm and 100 µm × 100 µm, respectively. Electron irradiation of the water and in situ observation were performed at room temperature in a vacuum using a conventional scanning electron microscope (JEOL, JSM-6700F). mainly, beam of accelerating voltage is 5kv.

Result and Discussion

The SEM images of the process of microbubble formation by electron irradiation are shown in Fig 1. In (a), a bubble formed by mistake during sample preparation is observed in the upper right corner. In (b-e), many microbubbles newly appeared and the first observed bubble became larger. After further irradiation (f-m), the size of each bubble increased while the density of the bubbles remained constant. In (n-r), the grown bubbles collided with each other to form large bubbles of ~20 µm. These bubbles were formed by irradiating the cell with a 5 keV electron beam (beam current 26 pA) at a dose ratio of 9.6×10^{11} electrons/cm2s. In our present study, the lowest dose ratio at which bubble formation was observed was 1.3×10^{11} electrons/cm^{2}s, which is 5-7orders of magnitude smaller than previous TEM studies[2][3].

The bubble is observed to be white in this experiment, which means that the bubble is emitting more secondary electrons than the liquid in the cell. Since the density of the gas inside the bubble is much smaller than that of the liquid, it is inferred that these secondary electrons originate from the bubble interface. In the experiment using the liquid flow cell, which is the only example of SEM observation so far, the bubble was observed to be black, but this is probably because the detection method was based on reflected electrons [4].

These tiny bubbles have a very large Laplace pressure due to their small radius of curvature.

However, the lifetime of the bubbles generated in this study reached at least three days. Elucidation of the stabilization mechanism of microbubbles and nanobubbles will be a future challenge.

As a factor in the formation of bubbles, we considered the possibility that boiling was

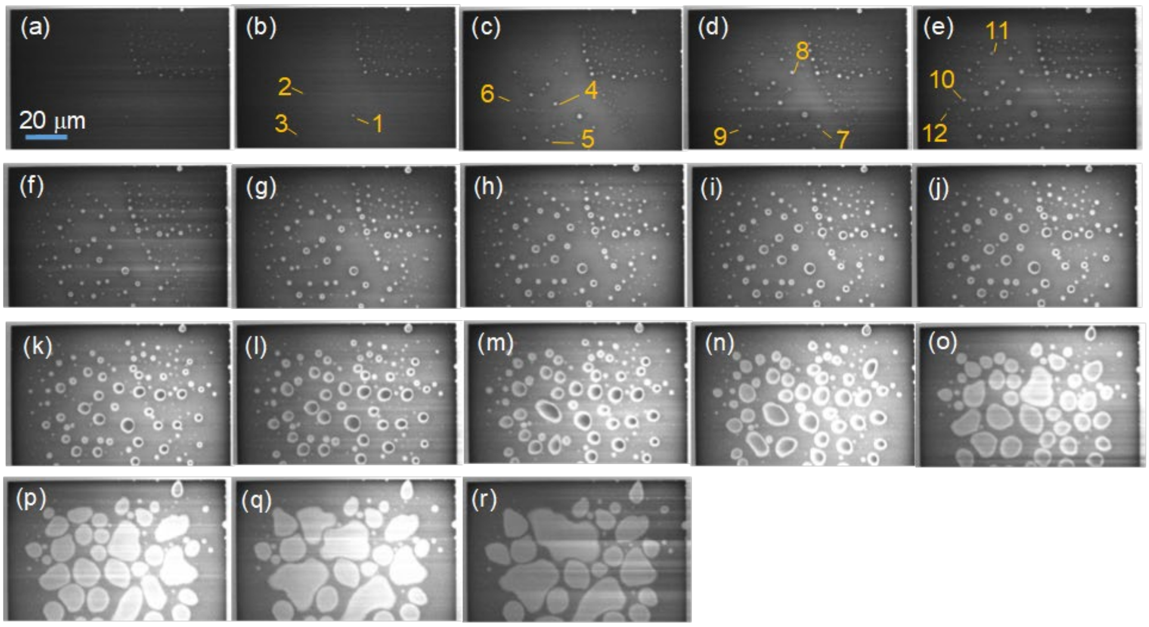

Fig 1. SEM images showing the formation process of large microbubbles by merging of small microbubbles. The electron energy was 5 keV and the irradiation dose ratio was 9.6 × 10^{11} electrons/cm^2·s. (a) Initial state of the liquid cell with a SiN membrane. The microbubbles observed in the upper right of the image were formed during a previous observation. SEM images after irradiation for (b) 44 s, (c) 120 s, (d) 162 s, (e) 204 s, (f) 247 s, (g) 289 s, (h) 329 s, (i) 374 s, (j) 414 s, (k) 491 s, (l) 601 s, (m) 678 s, (n) 789 s, (o) 967 s, (p) 1111 s, (q) 1188 s, and (r) 1367 s. The numbers correspond to those in Fig. 3.

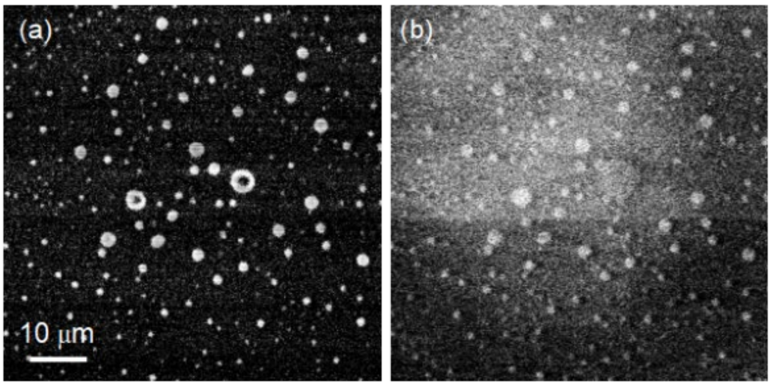

Fig 2. (a) SEM images of micro- and nano-bubbles immediately after formation. (b) SEM images obtained 3 days after bubble formation. The relatively low image quality is due to the effect of charging. Si was used as the film material.

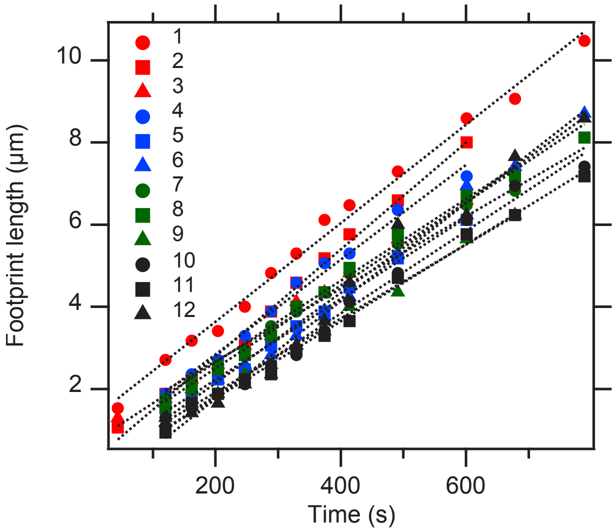

Fig 3. Relationship between footprint lengths and irradiation time of 12 microbubbles observed in Fig. 1. The broken lines are fitting results with linear functions. The numbers correspond to those in Fig. 1.

caused by the temperature rise of water due to electron irradiation. However, the irradiation-induced temperature was estimated by referring to the previous report [5] and the value for boiling was negligibly small (~1 mK). Therefore, the bubble formation is considered to be caused by the radiolysis of water.

Fig 3 shows the time dependence of the footprint length (before coalescence) of the 12 microbubbles observed in Fig 2. The footprint lengths increase almost linearly with irradiation time, indicating that the growth rate is almost constant regardless of the change in size. the close slope of the 12 bubbles means that the growth rate of all bubbles is close. Assuming that the three-dimensional shape of the bubbles is invariant, the linear dependence means that the bubble volume (V) increases rapidly with increasing irradiation time t, i.e., $V \propto t^3$. $dV/dt \propto t^2 \propto S$ (surface area), we tentatively propose the following bubble growth model. Uniform electron beam irradiation produces gas species uniformly in the liquid cell. When bubbles are formed by the agglomeration of gas species, they grow by taking in gas species (or invisible nanobubbles) uniformly dispersed near the surface from the surface.

The reason for the formation of bubbles at much lower dose ratios in the present experiment than in previous TEM studies is thought to be the difference in the permeability of the sample to electrons: in TEM observations, the thickness of the liquid cell is usually chosen to be close to the inelastic mean free path (188 nm at 200 keV for water). The thickness of the liquid cell was chosen to be close to the inelastic mean free path (188 nm at 200 keV for water [6]). Therefore, the liquid cell is very transparent to incident electrons. On the other hand, in the present SEM, the thickness of the cell (100-200 μm) is much larger than the maximum transmission depth (~8 μm at 20 keV and ~0.8 μm at 5 keV [5]), so the incident electrons can transfer almost all of their energy to the confined water. In addition, the supersaturation required for the formation and stabilization of bubbles was considered to have been achieved in this experiment. The small volume of the liquid cell (1-2 nl) and the low pressure in the cell (the maximum pressure that the membrane can withstand is 2 atm) contributed to the supersaturation state.

Conclusion

The formation of surface micro- and nano-bubbles by electron irradiation was observed using a conventional scanning electron microscope with a liquid cell confined with pure water. Bubbles were formed at an irradiation dose ratio 5~7 orders of magnitude lower than previous TEM studies. The results show that micro- and nano-bubbles can be formed in SEM and observed stably for a long time, suggesting that SEM may become an important analytical tool in the study of micro- and nano-bubbles.

References

[1] K.Takahara and S.Suzuki, J. Appl. Phys. (accepted).
[2] J. M. Grogan et al., Nano Letters 14, 359 (2014).
[3] Q.Kim et al, Applied Nanoscience (2018).
[4] T. Ishida, Electronics and Communications in Japan 102 (9), 55-60 (2019).
[5] H. Takahashi, J. Surf. Sci. Soc. Jpn 25 (4), 224-231 (2004).
[6] Q. Kim, D. Shin, J. Park, D. A. Weitz and W. Jhe, Applied Nanoscience (2018).

Cross-sectional Observation of Micro- and Nanobubbles Formed In-situ in a Scanning Electron Microscope

Koji Takahara, Satoru Suzuki
LASTI, University of Hyogo

Abstract

Cross-sectional observation of micro- and nano-bubbles formed by water radiolysis was successfully carried out, and the average value of contact angle of 69 bubbles was 69°. The average value of the contact angle of 69 bubbles was 69°. In previous AFM studies, microbubbles were observed in a flat shape, and the present results are contrary to these studies. In addition, the lifetime of the bubbles reached more than three days even though they contained a large Laplace pressure from these large contact angles.

Introduction

In recent years, microbubbles and nanobubbles have been utilized in a variety of fields ranging from industrial fields such as agriculture and fisheries to daily necessities such as washing machines. However, it is difficult to analyze these microbubbles individually, and their basic physical properties, such as stabilization mechanisms, remain unresolved. Several studies measuring the shape of surface microbubbles and nanobubbles have been reported using AFM at present. However, the present study using scanning electron microscopy (SEM) showed different results from the previous studies. In this study, we directly observed the cross-section of surface bubbles formed by SEM radiolysis [1].

This study is also a companion to "In-situ Formation of Micro- and Nanobubbles in a Scanning Electron Microscope" presented in this annual report.

Experiments

Liquid cells using Si chips with SiN or Si membranes (EMJapan Co., Ltd., Tokyo) as electron-transparent windows were constructed. The thickness and dimensions of the membrane were typically 15 nm and 100 μm × 100 μm, respectively. Electron irradiation of the water and in situ observation were performed at room temperature in a vacuum using a conventional scanning electron microscope (JEOL, JSM-6700F). mainly, beam of accelerating voltage is 5kv.

Result and Discussion

Fig. 1. is a cross-sectional SEM image of the micro- and nanobubbles formed by electron irradiation at the edge of the electron transmission window. These bubbles touched both the SiN film and the Si wall, as shown schematically in Fig. 2. In Fig. 2 (top), the top cross-sectional view of the SEM observed bubbles is shown. Fig 2. (bottom) shows the side cross section which cannot be observed by SEM. Edge bubbles, such as the one observed at the edge of the window in this study, are assumed to be part of a sphere with a radius of curvature R. To identify the contact angle of the bubble, we measured the wettability of the SiN film and that of the Si wall. Since the wettability of each was very close, we assumed that the contact angles of the SiN film and the Si wall were the same. From these considerations, the radius of curvature R is determined as a simple surface bubble by the following equation

$$R = L/(2\ \sin\theta\ ) \qquad (1)$$

From the SEM image of the cross-section, the contact angle θ′ and footprint length L′ can be measured. As shown in Figure 2, θ ′, L′, and R′ are slightly different from θ, L, and R can be determined from geometric considerations by the following equation.

$$R = R'\sqrt{1+\cos^2\theta'} \qquad (2)$$

$$L = 2R' = L'/\sin\theta' \qquad (3)$$

$$\theta = \cos^{-1}(\cos\theta'/\sqrt{1+\cos^2\theta'}) \qquad (4)$$

The real radius of curvature R, which is related

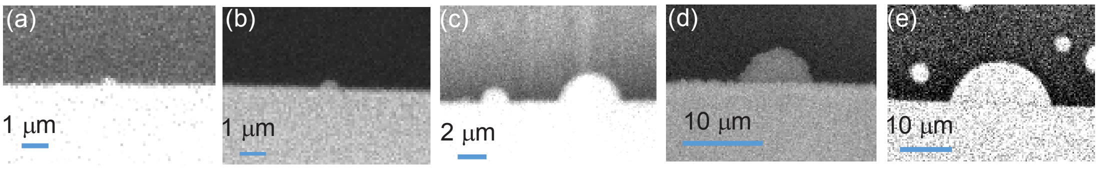

Fig 1. (a)-(e) Cross-sectional SEM images of nano- and microbubbles of various sizes.

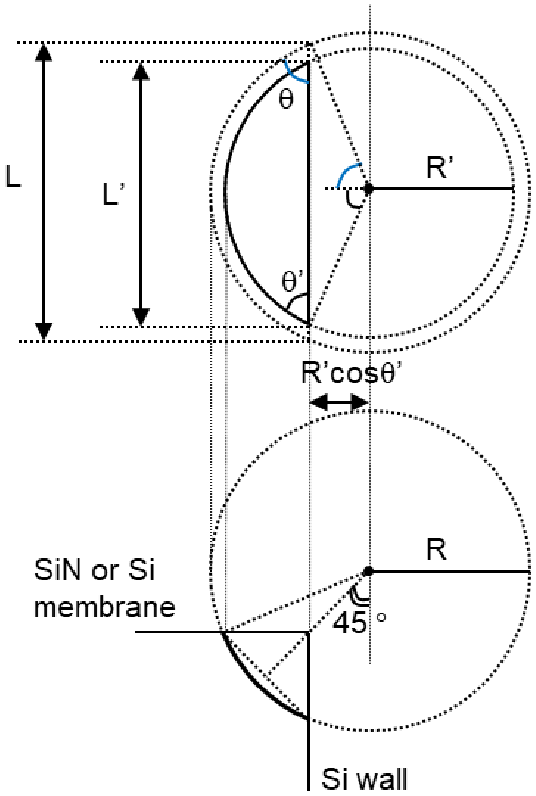

Fig 2. Schematic of a bubble formed at an edge and definition of *L*, *L′*, *θ*, *θ′*, *R*, and *R′*. Side view (bottom) and top view (top).

to the Laplace pressure and other physical properties of the edge bubble, is determined by L and L′, but they differ little when θ′ is relatively large. Since the difference between R and R′ is small and L′ and θ′ could be measured directly, L′ and θ′ are used for the bubble formed at the edge in the following discussion. This does not qualitatively affect the discussion.

An important result from Fig. 1 is that the shape of the bubble is close to a hemisphere, regardless of its size. This is in contrast to previous AFM studies, where the bubbles were referred to as micropancakes due to their shape [2][3]. TEM studies have also shown hemispherical surface bubbles similar to our results [4]. The simple average of *θ′* for the 69 edge bubbles we observed in this study was 69. Fig 3 shows the smallest bubble that we were able to observe in this study.If we apply the previously shown *θ′* to the smallest bubble as shown in Fig 3 (L′ =100 nm), we were able to calculate the Laplace pressure to be about 25 atm.

Furthermore, it is worth noting here that the bubble with such a high Laplace pressure continued to exist for more than three days.

Conclusion

Direct cross-sectional observation of bubbles

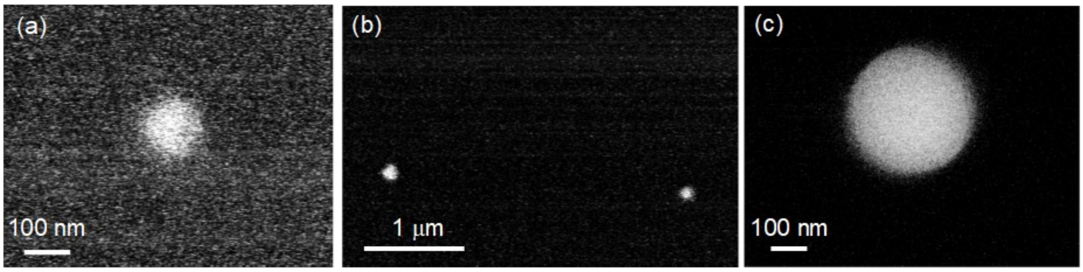

Fig3. (a)–(c) SEM images of nanobubbles. During formation and observation of the nanobubbles, the irradiation dose ratio was 1–15 × 10^{15} electrons/cm^2·s and the electron kinetic energy was 5 keV. The membrane material was SiN.

formed in situ by electron beam irradiation. The shape of the bubble was similar to a hemisphere regardless of its size. This result is contrary to the results of the AFM study, but is very close to the TEM study. The bubbles also had high Laplace pressure due to this shape, but their lifetime reached at least three days.

References

[1] K.Takahara and S.Suzuki, J. Appl. Phys. (accepted).
[2] J. R. T. Seddon and D. Lohse, Journal of Physics: Condensed Matter **23** (13), 133001 (2011).
[3] T. Nishiyama, Y. Yamada, T. Ikuta, K. Takahashi and Y. Takata, Langmuir **31** (3), 982-986 (2015).
[4] D. Shin, J. B. Park, Y.-J. Kim, S. J. Kim, J. H. Kang, B. Lee, S.-P. Cho, B. H. Hong and K. S. Novoselov, Nature Communications **6** (1), 6068 (2015).

Irradiation Effect of Atomic Hydrogen on Si Surface

D. Morimoto[1], A. Heya[2], K. Sumitomo[2], S. Ito[2], S. Suzuki[1], and Y. Haruyama[1]
[1]Laboratory of Advanced Science and Technology for Industry, University of Hyogo
[2]Graduate School of Engineering, University of Hyogo

Abstract

The irradiation effect of atomic H on Si surface was investigated by X-ray photoelectron spectroscopy. After the atomic H irradiation at RT, C atoms on the Si surface were removed but O atoms were not removed. To control the sample temperature during atomic H irradiation, a heater was installed behind the sample holder. After atomic H irradiation below 660 °C, no spectral change was observed. With increasing the sample temperature during atomic H irradiation at 830 °C, the peak of the O 1s level disappeared but a peak of the C 1s level appeared. This indicates that the surface oxide layer on Si surface was removed and Si carbide was generated during atomic H irradiation at 830 °C.

Introduction

Since the atomic H, which is generated on heated W under ambient H_2 gas, is very reactive, it has been used for a wide range of applications such as the low-temperature crystallization of a-Si [1], the dry etching of crystalline Si [2], vacuum chamber cleaning and photoresist removal [3]. One of the authors has developed as the atomic H annealing treatment [1, 4] and has demonstrated that the Si-rich SiO_x film was reduced and was etched [5]. However, it is considered that the atomic H treatment is difficult to reduce and etch the SiO_2 film [6].

In this study, we attempt to remove the native oxide on Si surface by irradiating the atomic H.

Experiments

The atomic H irradiation apparatus was constructed at the BL-07B end station of the NewSUBARU synchrotron radiation facility, the University of Hyogo. This apparatus is directly connected to a vacuum chamber of the end station through a gate valve. In Figs. 1 and 2, a picture and a schematic diagram of the atomic H irradiation apparatus are shown, respectively. As a filament, W mesh composed of 0.03 mm ϕ wire at the density of 30 wires per inch was used and heated at the temperature of about 1700 °C. Ar(95 %) and H_2(5 %) mixture gas was filled at the pressure of 10 Pa and at the flow rate of 100 sccm during the atomic H irradiation. The distance between W mesh and the sample was 150 mm in the case of the atomic H irradiation at RT. To control the sample temperature during atomic H irradiation, a heater made from a rolled W wire with a diameter of 0.4 mm was installed behind the sample holder. In addition, the distance between W mesh and the sample was approached at 50 mm in the case of the atomic H irradiation at higher sample temperature. The sample temperature during heating was recorded at a Cr/Al thermocouple attached to the sample holder.

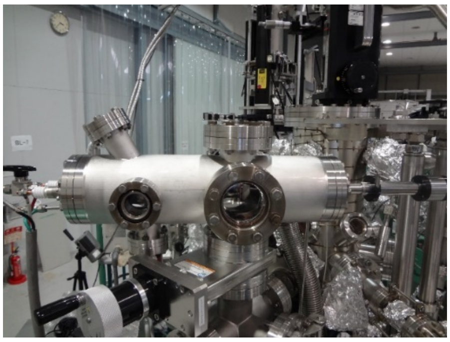

Fig. 1 Picture of the atomic H irradiation apparatus.

X-ray photoelectron spectroscopy (XPS) experiments were performed by using the conventional photoelectron spectroscopy apparatus, which was mounted with a R3000 (VG scienta) hemispherical electron energy analyzer. The Mg Kα line (hν = 1253.6 eV) was used as an X-ray source and was incident at 45° with respect to the surface normal. XPS spectra were measured at the emission angle of 45° to the surface normal. The total energy resolution was ~0.7 eV. The base pressure in the photoelectron analysis chamber was 4×10^{-8} Pa. The typical size of the Si (001) sample for the XPS measurements was $10\times10\times1$ mm^3.

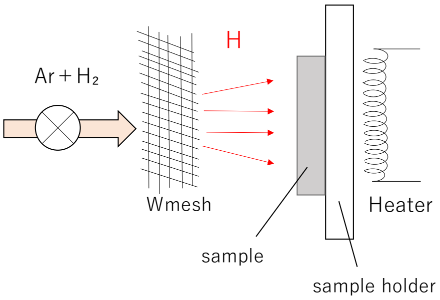

Fig. 2 Schematic diagram of the atomic H irradiation apparatus.

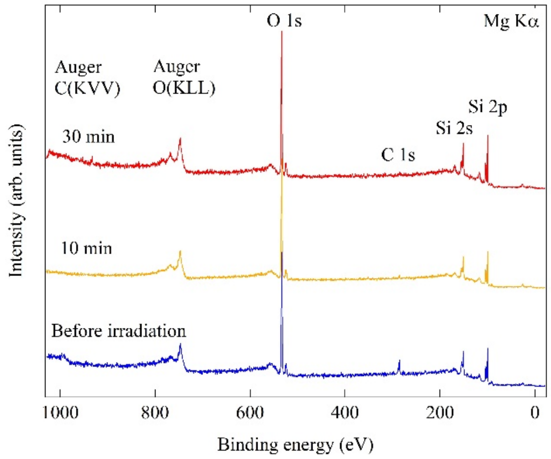

Fig. 3 Wide range of XPS spectra of a Si sample at RT as a function of the atomic H irradiation time.

Results and discussion

Figure 3 shows the wide range of XPS spectra of a Si sample at RT as a function of the atomic H irradiation time. Before atomic H irradiation, several peaks originating from the C, O, and Si atoms were observed in the photoelectron spectrum. The peaks at ~1000, ~750, ~530, ~290, ~150 and ~100 eV were assigned to Auger levels by C KVV and O KLL decay process, the O 1s level, C 1s, Si 2s and Si Si 2p levels, respectively [7]. These peak assignments are denoted beside the top spectrum. It is clear that there are C and O atoms on the surface of the Si sample before atomic H irradiation. The O atoms are derived from the native oxide layer and the C atoms are from the contamination on the native oxide layer. After atomic H irradiation for 10 minutes, the peak intensity of the C 1s level was decreased considerably. Further, the C 1s level was not observed after atomic H irradiation for 30 minutes. This indicates that the C atoms on the Si surface were removed by the atomic H irradiation.

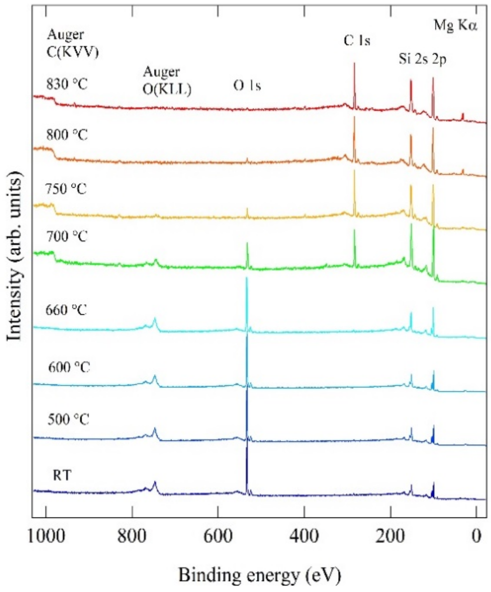

Fig. 4 Wide range of XPS spectra of a Si sample as a function of the sample temperature during atomic H irradiation.

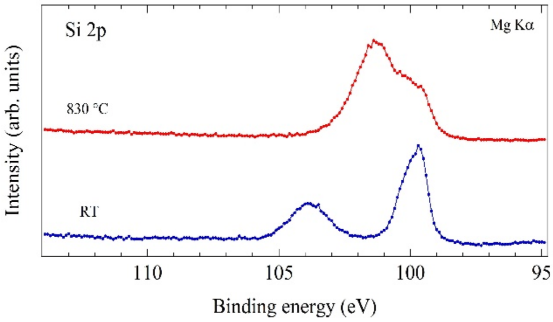

Fig. 5 XPS spectra of a Si 2p level after atomic H irradiation at RT and at 830 °C.

Figure 4 shows the wide range of XPS spectra of a Si sample as a function of the temperature during atomic H irradiation. The atomic H irradiation time was an hour. After atomic H irradiation at less than 660 °C, the spectral features were not changed. After atomic H irradiation at 700-750 °C, the peak intensity of the O 1s level was decreased and that of the C 1s level appeared. The origin of the C atoms is probably due to the reaction with the residual gas because a base pressure of the atomic H irradiation apparatus was ~10^{-6} Pa. After atomic H irradiation at 830 °C, the peak intensity of the O 1s level was completely eliminated while the that of the C 1s level was increased. This indicates that the surface oxide layer was removed at 830 °C during atomic H irradiation. In Fig. 5, the XPS spectrum of the Si 2p level after atomic H irradiation at 830 °C was compared with that after atomic H irradiation at RT. After atomic H irradiation at RT, two peaks were observed at ~104 and ~100 eV. These peaks at ~104 and ~100 eV were assigned to surface SiO_2 and bulk Si components, respectively. After atomic H irradiation at 830 °C, the peak at ~104 eV disappeared and a new peak appeared at ~101.5 eV. From the binding energy, the peak at ~101.5 eV was assigned to SiC component [8]. Therefore, it was found that the Si carbide is generated on the surface.

In this study, it was found that the surface oxide layer on Si was removed and Si carbide is generated at 830 °C during atomic H irradiation.

References

[1] A. Heya, A. Masuda, and H. Matsumura: Appl. Phys. Lett. **74**, 2143, (1999).

[2] K. Uchida, S. Hashioka, A. Izumi, and H. Matsumura: 2000 Dry Process Symp., 2000, p. 231.
[3] A. Izumi and H. Matsumura: Jpn. J. Appl. Phys. **41**, 4639, (2002).
[4] A. Heya and N. Matsuo: Jpn. J. Appl. Phys. **46**, 3545, (2007).
[5] A. Heya: Proceeding of 26th International Workshop on Active-Matrix Flatpanel Displays and Devices (AM-FPD) 2019.
[6] S. Veprek, C. Wang, M. G. J. Vepprek-Heijman, J. Vac. Sci. Technol. A, 26, 313, (2008).
[7] C. D. Wagner, W. M. Riggs, L. E. Davis, J. F. Moulder and G. E. Muilenberg: Handbook of X-ray photoelectron spectroscopy, ed. G. E. Muilenberg (Perkin-Elmer, Eden Prairie, Minnesota, 1978).
[8] Jiahao Guo Kaiyue Song Bingbing Wu Xiang Zhu Beilin Zhang and Yantao Shi: RSC advances. 7, 22875, (2017).

Part 3. List of Publications

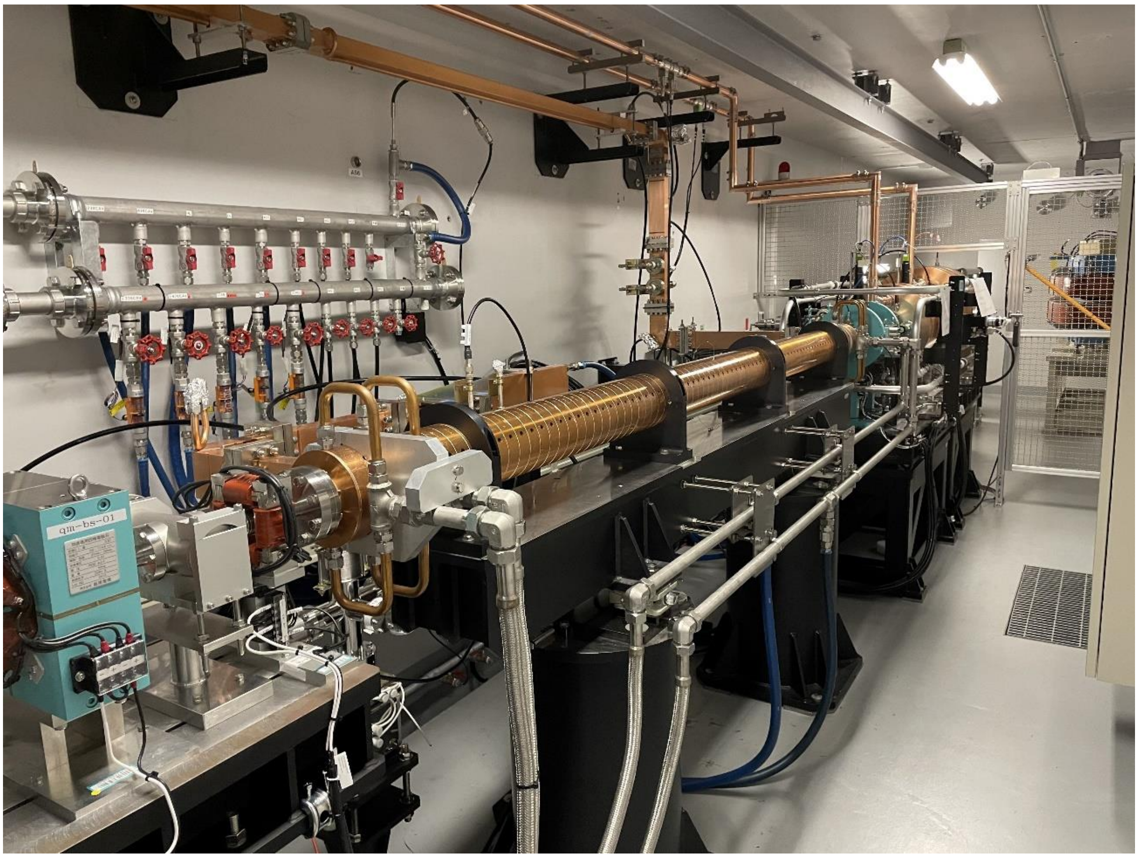

New Injector Linac

Papers

1. **"Development of a convenient positron annihilation lifetime and Doppler broadening measurement system for bulk materials using the 17 MeV gamma beam at the NewSUBARU synchrotron radiation facility"**
   Kento Sugitaa, Shuji Miyamotob, Mititaka Terasawab,Sho Amanob, Satoshi Hashimotob, Kenji Umezawaa, Fuminobu Hori
   Nuclear Instruments and Methods in Physics Research Section A, Accepted for publication

2. **"Development of an undulator with a variable magnetic field profile"**
   T. Tanaka, Y. Kida, R. Kinjo, T. Togashi, H. Tomizawa, S. Hashimoto, S.Miyamoto, S. Okabe, Y. Tanaka
   Journal of synchrotron radiation 28, pp.404-409 (2020)

3. **"Neutron emission spectrum from gold excited with 16.6 MeV linearly polarized monoenergetic photons"**
   Y. Kirihara, H. Nakashima, T. Sanami, Y. Namito, T. Itoga, S. Miyamoto, A. Takemoto, M. Yamaguchi, Y. Asano
   Journal of Nucl. Sci. Technol., vol. 57, no. 4, pp. 444-456 (2020)

4. **"Real-time in vivo dosimetry system based on an optical fiber-coupled micro-sized photostimulable phosphor for stereotactic body radiation therapy"**
   R. Yada, K. Maenaka, S. Miyamoto, G. Okada, A. Sasakura, M. Ashida, M. Adachi, T. Sato, T. Wang, H. Akasaka, N. Mukumoto, Y. Shimizu, and R. Sasaki
   Medical Physic, Vo.47, Issue10, pp.5235-5249 (2020)

5. **"Energy and angular distribution of photo-neutrons for 16.6 MeV polarizedphoton on medium–heavy targets"**
   T. K. Tuyet, T. Sanami, H. Yamazaki, T. Itoga, A. Takeuchi, Y. Namito, S. Miyamoto, Y. Asano
   Nuclear Instrum. Methods in Phys. Res. A 989, 164965 (2021). (Available online 17 December 2020)

6. **"Low-lying electric and magnetic dipole strengths in 207Pb"**
   T. Shizuma, F. Minato, M. Omer, T. Hayakawa, H. Ohgaki, and S. Miyamoto
   Phys. Rev. C 103, 024309 (2021). (Published 5 February 2021)

7. **"Local Structure Analysis on Si-Containing DLC Films based on the Measurement of C K-edge and Si K-edge X-ray Absorption Spectra"**
   Kazuhiro Kanda, Shuto Suzuki, Masahito Niibe, Takayuki Hasegawa, Tsuneo Suzuki and Hedetoshi Saitoh
   Coatings, 10 (2020) 330; doi:10.3390/coatings10040330

8. **"Graphene synthesis from pentacene by soft X-ray irradiation"**
   Akira Heya, Tomohiro Oonuki, Ryuichi Utimi, Kazuhiro Kanda, Ryo Yamasaki and Koji Sumitomo
   Thin Solid Films, 713 (2020) 138365; doi:10.1016/j.tsf.2020.138365

9. **"DLC 膜の構造分析法と ISO20523"**
   神田一浩
   表面技術, 71, 543-546 (2020)

10. **"Effect of Soft X-ray Irradiation on Film Properties of a Hydrogenated Si-Containing DLC Film"**
    Kazuhiro Kanda, Ryo Imai, Shotaro Tanaka, Shuto Suzuki, Masahito Niibe, Takayuki Hasegawa, Tsuneo Suzuki, and Hiroki Akasaka
    Materials, 14, 14924 (2021)

11. **"Control of Molecular Orientation of Spiro-OMeTAD on Substrates"**
    Naoyuki Shibayama, Hiroyuki Maekawa, Yuiga Nakamura, Yuichi Haruyama, Masahito Niibe, Seigo Ito
    ACS Appl. Mater. Interfaces 12, 50187-50191 (2020). doi: 10.1021/acsami.Oc15509

12. **"Effect of nonequilibrium atmospheric pressure O2 plasma-assiated annealing on anatase TiO2 nanoparticls"**
    Retsuo Kawakami, Yuki Yoshitani, Akihiro Shirai, Shin-ichiro Tanagiya, Hirofumi Koide, Yuki Mimoto, Kosuke Kajikawa, Masahito Niibe, Yoshitaka Nakano, Chisato Azuma, Takashi Mukai
    Appl. Surf. Sci. 526, 146684 (2020). doi: 10.1016/j.apsusc.2020.146684

13. **"Electronic structure of a 3x3-ordered silicon layer on Al(111)"**
    Yusuke Sato, Yuki Fukaya, Mathis Cameau, Asish K. Kundu, Daisuke Shiga, Ryu Yukawa, Koji Horiba, Chin-Hsuan Chen, Angus Huang, Horng-Tay Jeng, Taisuke Ozaki, Hiroshi Kumigashira, Masahito Niibe, and Iwao Matsuda
    Phys. Rev. Mater., 4, 064005 (2020). DOI: 10.1103/PhysRevMaterials.4.06405.

14. **"X-ray absorption and photoemission spectroscopy of bulk insulating materials using graphene"**
    Satoru Suzuki, Yuichi Haruyama, Akinobu Yamaguchi, Tomoki Yamamoto, Takuya Yoshizumi, Ayaka Fujii, Seiji Nakashima, Yakumo Fuchiwaki, Hironori Fujisawa, Takuo Ohkochi, Mari Ishihara, Hirosuke Sumida
    J. Appl. Phys. 128, 015304-1-8 (2020)

15. **"Water electrolysis using thin Pt and RuOx catalysts deposited by a flame-annealing method on pencil-lead graphite-rod electrodes"**
    R. Tsuji, Y. Koshino, H. Matsutani, Y. Haruyama, M. Niibe, S. Suzuki, S. Nakashima, H. Fujisawa, S. Ito
    ACS Omega 5, 6090-6099 (2020)

16. **"Immobilizing a π-Conjugated Catecholato Framework on Surfaces of SiO2 Insulator Films via a One-Atom Anchor of a Platinum Metal Center to Modulate Organic Transistor Performance"**
    Keishiro Tahara, Yuya Ashihara, Takashi Ikeda, Tomofumi Kadoya, Jun-ichi, Fujisawa, Yoshiki Ozawa, Hiroyuki Tajima, Noriaki Toyoda, Yuichi Haruyama, and Masaaki Abe
    Inorganic Chemistry, 59, 17945–17957 (2020). doi.org/10.1021/acs.inorgchem.0c02163

17. **"A Global Shutter Wide Dynamic Range Soft X-Ray CMOS Image Sensor with Backside-Illuminated Pinned Photodiode, Two-Stage Lateral Overflow Integration Capacitor, and Voltage Domain Memory Bank"**
    H. Shike, R. Kuroda, R. Kobayashi, M. Murata, Y. Fujihara, M. Suzuki, S. Harada, T. Shibaguchi, N. Kuriyama, T. Hatsui, J. Miyawaki, T. Harada, Y. Yamasaki, T. Watanabe, Y. Harada
    IEEE Trans. Electron Devices 68, 2056-2063 (2021)

18. **"A Global Shutter Wide Dynamic Range Soft X-ray CMOS Image Sensor with BSI Pinned Photodiode, Two-stage LOFIC and Voltage Domain Memory Bank"**
    H. Shike, R. Kuroda, R. Kobayashi, M. Murata, Y. Fujihara, M. Suzuki, T. Shibaguchi, N. Kuriyama, J. Miyawaki, T. Harada, Y. Yamasaki, T. Watanabe, Y. Harada and S. Sugawa
    IEEE IEDM 2020, 16.4, pp. 339-342 (2020)

19. **"Analysis of Chemical Contents Spatial Distribution in EUV Resist Using Resonant Soft X-ray Scattering Method"**
    Jun Tanaka, Takuma Ishiguro, Tetsuo Harada, Takeo Watanabe
    J. Photopolym. Sci. Technol. 33, pp. 491-498 (2020)

20. **"Higher Sensitive Extreme Ultraviolet (EUV) Resist Materials DerivedFrom p-t-Butylcalix[n]arenes (n = 4 and 8) "** (Invited)
Hiroyuki Maekawa, Hiroto Kudo, Takeo Watanabe, Hiroki Yamamoto, Kazumasa Okamoto, Takahiro Kozawa
Photopolym. Sci. Technol., 33, 45-51 (2020)

21. **"Removal of Surface Contamination by Atomic Hydrogen Annealing"**
A. Heya, T. Harada, M. Niibe, K. Sumitomo, and T. Watanabe
J. Photopolym. Sci. Technol. 33, 419-426 (2020)

22. **"Molecular Structure Evaluation of Bulk Polytetrafluoroethylene Modified by X-ray Irradiation"**
Masaya Takeuchi, Atsushi Kinoshita, Akinobu Yamaguchi, Yuichi Utsumi
Journal of Photopolymer Science and Technology, 33, 3, 295-299 (2020)

23. **"Design and Fabrication of PTFE Substrate Integrated Waveguide Coupler by SR Direct Etching"**
M. Kishihara, M. Takeuchi, A. Yamaguchi, Y. Utsumi, and I. Ota
IEICE Trans. Electron. Volume and Number: Vol.E104-C, No.9 (2021)

24. **"Anisotropic pyrochemical dry etching of fluorinated ethylene propylene induced by pre-irradiation with synchrotron radiation"**
Kaito Fujitani, Masaya Takeuchi, Yuichi Haruyama, Akinobu Yamaguchi, and Yuichi Utsumi
AIP Advances 11, 025104 (2021)

25. **"Non-Destructive Imaging on Synthesised Nanoparticles"**
Kelvin Elphick, Akinobu Yamaguchi, Akira Otsuki, Neil Lonio Hayagan, and Atsufumi Hirohata
Materials, 14, 613 (2021)

26. **"Direct observation of a magnetic domain change in Ni wire and film on a LiNbO3 substrate using X-ray magnetic circular dichroic photoemission electron microscopy"**
Ryo Nakamura, Shunya Saegusa, Naoya Akamatsu, Keisuke Yamada, Takeshi Ogasawara, Masaki Oura, Takuo Ohkochi, Akinobu Yamaguchi
Japanese Journal of Applied Physics 60, SBBC01-1-5 (2021)

27. **"A Lab in Bento Box: Autonomous centrifugal microfluidic system for an enzyme-linked immunosorbent assay"**
Takaaki Abe, Shunya Okamoto, Akinobu Taniguchi, Michiyasu Fukui, Akinobu Yamaguchi, Yuichi Utsumi, Yoshiaki Ukita
Analytical Methods, 12, 4858-4866 (2020)

28. **"Highly Stable and Reproducible Au Nanorod Arrays for Near-Infrared Optofluidic SERS sensor"**
Samir Kumar, Takao Fukuoka, Ryo Takahashi, Mitsuhiro Yoshida, Yuchi Utsumi, Akinobu Yamaguchi, Kyoko Namura, Motofumi Suzuki
Materials Letters 286, 129106 (2021)

29. **"Visualization of elemental distributions and local analysis of element-specific chemical-states of Arachnoidiscus sp. frustule using soft x-ray spectromicroscopy"**
Tomoko Ishihara, Takuo Ohkochi, Akinobu Yamaguchi, Yoshinori Kotani, Masaki Oura
PLOS ONE 15(12), e0243874 (2020)

30. **"Gold nanoparticles enhance EGFR inhibition and irradiation effects in head and neck**

squamous carcinoma cells"
Masahiko Kashin, Yasumasa Kakei, Shun Teraoka, Takumi Hasegawa, Akinobu Yamaguchi, Takao Fukuoka, Ryohei Sasaki, Masaya Akashi
BioMed Research International Article ID 1281645 (2020)

31. **"Application of microprobe soft x-ray fluorescence analyses to characterize the multi-layered buried micro-structure"**
    M. Oura, T. Ishihara, A. Yamaguchi
    Jpn. J. Appl. Phys., 59, 060902 (2020)

32. **"Dependence of Gilbert damping constant on microstructure in nanocrystalline YIG thin films chemically prepared by co-precipitation and spin-coating on a Si substrate"**
    K. Yamada, K. Kogiso, Y. Shiota, A. Yamaguchi, T. Moriyama, T. Ono, and M. Shima
    Journal of Magnetism and Magnetic Materials 513, 167253 (2020)

33. **"Enhancement of the rectifying voltage and Gilbert damping of a Ni wire fabricated on LiNbO3 substrate"**
    A. Yamaguchi, R. Nakamura, S. Saegusa, N. Akamatsu, K. -J. Kim, T. Lee, A. Nakao, T. Ohkochi, K. Yamada
    Japanese Journal of Applied Physics 59, 083001 (2020)

34. **"Solid/Liquid-interface-dependent synthesis and immobilization of copper-based particles nucleated by the X-ray-radiolysis-induced photochemical reaction"**
    Akinobu Yamaguchi, Ikuya Sakurai, Ikuo Okada, Hirokazu Izumi, Mari Ishihara, Takao Fukuoka, Satoru Suzuki, and Yuichi Utsumi
    Journal of Synchrotron Radiation 27, 1008-1014 (2020)

35. **"マイクロ波加熱によるオンチップ金ナノ粒子合成"**
    竹内雅耶，岸原充佳，福岡隆夫，山口明啓，内海裕一
    電気学会論文誌 C Vol. 140, pp. 471-475 (2020)
    "On Chip Synthesis of Au Nanoparticles by Microwave Heating"
    Masaya Takeuchi, Mitsuyoshi Kishihara, Takao Fukuoka, Akinobu Yamaguchi, Yucihi Utsumi
    IEEJ Transactions on C Vol. 140, pp. 471-475 (2020)

36. **"Lab-on-a-disc におけるオイラー力を用いた異密度液体の混合"**
    竹内雅耶，藤谷海斗，三枝峻也，石本睦，山口明啓，内海裕一
    電気学会論文誌 C Vol. 140, pp. 465-470 (2020)
    "Mixing of difference density liquids by Euler-force on Lab-on-a-disc"
    Masaya Takeuichi, Kaito Fujitani, Atsushi Ishimoto, Akinobu Yamaguchi, Yuichi Utsumi
    IEEJ Transactions on C Vol. 140, pp. 465-470 (2020)

37. **"Observing the Delamination Interface in Multi Layered Thin Films with a MgAg Alloy Top Layer and Organic Semiconductor under Layers on a Flexible Substrate"**
    KOBAYASHI Toshiro, FURUMOTO Hideaki, YAMAGUCHI Akinobu, KANEMATSU Hideyuki, GRUESCU Ion Cosmin
    Advanced Experimental Mechanics, Vol.5, pp.151-156 (2020)

Books

1. **"Characterization of Hydrogen-Free and Hydrogenated DLC Films"**
    Toru Harigai, Takahiro Imai, Hirofumi Takikawa, Satoru Kaneko, Shinsuke Kunitsugu, Masahito Niibe, Kazuhiro Kanda and Masao Kamiya
    in "Carbon Related Materials", Springer, 2020, pp. 55-69 (ISBN 978-981-15-7610-2)

Proceedings

1. **"Resist pattern inspection for defect reduction in sub-15 nm templates"**
   T. Motokawa, M. Suenaga, K. Hagihara, N. Iida nee Sakurai, R. Komatsu, H. Sakurai, S. Kanamitsu, K. Tsuda, T. Harada, T. Watanabe
   Proc. SPIE 11518 (2020) 115180H.

2. **"Showcase of the Fundamental Research to Resolve the Technical Issues in EUV Lithography at NewSUBARU Synchrotron Light Facility of University of Hyogo"** (Invited)
   Takeo Watanabe, Tetsuo Harada, Shinji Yamakawa
   Proceedings of EUVL International Workshop 2020.

3. **"Reflectance Measurement of EUV Mask under OoB-Irradiation, and Hydrogen and Water Vapor Environments under the High Power EUV Irradiation"** (Invited)
   Takeo Watanabe and Tetsuo Harada
   Proceedings of EUVL International Workshop 2020.

4. **"Showcase of the Fundamental EUVL Research"** (Invited)
   Takeo Watanabe, Tetsuo Harada, and Shinji Yamakawa
   Proceedings of 2020 EUVL Supplier Showcase.

5. **"Fundamental Research Activities of EUV Lithography at NewSUBARU Synchrotron Light Facility"** (Invited)
   Takeo Watanabe and Tetsuo Harada
   Proceedings of High-brightness Sources and Light-driven Interactions Congress, OSA, Nov. 16-20, 2020.

6. **"Fundamental Research Activities of EUV Lithography at NewSUBARU Synchrotron Light Facility"** (Invited)
   Takeo Watanabe and Tetsuo Harada,
   Proceedings of 5th EUV-FEL Workshop 2021, Jan. 22, 2021

7. **"Real-time optical monitoring of cell culture in centrifugal microfluidics"**
   Edwin En-Te Hwu, Lina Gruzinskyte, Atsushi Ishimoto, Laura Serioli, Sriam Thoppe Rajendran, Akinobu Yamaguchi, Kinga Zór, and Anja Boisen
   The 24th International Conference on Miniaturized Systems for Chemistry and Life Science (mTAS 2020), pp. 1039 - 1040 (2020)

Articles

1. **"Synchrotron radiation extreme ultraviolet lithography technology that opens up the world of innovative IoT and AI"** (Invited paper)
   Takeo Watanabe
   Clean Technology, 2, pp.1-5 (2020). (in japanese)

International Meetings

1. **"GDR cross sections updated in the IAEA-CRP"**
H. Utsunomiya, I. Gheorghe, D. M. Filipescu, K. Stopani, S. Belyshev, H. Wang, G. Fan, T.i Ariizumi, Y.-W. Lui, D. Symochko, M. Krzysiek, S. Miyamoto, S. Goriely, and T. Kawano
EPJ Web of Conferences 239, 01002 (2020)
https://doi.org/10.1051/epjconf/202023901002

2. **"NEXAFS evaluation for the lumen of DLC coated small diameter long-sized medical objective tube by using AC high-voltage burst plasma CVD method"**
Yuichi Imai, Kazuhiro Kanda, Yasuhiro Fujii, Susumu Ouzawa, Daiki Ousaka and Tatsuyuki Nakatani
12th International Symposium on Advanced Plasma Science and its Applications for Nitrides and Nanomaterials / 13th International Conference on Plasma-Nano Technology & Science (ISPlasma2020/IC-PLANTS2020) [10P2-52], 2020.3.8-11, Nagoya University

3. **"Stability of Amino Acid Precursors in Space: Verification by Ground Simulations and Space Experiments"**
Kensei Kobayashi, Tomohito Sato, Takuya Yokoo, Soushi Kuramoto, Yoko Kebukawa, Hajime Mita, Miki Nakayama, Kazumichi Nakagawa, Hiromi Shibata, Hitoshi Fukuda, Yoshiyuki Oguri, Isao Yoda, Satoshi Yoshida, Kazuhiro Kanda, Itsuki Sakon, Hajime Yano, Hirofumi Hashimoto, Shin-ichi Yokobori and Akihiko Yamagishi
European Astrobiology Network Association 2020 (EANA2020) 2020.8.27-28 virtual meeting

4. **"A Global Shutter Wide Dynamic Range Soft X-ray CMOS Image Sensor with BSI Pinned Photodiode, Two-stage LOFIC and Voltage Domain Memory Bank"**
H. Shike, R. Kuroda, R. Kobayashi, M. Murata, Y. Fujihara, M. Suzuki, T. Shibaguchi, N. Kuriyama, J. Miyawaki, T. Harada, Y. Yamasaki, T.Watanabe, Y. Harada and S. Sugawa
IEEE IEDM 2020, Online, 2020/12.

5. **"Resist pattern inspection for defect reduction in sub-15 nm templates "**
T. Motokawa, M. Suenaga, K. Hagihara, N. Iida nee Sakurai, R. Komatsu, H. Sakurai, S. Kanamitsu, K. Tsuda, T. Harada, T. Watanabe
SPIE Photomask technology 2020, Online, 2020/9.

6. **"Removal of Surface Contamination by Atomic Hydrogen Aneealing"**
A. Heya, T. Harada, M. Niibe, K. Sumitomo, and T. Watanabe
ICPST37, Japan, 2020/6.

7. **"Analysis of Chemical Contents Spatial Distribution in EUV Resist Using Resonant Soft X-ray Scattering Method"**
Jun Tanaka, Takuma Ishiguro, Tetsuo Harada, Takeo Watanabe
ICPST37, Japan, 2020/6.

8. **"Showcase of the Fundamental Research to Resolve the Technical Issues in EUV Lithography at NewSUBARU Synchrotron Light Facility of University of Hyogo"** (Web online) (Invited)
Takeo Watanabe, Tetsuo Harada, Shinji Yamakawa
EUVL International Workshop, Jun. 2020, Berkeley, CA, USA, Jun. 7-11, 2020.

9. **"Reflectance Measurement of EUV Mask under OoB-Irradiation, and Hydrogen and Water Vapor Environments under the High Power EUV Irradiation"**
Takeo Watanabe and Tetsuo Harada

EUVL International Workshop (Web online), Jun. 2020, Jun. 7-11, 2020.

10. **"Higher Sensitive Extreme Ultraviolet (EUV) Resist Materials Derived From p-t-Butylcalix[n]arenes (n=4 and 8) "**
    Hiroyuki Maekawa, Hiroto Kudo, Takeo Watanabe, Hiroki Yamamoto, Kazumasa Okamoto, Takahiro Kozawa
    ICPST-37, Japan, May. 18-21, 2020.

11. **"Showcase of the Fundamental EUVL Research"** (Web online) (Invited)
    Takeo Watanabe, Tetsuo Harada, and Shinji Yamakawa
    2020 EUVL Supplier Showcase, Web conference by ZOOM, 2020.Sep. 14-15, 2020.

12. **"Fundamental Research Activities of EUV Lithography at NewSUBARU Synchrotron Light Facility"** (web online) (Invited)
    Takeo Watanabe and Tetsuo Harada
    High-brightness Sources and Light-driven Interactions Congress, OSA, Nov. 16-20, 2020.

13. **"Fundamental Research Activities of EUV Lithography at NewSUBARU Synchrotron Light Facility"** (Web online) (Invited)
    Takeo Watanabe and Tetsuo Harada
    5th EUV-FEL Workshop 2021, Jan. 22, 2021.

14. **"Aqueous-soluble Ink including Nano Beacon"**
    Akinobu Yamaguchi, Yuichi Utsumi, Kyoko Namura, Motofumi Suzuki, and Takao Fukuoka
    L51-03, Pittcon 2021, March 11, 2021. Oral.

15. **"Real-time optical monitoring of cell culture in centrifugal microfluidics"**
    Edwin En-Te Hwu, Lina Gruzinskyte, Atsushi Ishimoto, Laura Serioli, Sriram Thoppe Rajendran, Akinobu Yamaguchi, Kinga Zór, and Anja Boisen
    M1-180.e, The 24th International Conference on Miniaturized Systems for chemistry and life sciences (µTAS 2020), October 5, Monday, 2020.

16. **"Study on magnetic properties of artificial magnets induced by ferromagnetic/ferroelectric heterojunction"**
    Akinobu Yamaguchi, Ryo Nakamura, Shunya Saegusa, Naoya Akamatsu, Aiko Nakao, Yuichi Utsumi, Masaki Oura, Takeshi Ogasawara, Keisuke Yamada, Takuo Ohkochi
    IEEE-NEMS 2020 (The 15th IEEE International Conference on Nano/Micro Engineered & Molecular Systems," TS9-3, September 29, 2020, Oral

17. **"Study on solid/solid- and solid/liquid-interface-dependent material properties for an artificial multiferroic system and additive manufacturing process"**
    Akinobu Yamaguchi, Shunya Saegusa, Ryo Nakamura, Naoya Akamatsu, Aiko Nakao, Ikuya Sakurai, Ikuo Okada, Yuichi Utsumi, Takeshi Ogasawara, Keisuke Yamada, Masaki Oura, Takuo Ohkochi
    2020 International Conference on Solid State Deives and Materials (SSDM 2020), C-2-04, September 28, 2020, Oral

Academic Degrees

Master of Engineering

Takuma Ishiguro (University of Hyogo)
"Resonant Soft X-ray Reflectivity for the Chemical Analysis in Thickness Direction of EUV Resist"

Ayato Ohgata (University of Hyogo)
"Hydrogen Damage Evaluation of Mo/Si Multilayer using High-Power EUV Irradiation Tool"

Jun Tanaka (University of Hyogo)
"Analysis of Chemical Contents Spatial Distribution in EUV Resist Using Resonant Soft X-ray Scattering Method"

Keisuke Tsuda (University of Hyogo)
"Development of Grazing-Angle Coherent EUV Scatterometry Microscope for Resist Pattern Observation"

Atsushi Ishimoto (University of Hyogo)
"Study on implementation of mixing system in microfluidic devices"

Shunya Saegusa (University of Hyogo)
"Particle agglutination control by microsystem and its application to molecular sensor"

Ryo Nakamura (University of Hyogo)
"Creation of novel artificial materials consisting of heterojunction and study on their physical properties"

LASTI Annual Report Vol. 22 (2020)

October 2021, Published by
Laboratory of Advanced Science and Technology for Industry
University of Hyogo
3-1-2 Kouto, Kamigori-Cho, Ako-gun, Hyogo 678-1205, JAPAN
Phone: +81-791-58-0249 / FAX: +81-791-58-0242

Laboratory of Advanced Science and Technology for Industry
University of Hyogo

3-1-2 Kouto, Kamigori, Ako-gun, Hyogo 678-1205 Japan

兵庫県立大学 高度産業科学技術研究所
〒678-1205 兵庫県赤穂郡上郡町光都 3-1-2